

**FINAL REPORT  
FOR  
HIGH-SPEED STRAINED QUANTUM-WELL LASERS  
AND OPTOELECTRONIC DEVICES**

October 1, 1995 - December 31, 1998

Submitted to

Dr. Yoon-Soo Park  
CODE 312  
Office of Naval Research  
800 N. Quincy Street  
Arlington, VA 22217-5660

Grant No. N00014-96-1-0303

Prepared by

S. L. Chuang  
Department of Electrical and Computer Engineering  
University of Illinois at Urbana-Champaign  
Urbana, IL 61801

April 5, 1999

**DISTRIBUTION STATEMENT A**  
Approved for Public Release  
Distribution Unlimited

19990526 123

**DTIC QUALITY INSPECTED 1**

**FINAL REPORT  
FOR  
HIGH-SPEED STRAINED QUANTUM-WELL LASERS  
AND OPTOELECTRONIC DEVICES**

October 1, 1995 - December 31, 1998

Submitted to

Dr. Yoon-Soo Park  
CODE 312  
Office of Naval Research  
800 N. Quincy Street  
Arlington, VA 22217-5660

Grant No. N00014-96-1-0303

Prepared by

S. L. Chuang  
Department of Electrical and Computer Engineering  
University of Illinois at Urbana-Champaign  
Urbana, IL 61801

April 5, 1999

**FINAL REPORT on AASERT Project**  
(October 1, 1995 - December 1, 1998)

**1. Contract Title:** High-Speed Strained Quantum-Well Lasers and Optoelectronic Devices

**Number:** N00014-96-1-0303

**PI:** Professor S. L. Chuang  
University of Illinois at Urbana-Champaign  
Department of Electrical and Computer Engineering  
1406 W. Green Street, Urbana, IL 61801  
Phone: (217) 333-3359 Fax: (217) 333-5701  
e-mail: s-chuang@uiuc.edu

**Program Manager:** Dr. Y. S. Park, Code: ONR 312

**2. Technical Objectives:**

We investigate research issues on strained quantum-well optoelectronic devices and their applications for navy needs. This work studies the fundamental physics in strained quantum-well devices such as Fabry-Perot (FP) lasers, distributed-feedback (DFB) lasers, and vertical cavity surface-emitting lasers (VCSELs) through the development of theory and experiment. Integrated optoelectronic devices are also investigated for applications in wavelength-division-multiplexed (WDM) fiber-optic communications systems such as wavelength tunability and wavelength conversion. In this work, we investigate the following areas:

- a. Comprehensive characterization of fundamental parameters of strained quantum-well lasers
- b. Modeling and experiment of integrated laser/modulator devices
- c. Modeling and experiment of VCSELs
- d. Wavelength conversion using four-wave mixing and cross-phase/gain/absorption modulation
- e. Optical gain theory for GaN-based blue-green quantum-well lasers

**3. Approach**

- a. Use of our amplified spontaneous emission (ASE) measurements to study the intrinsic parameters of high-speed laser systems and to assess the temperature sensitivity of these parameters.
- b. Use of our high-speed modulation and measurement system to experimentally assess the carrier dynamics and the temperature effects on the high speed response of quantum-well structures in both lasers and integrated devices.
- c. Comparison of experimental data and theory using a comprehensive model for the emission spectra of integrated optoelectronic devices such as three-electrode curved-waveguide DFB lasers with electroabsorption modulators, taking into account the longitudinal dependence of the carrier and photon densities.
- d. Theoretical modeling of curved waveguide DFB lasers with integrated electroabsorption modulators for use as wavelength-tunable laser sources.
- e. Comparison of experiment and theory for the high-speed modulation response and relative intensity noise in selectively oxidized VCSELs.
- f. Conduct experiments to measure the effects of polarization dependence and multiple pump beams on the conversion efficiency of four-wave mixing in conventional and novel three-electrode DFB lasers.

- g. Demonstrate a novel wavelength conversion experiment demonstrating cross-absorption modulation in an integrated electroabsorption modulator / laser.

#### **4. Accomplishments**

##### **A. Comprehensive characterization of strained quantum-well lasers**

**I. Fundamental parameters of DFB lasers.** We have extended our model for the amplified spontaneous emission (ASE) light from the facet of a laser diode to a distributed feedback structure. By comparing measured spectra to the theory with excellent agreement we are able to obtain important cavity parameters such as the coupling coefficient and the facet phases which are otherwise very difficult to determine. Also, this measurement and fit enables us to extract critical material parameters such as the gain and refractive index and the corresponding differential gain, differential index shift, and linewidth enhancement factor which are critical measures of laser modulation bandwidth and chirp performance. [Publications 1 and 9]

**II. Temperature dependence of InGaAsP quantum-well lasers.** We have also used the facet light emission to study the temperature dependence of bulk InGaAsP semiconductor lasers. The side light spontaneous emission is measured and compared with the gain obtained from the facet ASE spectrum through the fundamental relationship between these two parameters. Through this process we can calibrate the spontaneous emission measurement and obtain the actual radiative recombination rate. From measurements at different temperatures we have shown that the characteristic temperature for the non-radiative current density is 44 K for our lasers which causes the high-temperature sensitivity of these lasers. [Publication 6]

**III. Strained InGaAlAs quantum-well lasers.** We have measured intrinsic parameters for both strained InGaAsP and new strained and unstrained InGaAlAs material systems. For the InGaAlAs system we have found that compressive strain gives a larger differential gain and refractive index shifts than no strain and slight tensile strain. Also, the linewidth enhancement factor is greatly reduced for the compressively strained active regions when compared to that of the unstrained ones. When compared to an InGaAsP sample of similar compressive strain, the InGaAlAs samples have a much larger differential gain as well as a much larger refractive index shift. InGaAlAs active regions should yield much higher modulation bandwidths and should provide good candidates for devices such as modulators and wavelength converters which require a large index change. The linewidth enhancement factor for the two systems seem to be similar. [Publications 16 and 18]

**IV. High-speed microwave modulation of quantum-well lasers by electrical and optical injection.** We investigated optical injection in the absorption region of a quantum-well laser and compared with direct electrical injection. We show experimentally and theoretically that differences between the modulation responses for the two injection methods come from carrier transport and circuit parasitic effects. We also obtained more accurate measurements of several important dynamic laser parameters by using both injection methods. [Publication 21]

##### **B. Modeling of integrated laser/modulator devices**

**I. Spatial hole-burning and ASE of DFB lasers.** We have developed a transfer-matrix based model for distributed-feedback laser structures. With this model we are able to treat the spatial dependence of the photon density and carrier density self-consistently.

We have also achieved excellent agreement with the measured lasing spectrum as well as a measurement of the longitudinal carrier density profile obtained from the side light spontaneous emission from a typical index-coupled DFB laser. [Publication 12]

**II. Wavelength tuning in novel integrated laser/modulator devices.** Another advantage of this technique is that complicated structures with longitudinal dependence such as a chirped grating pitch as well as integrated devices can easily be modeled. We have applied this technique to explain the behavior of integrated DFB lasers integrated with electroabsorption modulators experimentally characterized in our lab. We have also had success explaining the tuning mechanisms for a tunable DFB laser integrated with a modulator which serves as a phase tuning section. We show that the wavelength-tuning range can be enhanced by increasing the bending of the curved waveguide. We also show that the use of the curved waveguide can suppress detrimental spatial hole burning effects so higher power operation can be achieved. [Publication 20]

**III. High-speed modulation of integrated devices.** We have developed an experimental setup to measure the frequency response of integrated laser and modulator devices and have compared the direct and external modulation on the same laser.

### **C. Modeling and experiment of VCSELs**

**I. Modal properties of selectively oxidized VCSELs.** We have developed a very efficient model to calculate the electromagnetic properties of VCSEL cavities based on the beam propagation method and a discrete Bessel transform. This method compares favorably to more computationally intensive models such as the Finite-Difference Time Domain model. We have used this model to study threshold properties and mode competition in pillar structures and selectively oxidized aperture devices. By determining the cavity quality factor and resonant wavelength of each mode we can design optimized structures for low threshold and single mode operation. Experimentally, we have developed a fiber-tip near-field measurement system which allows us to measure the near-field pattern of the VCSEL modes. We are currently using these techniques to measure the spatial and spectral properties of VCSEL laser modes including beam size and modal competition of selectively oxidized VCSELs. We have also measured the relative intensity noise (RIN) spectrum and studied the effects of competition between multiple transverse modes. [Publication 10]

**II. Bistability in selectively-oxidized VCSELs.** We have performed extensive experimental characterization of selectively oxidized VCSELs provided by our research collaborators at Sandia National Laboratory. We have observed a strong correlation between electrical and optical characteristics. The onset of lasing threshold for both the fundamental mode and for each higher order mode is indicated by a dip in  $I$ - $dV/dI$  curve. We have also observed new phenomena including both electrical and optical bistability. [Publication 8]

**III. High-speed modulation of VCSELs.** We have developed an experiment to study the high-speed modulation of VCSELs in both the small signal and large signal regimes. Initial experiments for the small signal modulation give a bandwidth of about 8 GHz. The spectral behavior is markedly different from that of single-mode edge emitting lasers. For the large signal domain, we observe several higher order harmonics in the modulation spectrum whose power dies down as the current is increased. We have also observed interesting effects such as period doubling for some operating conditions. In addition, the effects of lateral diffusion, carrier transport, and multiple transverse modes in

VCSELs were studied by modeling the high-speed modulation response, showing good agreement with experiment.

#### **D. Wavelength conversion by four-wave mixing, cross-phase modulation, and cross-absorption modulation**

**I. Four-wave mixing in a DFB laser.** We have performed a detailed study of wavelength conversion by four-wave mixing in distributed-feedback (DFB) lasers where the lasing modes serve as pump waves to facilitate the wavelength conversion. In a DFB laser with a single longitudinal mode, we have characterized the conversion efficiency up to detuning frequencies of 500 GHz. For small detunings, multiple conjugate signals are observed and measured. The dependence of each of these on the probe and pump powers were measured and agree quite well with a simple theoretical analysis. For larger detunings, the laser cavity has a pronounced effect on the efficiency spectrum which correlates very well to a simple analysis of the experimental ASE spectrum of the laser. [Publications 9 and 11]

**II. Four-wave mixing in two-lasing-mode DFB laser.** We have also measured four-wave mixing in DFB lasers with two simultaneous lasing modes. We have demonstrated that the shifted conjugate conversion efficiency is virtually independent of pump separation even though the frequency shift is increased by that amount. We have achieved a conversion efficiency of 2% for a frequency shift of 900 GHz even though the gain is clamped at threshold in these lasers. When compared to the single pump case for the same overall frequency shift, this conversion efficiency is almost 1000 times greater.

**III. Four-wave mixing in a novel tunable DFB laser.** We have characterized four-wave mixing in a tunable three-electrode DFB laser with a curved waveguide. This device gives a tuning range of over 4 nm and allows us to tune to the desired output wavelength. Initial studies indicate that the current injection profile and thus the spatial profile of the pump wave can have a large effect on the observed conversion efficiencies.

**IV. Polarization dependence of four-wave mixing.** We measured the spectral dependence of the conversion efficiency for polarization resolved four-wave mixing in a single mode distributed-feedback laser. We then used our measurements of the refractive index dispersion to calculate the polarization dependent phase mismatch for four-wave mixing. In addition, we measured the polarization resolved four-wave mixing in a distributed-feedback laser with simultaneous lasing TE and TM modes. The experimental observations agree very well with a qualitative analysis of the theoretical mechanism for four-wave mixing.

**V. Fundamental parameters for cross-gain and cross phase modulation.** We have performed measurements of the gain and refractive index in the presence of an optical pump light. Depending on the location of the pump (above or below transparency) we see enhancement or compression of the gain and index spectra. For the refractive index spectra we have demonstrated that the induced index shift is almost constant over a 100 nm wavelength span. This would indicate that efficient two-way cross-phase modulation could be achieved over the entire gain bandwidth of the semiconductor active region. [Publication 13]

**VI. Novel wavelength conversion by cross-absorption modulation.** We demonstrated wavelength conversion by a novel method, cross-absorption modulation, in an integrated electroabsorption modulator / laser (EML) for the first time. The EML serves as both the conversion medium and the converted wavelength light source, a technique

which requires less components than other methods of wavelength conversion using semiconductor optical amplifiers. Cross-absorption modulation as a function of input and converted signal power was measured to study absorption saturation effects in the modulator. Dependencies on input signal wavelength were also studied. The modulator voltage can be chosen to optimize cross-absorption modulation at a specific wavelength.

**E. Optical gain theory for GaN based blue-green quantum-well lasers.** We have published several fundamental papers on the band-structure and gain of wurtzite semiconductors. The k.p method was used to derive the proper Hamiltonian for strained nitride-based semiconductors with the wurtzite crystal symmetry. We have subsequently applied this Hamiltonian to the study of the band-structure of strained GaN and InGaN quantum wells. In addition, we have added many-body effects which includes bandgap renormalization and Coulomb enhancement of the gain model to our calculations for these material systems. We have found that these effects significantly contribute to the blue-shift of the peak gain in addition to its magnitude. Our model agrees very well with the first set of experimental data published recently by Nakamura. Recently, we have studied the effects of the strong piezoelectric fields in GaN based systems on the electronic band structure and optical gain. We have found that at lower carrier densities these induced fields dramatically lowers the calculated gain and can shift the peak gain position. The impact of the piezoelectric field on the laser performance has also been investigated, and we find that the laser threshold can be reduced for a certain crystal orientation direction such that the piezoelectric field is reduced and the band edge effective mass is smaller than the conventional growth direction along the c axis. [Publications 2-5, 14, 15, 17]

## **5. Significance of this work:**

The fundamental research conducted here, including theory on gain, high-speed response, and noise in lasers, allows for a better understanding of current device limitations and will enable higher performance device design. Our investigation of applications for strained quantum-well optoelectronics, such as wavelength-tunable sources for wavelength-division-multiplexing (WDM) fiber-optic communications systems, wavelength conversion in order to enable wavelength switching in dense WDM networks, and high-speed modulation in distributed-feedback (DFB) lasers and vertical-cavity surface-emitting lasers (VCSELs) is essential for enabling the growth of future optical communications systems.

## **6. Papers, Patents, and Awards:**

### **A. Publications:**

#### **(i) Journal Papers**

1. C. S. Chang, S. L. Chuang, J. Minch, Y. K. Chen, and T. Tanbun-Ek, "Amplified spontaneous emission spectroscopy in strained quantum-well lasers," *IEEE J. Selected Topics Quantum Electron.*, Special issue on Applied Optical Diagnostics of Semiconductors vol. 1, pp. 1100-1107, 1995.
2. S. L. Chuang and C. S. Chang, "Effective-mass Hamiltonian for strained wurtzite GaN and analytical solutions," *Appl. Phys. Lett.*, vol. 68, pp. 1657-1659, 1996.
3. S. L. Chuang and C. S. Chang,, "The k.p method for strained wurtzite semiconductors," *Phys. Rev. B*, vol. 54, pp. 2491-2504, 1996.

4. S. L. Chuang, "Optical gain of strained wurtzite GaN quantum-well lasers," *IEEE J. Quantum Electron.*, vol. 32, pp. 1791-1800, 1996.
5. S. L. Chuang and C. S. Chang, "Band structure model of strained quantum-well wurtzite semiconductors," *Semicond. Sci. and Technol.*, vol. 12, pp. 252-263, 1997.
6. W. Fang, M. Hattendorf, S. L. Chuang, J. Minch, C. S. Chang, C. G. Bethea, and Y. K. Chen, "Analysis of temperature sensitivity in semiconductor lasers using gain and spontaneous emission measurements," *Appl. Phys. Lett.*, vol. 70, pp. 796-798, 1997.
7. J. Minch, C. S. Chang, and S. L. Chuang, "Four-wave mixing in a distributed-feedback laser," *Appl. Phys. Lett.*, vol. 70, pp. 1360-1362, 1997.
8. J. Li, J.-F. Seurin, S. L. Chuang, K. D. Choquette, K. M. Geib, and H. Q. Hou, "Correlation of electrical and optical characteristics of selectively oxidized vertical cavity laser diodes," *Appl. Phys. Lett.*, vol. 70, pp. 1799-1801, 1997.
9. J. Minch, S. L. Chuang, C. S. Chang, W. Fang, Y. K. Chen, and T. Tanbun-Ek, "Theory and experiment on the amplified spontaneous emission from distributed-feedback lasers," *IEEE J. Quantum Electron.*, vol. 33, pp. 815-823, 1997.
10. J.-F. P. Seurin and S. L. Chuang, "Discrete Bessel transform and beam propagation method for modeling of vertical-cavity surface-emitting lasers," *J. Appl. Phys.*, vol. 82, pp. 2007-2016, 1997.
11. J. Minch, C. S. Chang, and S. L. Chuang, "Wavelength conversion in distributed-feedback lasers," *IEEE J. Selected Topics Quantum Electronics*, vol. 3, pp. 569-576, 1997.
12. W. Fang, A. Hsu, S. L. Chuang, T. Tanbun-Ek, and A. M. Sergent, "Measurement and modeling of distributed-feedback lasers with spatial hole burning," *IEEE J. Selected Topics Quantum Electronics*, vol. 3, pp. 547-554, 1997.
13. T. Keating, J. Minch, C. S. Chang, P. Enders, W. Fang, S. L. Chuang, T. Tanbun-Ek, T. K. Chen, and M. Sergent, "Optical gain and refractive index of a laser amplifier in the presence of pump light for cross-gain and cross-phase modulation," *IEEE Photon. Technol. Lett.*, vol. 9, pp. 1358-1360, 1997.
14. S. H. Park and S. L. Chuang, "Many-body optical gain of wurtzite GaN-based quantum-well lasers and comparison with experiment," *Appl. Phys. Lett.*, vol. 72, pp. 287-289, 1998.
15. S. H. Park and S. L. Chuang, "Piezoelectric effects on electrical and optical properties of wurtzite GaN/AlGaIn quantum well lasers," *Appl. Phys. Lett.*, vol. 72, pp. 3103-3105, 1998.
16. T. Tanbun-Ek, S. N. G. Chu, P. W. Wisk, R. Pawelek, A. M. Sergent, J. Minch, E. Young, and S. L. Chuang, "High performance buried heterostructure 1.55  $\mu\text{m}$  wavelength AlGaInAs/InP multiple quantum well lasers grown entirely by MOVPE technique," *Photon. Technol. Lett.*, (submitted, 1998).
17. S. H. Park, and S. L. Chuang, "Crystal orientation effects on piezoelectric field and electronic properties of strained wurtzite semiconductors," *Phys. Rev. B*, vol. 59, pp. 4725-4737, 1999.
18. J. Minch, S. H. Park, J. Minch, X. Jin, and S. L. Chuang, "Theory and Experiment of InGaAsP and InGaAlAs long-wavelength strained quantum-well lasers," *IEEE J. Quant. Electron.*, vol. 35, May 1999 (in press).
19. T. Keating, S. H. Park, J. Minch, X. Jin, and S. L. Chuang, "Optical gain measurements based on fundamental properties and comparison with many-body theory," *J. Appl. Phys.* (submitted, 1998).
20. A. Hsu, S. L. Chuang, W. Fang, L. Adams, G. Nykolak, and T. Tanbun-Ek, "A Wavelength-Tunable Curved Waveguide DFB Laser with Integrated Modulator," *IEEE J. Quant. Electron.*, vol. 35, June 1999 (in press).

21. T. Keating, X. Jin, S. L. Chuang, and K. Hess, "Temperature dependence of electrical and optical modulation responses of quantum-well lasers," *IEEE J. Quantum Electron.*, (submitted, 1999).

**ii) Book Chapter:**

22. S. L. Chuang, "GaAs optoelectronic integrated circuits and future applications," in *GaAs Datareview*, Institution of Electrical Engineers, London, pp. 925-930, 1997.

**B) Presentations:**

23. J. Minch, C. S. Chang, W. Fang, S. L. Chuang, Y. K. Chen, and T. Tanbun-Ek, "Theory and experiment on the amplified spontaneous emission from DFB lasers," *Conference on Lasers and Electro-Optics*, Anaheim, CA, June 2-7, 1996.
24. W. Fang, C. G. Bethea, Y. K. Chen, T. Tanbun-Ek, and S. L. Chuang, "Measurements of spatially dependent carrier lifetimes in 1.55  $\mu\text{m}$  DFB quantum-well lasers using microwave modulation," *Conference on Lasers and Electro-Optics*, Anaheim, CA, June 2-7, 1996.
25. J.-F. P. Seurin and S. L. Chuang, "Discrete Bessel transform and beam propagation method for modeling of vertical-cavity surface-emitting lasers," *Opt. Soc. Am. Annual Meeting*, Rochester, NY, October 20-24, 1996.
- 26.\* S. L. Chuang, C. S. Chang, J. Minch, and W. Fang, "Amplified spontaneous emission spectroscopy of strained quantum-well lasers-Theory and experiment," *Optoelectronics'97 Symposium*, San Jose, Feb. 1997. (Invited).
27. W. Fang, S. L. Chuang, T. Tanbun-Ek, and Y. K. Chen, "Modeling and experiment of 1.55  $\mu\text{m}$  integrated electroabsorption modulator with distributed-feedback lasers," *SPIE*, vol. 3006, Edited by Y. S. Park and R. V. Ramaswamy, *Photonics West*, Optoelectronics'97 Symposium, San Jose, Feb. 1997.
28. J. Minch, C. S. Chang, and S. L. Chuang, "Wavelength conversion using distributed-feedback lasers," *Conference on Lasers and Electro-Optics*, Baltimore, MD, May, 1997.
29. J. Minch, C. S. Chang, and S. L. Chuang, "Wavelength conversion using two-pump four-wave mixing in a double-mode distributed-feedback laser," *Laser and Electro-optics Society Annual Meeting*, MN3, San Francisco, CA, Nov. 10-13, 1997.
30. T. Keating, J. Minch, C. S. Chang, and S. L. Chuang, "Optimal refractive index changes for cross-gain modulation and cross-phase modulation," *Photonics West*, Physics and Simulation of Optoelectronic Devices VI, San Jose, CA, 1998.
31. A. Hsu, W. Fang, S. L. Chuang, T. Tanbun-Ek, C. Bethea, and R. People, "Integrated tunable laser with mode selection modulator," *Photonics West*, Optoelectronic Integrated Circuits II, SPIE, vol. 3290, Edited by S. Y. Wang and Y. S. Park, San Jose, CA, 1998.
32. S. H. Park and S. L. Chuang, "Many-body optical gain of wurtzite InGa<sub>N</sub> quantum-well lasers," *Integrated Photonic Research.*, Victoria, Canada, April 1998.
33. A. Hsu, W. Fang, and S. L. Chuang, "Modeling of normal and backward integrated electroabsorption modulator and laser," *Integrated Photonic Research.*, Victoria, Canada, April 1998.
- 34.\* S. L. Chuang, "Quantum beat in a Wannier-Stark ladder," *International Workshop on Coherent Control of Charge Carrier Dynamics in Semiconductors*, Chicago, May 1998.

- 35.\* S. L. Chuang, "Terahertz generation due to charge oscillations in quantum wells and coherent control," *ONR and TAMU Workshop on Quantum Optics*, Jackson Hole, Wyoming, August 1998.
- 36.\* S. L. Chuang, S. H. Park, J. Minch, and T. Keating, "Strained zinc-blende and wurtzite quantum-well lasers: theory and comparison with experiment," *Semiconductor Science and Technology*'98, La Jolla, CA, Sept. 1998.
37. S. H. Park and S. L. Chuang, "Structural dependences of many-body optical gain with piezoelectric field effects in wurtzite GaN/AlGaIn quantum-well lasers," *Photonics West, Physics and Simulation of Optoelectronic Devices VII*, San Jose, CA, Jan. 1999.
38. E. Young, J. Minch, and S. L. Chuang, "Polarization resolved four-wave mixing in a distributed-feedback laser," *Photonics West, Physics and Simulation of Optoelectronic Devices VII*, San Jose, CA, Jan. 1999.
39. A. Hsu and S. L. Chuang, "Wavelength conversion by cross-absorption modulation using an integrated electroabsorption modulator / laser," *Conference on Lasers and Electro-Optics*, Baltimore, MD, May 1999.
40. X. Jin, T. Keating, and S. L. Chuang, "High-speed optical and gain modulation of quantum-well lasers," *Integrated Photonics Research*, Santa Barbara, CA, July 1999 (submitted).
- 41.\* S. L. Chuang, "Measurements of optical gain spectrum and comparison with many-body theory," *Opt. Soc. Am. Annual Meeting*, Sept. 1999.
- 42.\* S. L. Chuang, "Determination of carrier density and Fermi level separation in semiconductor structures," *The Rank Prize Funds Symposium on Optical Gain and Recombination in Semiconductors*, Grasmere, U.K., Oct. 18-21 1999.

\* invited talk

## ATTACHMENTS

Five major representative publications

# Theory and Experiment of $\text{In}_{1-x}\text{Ga}_x\text{As}_y\text{P}_{1-y}$ and $\text{In}_{1-x-y}\text{Ga}_x\text{Al}_y\text{As}$ Long-Wavelength Strained Quantum-Well Lasers

J. Minch, S. H. Park, T. Keating, and S. L. Chuang

**Abstract**—We present a comprehensive model for the calculation of the bandedge profile of both the  $\text{In}_{1-x}\text{Ga}_x\text{As}_y\text{P}_{1-y}$  and  $\text{In}_{1-x-y}\text{Ga}_x\text{Al}_y\text{As}$  quantum-well systems with an arbitrary composition. Using a many-body optical gain model, we compare the measured net modal gain for both material systems with calculations from the realistic band structure including valence band mixing effects. Calibrated measurements of the side light spontaneous emission spectrum based on its fundamental relation to the optical gain spectrum give values for the radiative current density. These measurements allow us to extract the relationship between total current density and carrier density. A fit of this relation yields values for the Auger coefficient for each material system.

**Index Terms**— Auger recombination, gain,  $\text{InGaAsP}$ ,  $\text{InGaAlAs}$ , semiconductor lasers, strained quantum-well lasers.

## I. INTRODUCTION

THERE are two main material systems used to fabricate long-wavelength semiconductor lasers. While the  $\text{In}_{1-x}\text{Ga}_x\text{As}_y\text{P}_{1-y}$  system has been firmly established as a candidate for high-performance lasers [1], [2], the  $\text{In}_{1-x-y}\text{Ga}_x\text{Al}_y\text{As}$  system has only recently begun to yield quality results [3]–[5]. The interest in the  $\text{In}_{1-x-y}\text{Ga}_x\text{Al}_y\text{As}$  system stems from its larger conduction band offset of  $\Delta E_c/\Delta E_g = 0.7$  compared to a value of  $\Delta E_c/\Delta E_g = 0.4$  for  $\text{In}_{1-x}\text{Ga}_x\text{As}_y\text{P}_{1-y}$ . This larger conduction band offset had been predicted to result in better electron confinement in the conduction band and, therefore, a higher temperature stability.

Previous reports have been given on the model for the band structure of these two systems [6], theoretical calculations comparing the systems in terms of threshold current density and differential gain [7], as well as the temperature dependence of the threshold current [8]. There have also been measurements of the contributions of the various recombination mechanisms for each system [9]. However,

little has been published directly comparing the gain and recombination mechanisms of these two systems, or comparing the existing many-body optical gain models with experimental measurements.

In this paper, we present a comprehensive model for the calculation of the band structure of samples made of either of these systems with an arbitrary composition. Then, using a many-body model for the optical gain and spontaneous emission, we compare the model to experimental data for each material system. Also, from simultaneous measurements of both the spontaneous emission spectrum from the side of the lasers and the gain spectrum from the facet emission, we are able to compare the relative contributions of the different recombination mechanisms in each laser system.

In Section II, we present our model for the calculation of the bandedge of each material system and the quantum-well (QW) band edge discontinuities, followed by the model for the optical gain and spontaneous emission. In Section III, we describe the structure of the lasers as well as our experimental measurements. Section IV describes the comparison of the optical gain data with calculations using our model, and the extraction of the relative contributions of the recombination mechanisms in each system. Finally, a brief conclusion is given in Section V.

## II. THEORETICAL MODEL

### A. Calculation of Bulk Bandgap with Strain

To obtain most parameters for both the  $\text{In}_{1-x}\text{Ga}_x\text{As}_y\text{P}_{1-y}$  and  $\text{In}_{1-x-y}\text{Ga}_x\text{Al}_y\text{As}$  material systems, a linear interpolation between the parameters of the relevant binary semiconductors is used. The interpolation formulas for all physical parameters  $P$  used in the calculation of the band edge, except for the bandgap, are given as [10], [11]

$$\begin{aligned} P(\text{In}_{1-x}\text{Ga}_x\text{As}_y\text{P}_{1-y}) \\ = P(\text{GaAs})xy + P(\text{GaP})x(1-y) + P(\text{InAs})(1-x)y \\ + P(\text{InP})(1-x)(1-y) \end{aligned} \quad (1)$$

$$\begin{aligned} P(\text{In}_{1-x-y}\text{Ga}_x\text{Al}_y\text{As}) \\ = P(\text{InAs})(1-x-y) + P(\text{GaAs})x + P(\text{AlAs})y. \end{aligned} \quad (2)$$

The material parameters of the binary semiconductors can be found in Table I.

Manuscript received July 27, 1998; revised December 1, 1998. This work was supported by the Office of Naval Research under Grant N00014-96-1-0303 and by AASERT under Grant N00014-96-1-0902. The work of S. H. Park was supported by the Catholic University of Taegu-Hyosung.

J. Minch, T. Keating, and S. L. Chuang are with the Department of Electrical and Computer Engineering, University of Illinois at Urbana-Champaign, Urbana, IL 61801 USA.

S. H. Park is with the Department of Electrical and Computer Engineering, University of Illinois at Urbana-Champaign, Urbana, IL 61801 USA, on leave from the Department of Physics, Catholic University of Taegu-Hyosang, Hayang, Kyeongbuk, Korea.

Publisher Item Identifier S 0018-9197(99)03414-4.

TABLE I  
PARAMETERS FOR THE CALCULATION OF STRAIN AND BANDGAP ENERGY FOR THE  $\text{In}_{1-x}\text{Ga}_x\text{As}_y\text{P}_{1-y}$  AND  $\text{In}_{1-x-y}\text{Ga}_x\text{Al}_y\text{As}$  MATERIAL SYSTEMS [10], [11]

Parameter	Symbol(unit)	GaAs	InAs	InP	GaP	AlAs
Lattice Constant	$a(\text{\AA})$	5.6533	6.0584	5.8688	5.4505	5.660
Elastic Stiffness Constant	$C_{11}(10^{11}\text{dyn/cm}^2)$	11.879	8.329	10.11	14.05	12.5
Elastic Stiffness Constant	$C_{12}(10^{11}\text{dyn/cm}^2)$	5.376	4.526	5.61	6.203	5.34
Hydrostatic deformation potential						
for conduction band	$a_c(\text{eV})$	-7.17	-5.08	-5.04	-7.14	-5.64
for valence band	$a_v(\text{eV})$	1.16	1.00	1.27	1.70	2.47
Shear deformation potential						
for valence band	$b(\text{eV})$	-1.7	-1.8	-1.7	-1.8	-1.5
Valence band parameter	$\gamma_1$	6.8	20.4	4.95	4.05	3.45
	$\gamma_2$	1.9	8.3	1.65	0.49	0.68
	$\gamma_3$	2.73	9.1	2.35	1.25	1.29
Electron effective mass	$m_e/m_0$	0.067	0.023	0.077	0.25	0.15
Heavy-hole effective mass	$m_{hh}/m_0$	0.50	0.40	0.60	0.67	0.79

The one exception to the linear interpolation is the formula for the unstrained bandgap. For each material system, this quantity is given as

$$\begin{aligned} \text{In}_{1-x}\text{Ga}_x\text{As}_y\text{P}_{1-y}E_g(x, y) \\ = 1.35 + 0.642x - 1.101y + 0.758x^2 + 0.101y^2 \\ - 0.159xy - 0.28x^2y + 0.109xy^2 \text{ (eV)} \end{aligned} \quad (3)$$

$$\begin{aligned} \text{In}_{1-x-y}\text{Ga}_x\text{Al}_y\text{As}E_g(x, y) \\ = 0.36 + 2.093y + 0.629x + 0.577y^2 + 0.436x^2 \\ + 1.013xy - 2.0xy(1 - x - y) \text{ (eV)}. \end{aligned} \quad (4)$$

The effects of strain are calculated in the following way. First, the strain in the plane of the epitaxial growth is

$$\epsilon = \epsilon_{xx} = \epsilon_{yy} = \frac{a_0 - a}{a} \quad (5)$$

where  $a$  is the lattice constant of the quaternary epitaxial layer and  $a_0$  is the lattice constant of the substrate which is assumed to be InP. The strain in the perpendicular direction can be expressed as

$$\epsilon_{zz} = -2\frac{C_{12}}{C_{11}}\epsilon \quad (6)$$

where  $C_{11}$  and  $C_{12}$  are the elastic stiffness constants. The conduction band is shifted by the energy

$$\delta E_c(x, y) = a_c(\epsilon_{xx} + \epsilon_{yy} + \epsilon_{zz}) = 2a_c\left(1 - \frac{C_{12}}{C_{11}}\right)\epsilon \quad (7)$$

and the valence bands are shifted by

$$\delta E_{hh}(x, y) = -P_c - Q_c \quad (8)$$

$$\delta E_{lh}(x, y) = -P_c + Q_c \quad (9)$$

where

$$P_c = -a_v(\epsilon_{xx} + \epsilon_{yy} + \epsilon_{zz}) \quad (10)$$

$$= -2a_v\left(1 - \frac{C_{12}}{C_{11}}\right)\epsilon \quad (11)$$

$$Q_c = -\frac{b}{2}(\epsilon_{xx} + \epsilon_{yy} - 2\epsilon_{zz}) \quad (12)$$

$$= -b\left(1 + 2\frac{C_{12}}{C_{11}}\right)\epsilon \quad (13)$$

where  $a_c$  and  $a_v$  are the conduction-band and valence-band hydrostatic deformation potentials, and  $b$  is the valence-band shear deformation potential.

The strained bandgaps can then be expressed as

$$E_{c-hh}(x, y) = E_g(x, y) + \delta E_c(x, y) - \delta E_{hh}(x, y) \quad (14)$$

and

$$E_{c-lh}(x, y) = E_g(x, y) + \delta E_c(x, y) - \delta E_{lh}(x, y). \quad (15)$$

Fig. 1(a) shows a contour plot relating  $x$  and  $y$  to the strain and energy gap of the  $\text{In}_{1-x}\text{Ga}_x\text{As}_y\text{P}_{1-y}$  system grown on an InP substrate. Fig. 1(b) shows the same information, but inverted, so that, given a strain and a bandgap, the Ga and As mole fractions can be obtained. Fig. 2(a) and (b) shows the results for the  $\text{In}_{1-x-y}\text{Ga}_x\text{Al}_y\text{As}$  system with an InP substrate. In all of these figures, the bandgap with the smallest energy is presented (i.e.,  $c-hh$  for compressive strain,  $c-lh$  for tensile strain) and the bandgap shift due to the strain effects is taken into account. Note that these results are different from a conventional plot where the "unstrained" bandgap energy is usually presented.

#### B. Calculation of Band Offset

When modeling the bandstructure for a QW, the relative alignment of the band edges of the well and barrier material is very important. Unfortunately, there are few data for arbitrary compositions of these two quaternary material systems, especially for the strained cases. Here we present and compare two models for the band alignment of these systems.

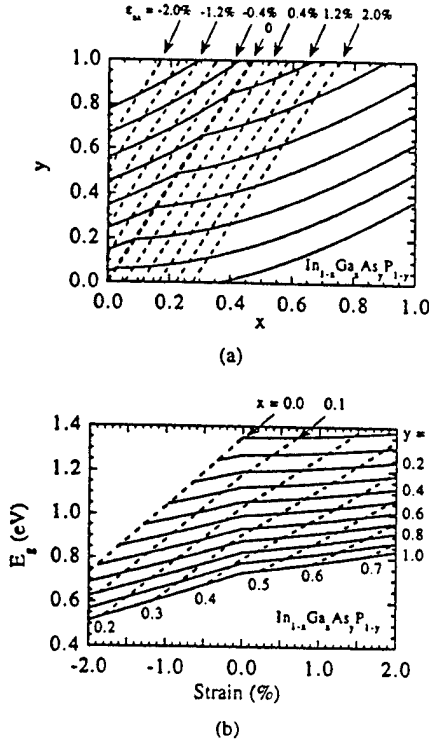


Fig. 1. Strain and strained bandgap energy versus Ga ( $x$ ) and As ( $y$ ) mole fractions for the  $\text{In}_{1-x}\text{Ga}_x\text{As}_y\text{P}_{1-y}$  material system with (a) contours of constant strain and bandgap energy and (b) contours of constant  $x$  and  $y$ .

1) *Model-Solid Theory* [10], [12]: The valence band position of a quaternary is given by

$$E_v(x, y) = \begin{cases} E_{v,av}(x, y) + \frac{\Delta(x, y)}{3} + \delta E_{hh}(x, y), & \text{for } hh \text{ (compressive strain)} \\ E_{v,av}(x, y) + \frac{\Delta(x, y)}{3} + \delta E_{lh}(x, y), & \text{for } lh \text{ (tensile strain)} \end{cases} \quad (16)$$

where  $E_{v,av}(x, y)$  is the average valence subband energy and  $\Delta$  is the spin-orbit split-off band energy. These values are obtained by a linear interpolation [see (1) or (2)] of the binary values listed in Table II. The conduction band position may be calculated by simply adding the strained bandgap energy to the valence band position

$$E_c(x, y) = \begin{cases} E_v(x, y) + E_{c-hh}(x, y), & \text{for } hh \text{ (compressive strain)} \\ E_v(x, y) + E_{c-lh}(x, y), & \text{for } lh \text{ (tensile strain)} \end{cases} \quad (17)$$

The conduction band offset is given by

$$\frac{\Delta E_c}{\Delta E_g} = 1 - \frac{E_v^w - E_v^b}{E_g^b - E_g^w} \quad (18)$$

where  $E_v^w$  and  $E_v^b$  are the valence band positions in the well and barrier materials, respectively, and  $E_g^w$  and  $E_g^b$  are the strain adjusted band gaps ( $E_{c-hh}$  for compressive strain and  $E_{c-lh}$  for tensile strain) for the well and barrier materials.

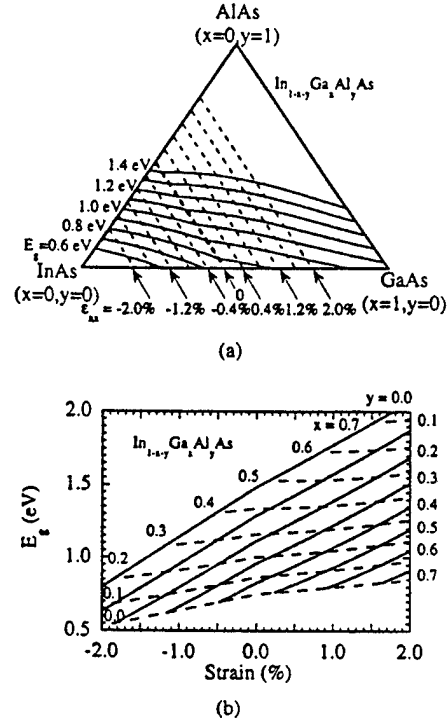


Fig. 2. Strain and strained bandgap energy versus Ga ( $x$ ) and Al ( $y$ ) mole fractions for the  $\text{In}_{1-x-y}\text{Ga}_x\text{Al}_y\text{As}$  material system with (a) contours of constant strain and bandgap energy and (b) contours of constant  $x$  and  $y$ .

2) *Harrison's Model* [13]: The position of both the conduction and valence bands are determined by

$$E_v(x, y) = \begin{cases} E_v^H(x, y) + \delta E_{hh}(x, y), & \text{for } hh \text{ (compressive strain)} \\ E_v^H(x, y) + \delta E_{lh}(x, y), & \text{for } lh \text{ (tensile strain)} \end{cases} \quad (19)$$

$$E_c(x, y) = E_c^H + \delta E_c(x, y) \quad (20)$$

where  $E_v^H(x, y)$  and  $E_c^H(x, y)$  are obtained by a linear interpolation of the binary parameters found in Table II, and  $\delta E_{hh}(x, y)$ ,  $\delta E_{lh}(x, y)$ , and  $\delta E_c(x, y)$  are the strain-induced energy shifts given in (7)–(9). The superscript “H” refers to Harrison's model. The conduction band-edge discontinuity may then be calculated as

$$\frac{\Delta E_c}{\Delta E_g} = \frac{E_c^{H,b} - E_c^{H,w}}{(E_v^{H,w} - E_v^{H,b}) + (E_c^{H,b} - E_c^{H,w})} \quad (21)$$

where the superscripts  $w$  and  $b$  indicate the well and barrier materials, respectively.

It should be noted that this method simply is meant to give the parameter  $\Delta E_c/\Delta E_g$  which may be used to determine the alignment of the well and barrier materials. The difference between  $E_v(x, y)$  and  $E_c(x, y)$  from (19) and (20) should not be used to calculate the bandgap of the quaternary material. Rather, (3) and (4) should be used.

Fig. 3 shows a comparison of the model-solid theory and Harrison's model for the calculation of the conduction band offset for both lattice-matched  $\text{In}_{1-x}\text{Ga}_x\text{As}_y\text{P}_{1-y}$  and  $\text{In}_{1-x-y}\text{Ga}_x\text{Al}_y\text{As}$ . Also shown are empirical curves (solid) based on experimental measurements of these quantities [14], [15]. For the  $\text{In}_{1-x}\text{Ga}_x\text{As}_y\text{P}_{1-y}$  system, Harrison's

TABLE II  
PARAMETERS FOR THE CALCULATION OF BAND ALIGNMENT OF THE  $\text{In}_{1-x}\text{Ga}_x\text{As}_y\text{P}_{1-y}$  AND  $\text{In}_{1-x-y}\text{Ga}_x\text{Al}_y\text{As}$  MATERIAL SYSTEMS USING THE MODEL-SOLID THEORY [12] AND HARRISON'S MODEL [13]

Parameter	Symbol(unit)	GaAs	InAs	InP	GaP	AlAs
Model-solid theory:						
Average valence band position	$E_{v,av}(\text{eV})$	-6.92	-6.67	-7.04	-7.40	-7.49
Spin-orbit split-off energy	$\Delta(\text{eV})$	0.34	0.38	0.11	0.08	0.28
Harrison's model:						
Conduction band position	$E_c^H(\text{eV})$	1.53	0.801	1.35	2.352	2.5255
Valence band position	$E_v^H(\text{eV})$	0.111	0.441	0.00	-0.388	-0.4245

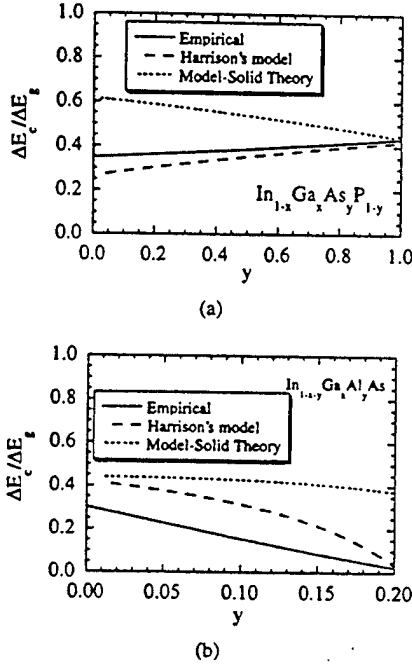


Fig. 3. The conduction band offset for (a)  $\text{In}_{1-x}\text{Ga}_x\text{As}_y\text{P}_{1-y}$  and (b)  $\text{In}_{1-x-y}\text{Ga}_x\text{Al}_y\text{As}$  lattice-matched to InP. The solid lines show empirical results [14], [15] obtained from experimental data. Dashed lines show calculations using the model-solid theory and Harrison's model.

model is excellent while the model-solid theory gives the opposite trend, only being good near the InGaAs boundary. For  $\text{In}_{1-x-y}\text{Ga}_x\text{Al}_y\text{As}$ , both models have some error, but Harrison's model is again closer to the empirical curve. For the calculations of the band structure in this paper, we therefore have chosen to use Harrison's model.

### C. Calculation of Band Structure and Gain

The optical gain with many-body effects is calculated by a non-Markovian model [16]. The plasma screening, bandgap renormalization (BGR), and the excitonic or the Coulomb enhancement (CE) of the interband transition probability are included in the model. The valence band structure is calculated by using the block-diagonalized  $3 \times 3$  Hamiltonian based on the  $\mathbf{k} \cdot \mathbf{p}$  method [17]. Aside from the conduction band effective mass for the  $\text{In}_{1-x}\text{Ga}_x\text{As}_y\text{P}_{1-y}$  system, parameters used in the calculation are interpolated using (1) and (2) and the

binary parameters summarized in Table I. The conduction band effective mass for  $\text{In}_{1-x}\text{Ga}_x\text{As}_y\text{P}_{1-y}$  is given as

$$m_e(\text{In}_{1-x}\text{Ga}_x\text{As}_y\text{P}_{1-y}) = 0.08 - 0.116x + 0.026y - 0.059xy + (0.064 - 0.02x)y^2 + (0.06 + 0.032y)x^2. \quad (22)$$

The optical gain spectra are related to the spontaneous emission spectra from the detailed balance [18], [19] between absorption and emission of photons. This means that there is a transparency point in the gain spectra that is determined by the Fermi level separation  $\Delta F$  that suggests the carriers are in a quasi-equilibrium distribution. The following fundamental relationship [18], [19] is then used to calculate the optical gain:

$$g(\omega) = \left[ 1 - \exp\left(\frac{\hbar\omega - \Delta F}{kT}\right) \right] g_{sp}(\omega) \quad (23)$$

$$g_{sp}(\omega) = \frac{\pi^2 c^2}{n^2 \omega^2} r_{sp}(\omega) \quad (24)$$

where  $\Delta F$  is the quasi-Fermi level separation,  $k$  is Boltzmann's constant,  $T$  is the device temperature,  $c$  is the speed of light,  $n$  is the effective refractive index of the optical waveguide mode, and  $r_{sp}(\omega)$  is the spontaneous emission rate. The spontaneous emission coefficient  $g_{sp}(\omega)$  taking into account the non-Markovian relaxation and the many-body effects is given by [16]

$$g_{sp}(\omega) = \sqrt{\frac{\mu_0}{\epsilon}} \left( \frac{e^2}{m_0^2 \omega} \right) \int_0^\infty dk_{\parallel} \frac{k_{\parallel}}{\pi L_z} |M_{lm}|^2 f_l^c(k_{\parallel}) \times (1 - f_m^v(k_{\parallel}))(1 - \text{Re}q_{k_{\parallel}}) \times \frac{\text{Re}L(E_{lm}(k_{\parallel})) - \text{Im}q_{k_{\parallel}} \text{Im}L(E_{lm}(k_{\parallel}))}{(1 - \text{Re}q_{k_{\parallel}})^2 + (\text{Im}q_{k_{\parallel}})^2} \quad (25)$$

where  $\omega$  is the angular frequency,  $\mu_0$  is the vacuum permeability,  $\epsilon$  is the dielectric constant,  $k_{\parallel}$  is the in-plane wavevector,  $L_z$  is the well thickness,  $|M_{lm}|^2$  is the momentum matrix element in the strained QW,  $f_l^c$  and  $f_m^v$  are the Fermi function for the conduction band states and the valence band states, and  $\hbar$  is the reduced Planck's constant. The indices  $l$  and  $m$  denote the electron states in the conduction band and the heavy hole (light hole) subband states in the valence band. Also,

TABLE III  
A SUMMARY OF THE STRUCTURE OF THE THREE LASER SYSTEMS STUDIED

Sample A	Well:	Number of wells	7	SCH width:	700Å
		Material	InGaAsP	Stripe width:	1.2μm
		Strain	-0.9% compressive	Cavity length:	350μm
		Width	80Å		
		PL wavelength	1.58μm		
	Barrier:	Material	InGaAsP		
		Strain	lattice matched		
		Width	80Å		
		PL wavelength	1.255μm		
Sample B	Well:	Number of wells	5	SCH width:	1000Å
		Material	InGaAlAs	Stripe width:	1.5μm
		Strain	-0.78% compressive	Cavity length:	890μm
		Width	54Å		
		PL wavelength	1.56μm		
	Barrier:	Material	InGaAlAs		
		Strain	lattice matched		
		Width	57Å		
		PL wavelength	1.21μm		
Sample C	Well:	Number of wells	5	SCH width:	600Å
		Material	InGaAlAs	Stripe width:	1.46μm
		Strain	lattice matched	Cavity length:	638μm
		Width	86Å		
		PL wavelength	1.56μm		
	Barrier:	Material	InGaAlAs		
		Strain	lattice matched		
		Width	50Å		
		PL wavelength	1.21μm		

$E_{lm}(k_{||}) = E_l^c(k_{||}) - E_m^v(k_{||}) + E_g + \Delta E_{SX} + \Delta E_{CH} - \hbar\omega$  is the renormalized transition energy between electrons and holes, where  $E_g$  is the bandgap of the material, and  $\Delta E_{SX}$  and  $\Delta E_{CH}$  are the screened exchange and Coulomb-hole contributions [21] to the bandgap renormalization. The factor  $q_{k_{||}}$  accounts for the excitonic or Coulomb enhancement of the interband transition probability [20], [21]. The lineshape function is Gaussian for the simplest non-Markovian quantum kinetics and is given by [16]

$$\text{Re}L(E_{lm}(k_{||})) = \sqrt{\frac{\pi\tau_{in}(k_{||})\tau_c}{2\hbar^2}} \exp\left(-\frac{\tau_{in}(k_{||})\tau_c}{2\hbar^2} E_{lm}^2(k_{||})\right) \quad (26)$$

and

$$\text{Im}L(E_{lm}(k_{||})) = \frac{\tau_c}{\hbar} \int_0^\infty \exp\left(-\frac{\tau_c}{2\tau_{in}(k_{||})} t^2\right) \cdot \sin\left(\frac{\tau_c E_{lm}(k_{||})}{\hbar} t\right) dt. \quad (27)$$

The intraband relaxation time  $\tau_{in}$  and correlation time  $\tau_c$  are assumed to be constant and used as fitting parameters.

### III. EXPERIMENTS

#### A. Laser Structures

In our experiments, we perform measurements using lasers with three types of active regions. First, we tested a buried heterostructure laser with five lattice-matched QW's made of the  $\text{In}_{1-x-y}\text{Ga}_x\text{Al}_y\text{As}$  material system, as well as a buried heterostructure laser with five -0.78% compressively strained QW's of the same system. Details on the growth and fabrication of these devices can be found elsewhere [5]. Also tested was a buried heterostructure laser with seven -0.9% compressively strained QW's made of the  $\text{In}_{1-x}\text{Ga}_x\text{As}_y\text{P}_{1-y}$  material system. Table III contains detailed information for the structure of each active region.

#### B. Experimental Procedure

The facet emission spectrum of each laser was measured for various currents below lasing threshold. The device under test is mounted on a heat sink and is held at a constant temperature of 25 °C using a thermoelectric cooling unit. The current

to the device was supplied by an ILX Lightwave LDX-3412 current source and monitored to the hundredth of a milliamp using a Fluke 87 III digital multimeter. The facet output was collected using an E-TEK Dynamics laser optical fiber interface with a built-in polarizer to control the polarization of the measured emission. An optical isolator was used to prevent optical feedback effects and the light was monitored using an HP 70951B optical spectrum analyzer with a spectral resolution of 0.08 nm. The net modal gain for these devices was obtained using the well known Hakki-Paoli method [22] in which the ratio of the maximum  $I_{\max}$  and minimum  $I_{\min}$  of the amplified spontaneous emission spectrum yields the net modal gain  $G_{\text{net}}$  by the following relations:

$$G_{\text{net}} = \Gamma g - \alpha_i = \frac{1}{L} \ln \left( \frac{S-1}{S+1} \right) + \frac{1}{2L} \ln \left( \frac{1}{R_1 R_2} \right) \quad (28)$$

$$S = \sqrt{\frac{I_{\max}}{I_{\min}}} \quad (29)$$

where  $g$  is the material gain for one well,  $\Gamma (=N_w \Gamma_w)$  is the optical confinement factor per well ( $\Gamma_w$ ) multiplied by  $N_w$ , the number of wells,  $\alpha_i$  is the intrinsic loss,  $L$  is the cavity length, and  $R_1$  and  $R_2$  are the facet power reflectivities.

The side light spontaneous emission [24] of the same device was also monitored for currents up to lasing threshold. In this measurement, a cleaved multimode fiber is brought up close to the side of the device, usually near the middle in order to avoid scattered light from the laser facets. First, using the same equipment as for the gain, the spontaneous emission spectrum is taken using a resolution bandwidth of 10 nm for each of the currents at which the facet emission was measured. Next, the current is controlled using an HP 4145 semiconductor parameter analyzer in order to achieve currents as low as 20  $\mu\text{A}$ . The current is swept and the light captured by the fiber is then fed into an HP 8153A Lightwave Multimeter to obtain the integrated spontaneous emission power. For these measurements, the width of the active region is sufficiently small (1.2–1.46  $\mu\text{m}$ ) so that amplification of the SE spectra is negligible.

#### IV. ANALYSIS AND DISCUSSION

The measured net modal gain obtained from the amplified spontaneous emission (ASE) spectrum using (28) for each of the three material systems studied is presented in Fig. 4 for several currents up to threshold. Typical mode spacings in the ASE spectrum for samples A, B, and C are about 0.93, 0.38, and 0.51 nm, respectively. To check for the effects of spectrometer resolution on the measured net modal gain, the min/sum method [23], which is less sensitive to the resolution limits of the measurement (although more sensitive to noise), was also used to extract the gain spectra. The resulting spectra were nearly identical except for values closest to the threshold gain value where the Hakki-Paoli method underestimates the gain, but these differences give less than a 5% error on the value of the modal gain.

Also presented in Fig. 4 are calculated spectra using the model presented above for the material gain of the three systems. The intraband relaxation time  $\tau_{\text{in}}$  and the correlation

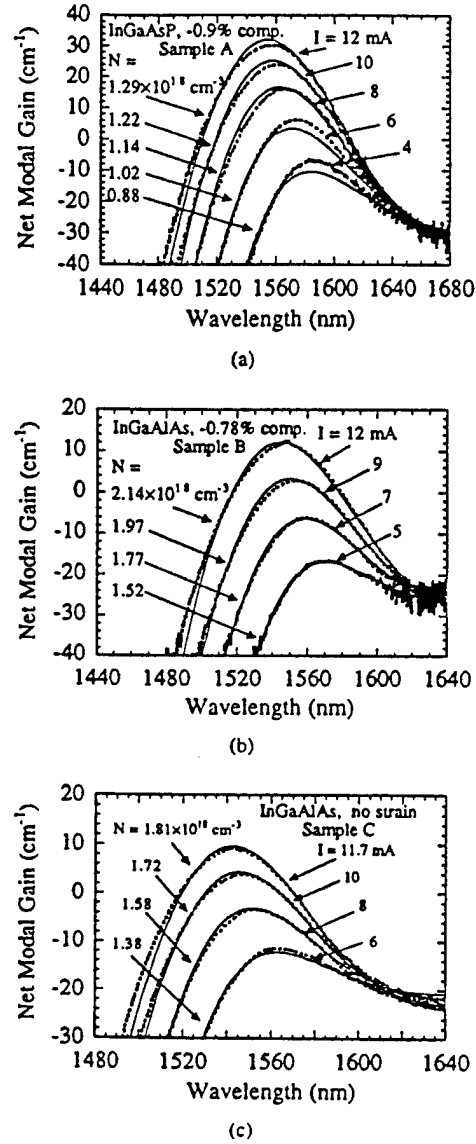


Fig. 4. The measured modal gain (solid lines) and calculated (dashed lines) values from the electronic band structure for (a)  $\text{In}_{1-x}\text{Ga}_x\text{As}_y\text{P}_{1-y}$  with  $-0.9\%$  compressive strain (Sample A), (b)  $\text{In}_{1-x-y}\text{Ga}_x\text{Al}_y\text{As}$  with  $-0.78\%$  compressive strain (Sample B), and (c)  $\text{In}_{1-x-y}\text{Ga}_x\text{Al}_y\text{As}$  lattice matched (Sample C). The device parameters are listed in Table III.

time  $\tau_c$  used for the fits are given in Table IV. For the screened exchange  $\Delta E_{\text{SX}}$  and Coulomb-hole  $\Delta E_{\text{CH}}$  contributions to the bandgap renormalization, [21, eqs. (27) and (28)] were used with a  $C$  parameter of 1.1, 1.7, and 2.0 for Samples A, B, and C, respectively. Each of these parameters affect the peak gain position and overall shape of the spectra. They were selected to yield the best overall fit, balancing these criteria. The net modal gain is obtained using an intrinsic loss which is independent of wavelength, and a confinement factor with a linear dependence on wavelength, with a slope equal to  $1.66 \times 10^{-4} \text{ nm}^{-1}$  (estimated from the wavelength-dependent refractive index and waveguide theory for the fundamental mode) and the vertical intercept treated as a parameter to fit the data.

Fig. 5(a) shows a plot of the fitted values of the intrinsic loss as a function of the injected current for each device.

TABLE IV  
PARAMETERS USED IN AND OBTAINED FROM THE THEORETICAL FITS

Parameter	Symbol	Sample A	Sample B	Sample C
Fit of the modal gain:				
Interband relaxation time	$\tau_{ia}(fs)$	40	60	85
Correlation time	$\tau_c(fs)$	20	20	20
Quasi-Fermi level separation	$\Delta F(eV)$	0.801 (4mA)	0.804 (5mA)	0.806 (6mA)
		0.813 (6mA)	0.815 (7mA)	0.816 (8mA)
		0.822 (8mA)	0.823 (9mA)	0.823 (10mA)
		0.828 (10mA)	0.829 (12mA)	0.827 (11.7mA)
Transformation of spontaneous emission:				
Scaling coefficient	$Q(cm^{-1}nm^{-1}(mW)^{-1})$	$6.11 \times 10^{-7} \pm 0.22 \times 10^{-7}$	$1.81 \times 10^{-7} \pm 0.08 \times 10^{-7}$	$8.2 \times 10^{-8} \pm 0.02 \times 10^{-8}$
Effective index of refraction	$n$	$3.3 \pm 0.15$	$3.3 \pm 0.15$	$3.3 \pm 0.15$
Optical confinement factor	$\Gamma(= N_w\Gamma_w)$	$0.15 \pm 0.02$	$0.06 \pm 0.02$	$0.11 \pm 0.02$
Optical confinement factor per well	$\Gamma_w$	$0.021 \pm 0.0029$	$0.012 \pm 0.004$	$0.022 \pm 0.004$
Fit of the $J_rN$ relationship:				
Coupling coefficient	$K_2$	$1.56 \times 10^{-14} \pm 0.01 \times 10^{-14}$	$1.64 \times 10^{-14} \pm 0.05 \times 10^{-14}$	$1.21 \times 10^{-14} \pm 0.01 \times 10^{-14}$
Monomolecular coefficient	$A(s^{-1})$	$1.1 \times 10^8 \pm 0.2 \times 10^8$	$7 \times 10^7 \pm 2 \times 10^7$	$6.7 \times 10^7 \pm 3 \times 10^7$
Auger coefficient	$C(cm^6s^{-1})$	$1.1 \times 10^{-27} \pm 0.15 \times 10^{-27}$	$1.4 \times 10^{-28} \pm 0.3 \times 10^{-28}$	$3 \times 10^{-28} \pm 2 \times 10^{-28}$
Injection efficiency	$\eta_{inj}$	$0.92 \pm 0.17$	$0.95 \pm 0.15$	$0.45 \pm 0.15$
Characteristic temperature (measured)	$T_0(^{\circ}K)$	38	53	51.4

The observed increase in the loss is consistent with previous reports [25] and can be explained by the increase in free-carrier absorption with an increasing carrier density. The fitted optical confinement factor used for the three devices is shown in Fig. 5(b). Values for the optical confinement factor per well ( $\Gamma_w$ ) and the overall confinement factor ( $\Gamma = N_w\Gamma_w$ ) are listed in Table IV. These fitted values are in good agreement with typical values for InP-based lasers [26] when scaling due to well width is taken into account. Finally, Fig. 5(c) shows a plot of peak net modal gain versus the total current density for each laser system. The fits of the gain spectra of these three material systems allow us to obtain the density of carriers  $N$  in the QW's corresponding to the measured injection currents. For each system, other samples from the same wafer exhibit similar gain spectra.

The same model used to create the gain spectrum was also used to calculate the spontaneous emission rate for each of the material systems studied. The radiative current density can be related to the spontaneous emission rate as

$$J_{rad} = eN_wL_w \int_0^\infty \tau_{spont}(\lambda) d\lambda = eN_wL_w B_{eff} N^2 \quad (30)$$

where  $e$  is the charge on an electron,  $N_w$  is the number of wells,  $L_w$  is the width of a QW,  $\tau_{spont}(\lambda)$  is the spontaneous emission rate,  $B_{eff}$  is the effective radiative recombination coefficient, and  $N$  is the carrier density.  $J_{rad}$  can be obtained from our calculated spontaneous emission spectrum using (30) with

$$\tau_{spont}(\lambda) = \frac{8\pi cn^2}{\lambda^4} g_{sp}(\lambda) \quad (31)$$

where  $g_{sp}(\lambda)$  is given in (25),  $\lambda = 2\pi c/\omega$ ,  $c$  is the speed of light, and  $n$  is the refractive index of the QW. The calculated curves for  $J_{rad}$  of each sample are shown in Fig. 6.

In order to validate these calculations from the band structure, it is important to be able to obtain the radiative current density experimentally. As described above, we measure the spontaneous emission power spectra from the side of each laser device. The spontaneous emission power captured by the optical fiber can be related to the spontaneous emission rate by

$$P(\lambda) = K_1 \frac{hc}{\lambda} \tau_{spont}(\lambda) d\lambda V \quad (32)$$

where  $P(\lambda)$  is the measured power in the fiber,  $K_1$  is a coupling coefficient which includes the fraction of the spontaneous emission captured by the optical fiber,  $h$  is Planck's constant,  $c$  is the speed of light,  $d\lambda$  is the spectrometer resolution, and  $V$  is the active region volume. Since  $K_1$  is an unknown quantity, it is not straightforward to obtain a value for the spontaneous emission rate so that (30) can be used to extract  $J_{rad}$ . A calibration can be accomplished based on the fundamental relationship between the material gain and the spontaneous emission rate [(23) and (24)], rewritten as

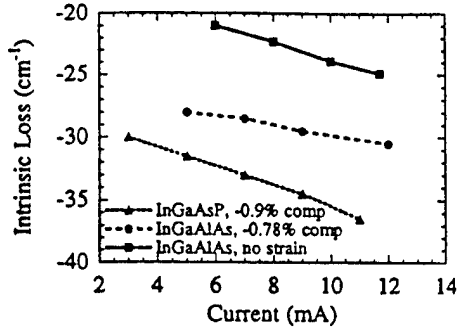
$$g(\lambda) = \frac{\lambda^4}{8\pi cn^2} \left[ 1 - \exp\left(\frac{hc/\lambda - \Delta F}{k_B T}\right) \right] \tau_{spont}(\lambda) \quad (33)$$

where  $n$  is the effective refractive index,  $\Delta F$  is the quasi-Fermi level separation energy,  $k_B$  is Boltzmann's constant, and  $T$  is the temperature. The material gain per well can be related to the measured net modal gain as

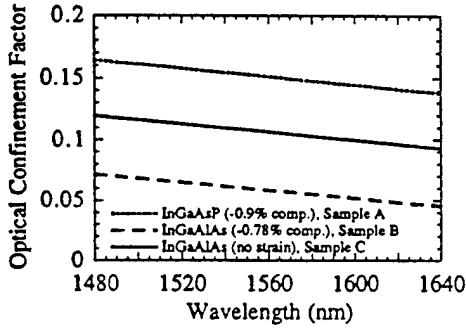
$$G_{net} = \Gamma g(\lambda) - \alpha_i \quad (34)$$

where  $\Gamma$  is the optical confinement factor and  $\alpha_i$  is the intrinsic loss for the optical waveguide mode. Combining (32)–(34), we obtain

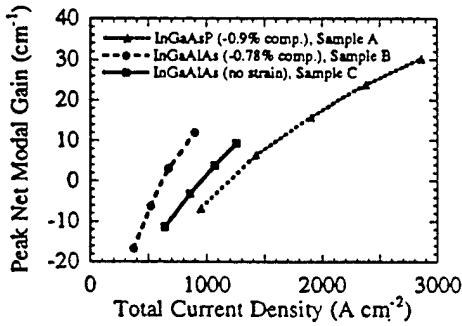
$$G_{net}(\lambda) = Q \lambda^5 \left( 1 - \exp\left(\frac{hc/\lambda - \Delta F}{k_B T}\right) \right) P(\lambda) - \alpha_i \quad (35)$$



(a)



(b)



(c)

Fig. 5. (a) The optical confinement factor and (b) intrinsic loss used in the fits of the modal gain for Samples A, B, and C in Fig. 4. (c) The peak net modal gain versus the total current density.

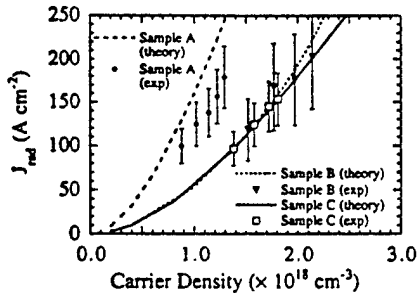
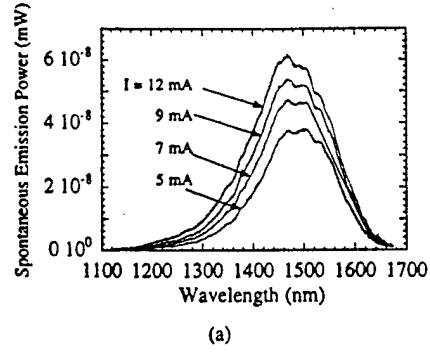


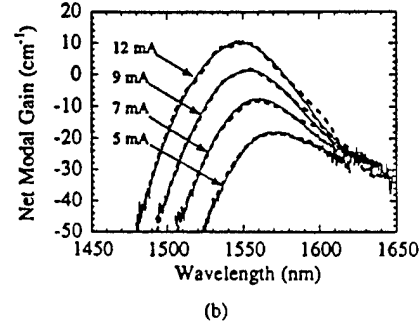
Fig. 6. The calculated total radiative current density through all wells [see (30)] as a function of carrier density (lines) compared to the extracted total radiative current density from the calibrated spontaneous emission spectrum measurements.

where

$$Q = \frac{\Gamma}{8\pi K_1 \hbar c^2 n^2 d \lambda V} \quad (36)$$



(a)



(b)

Fig. 7. (a) The measured spontaneous emission spectra for the -0.78% compressively strained  $\text{In}_{1-x}\text{Ga}_x\text{Al}_y\text{As}$  laser system (Sample B in Table III) and (b) the measured net modal gain spectra (solid lines) compared to the transformed spontaneous emission spectra (dashed lines) using (35).

This equation relates the measured net modal gain to the measured spontaneous emission power using the three parameters  $Q$ ,  $\Delta F$ , and  $\alpha_i$ .  $\Delta F$  and  $\alpha_i$  are not independent, however, since the net modal gain value measured at the wavelength corresponding to  $\Delta F$  is exactly the transparency level and equal to  $\alpha_i$ . (We assume here that the intrinsic loss is independent of wavelength.) Hence, the short-wavelength side of the measured net modal gain spectrum gives the relationship between these two quantities.

Using  $Q$  and  $\Delta F$  as fitting parameters, (35) may then be used to transform the measured spontaneous emission power into the net modal gain spectrum. By choosing the best fit between the measured and transformed net modal gains, an accurate value for  $Q$  can be obtained. As an example of this procedure, Fig. 7(a) shows the spontaneous emission power spectra measured for the compressively strained  $\text{In}_{1-x}\text{Ga}_x\text{Al}_y\text{As}$  system. These spectra were measured for each of the currents that the gain was measured at. The best fits between the transformed spontaneous emission and actually measured net modal gain spectra are shown in Fig. 7(b). The extracted values of  $Q$  are about  $1.8 \times 10^{-7}$  and vary by less than 4% among all of the currents measured, showing excellent uniformity in the measurement of the SE spectra. For  $\Delta F$ , the extracted values for each system deviate from the values obtained for the fitting of the experimental gain curves by less than 0.1% at low currents where the difference between two adjacent curves in Fig. 4 represent a shift of about 1% in  $\Delta F$ . At higher currents, the deviation gets as large as 0.45% while the separation between curves is about 0.5%.

Once accurate values of  $Q$  have been extracted, the measured spontaneous emission power spectra can be calibrated

in the following way to get the actual spontaneous emission rate. By solving (32),  $\tau_{\text{spont}}(\lambda)$  can be expressed as

$$\tau_{\text{spont}}(\lambda) = T\lambda P(\lambda) \quad (37)$$

where

$$T = \frac{8\pi cn^2}{\Gamma} Q. \quad (38)$$

Note that this procedure has eliminated the need to derive the coupling coefficient  $K_1$  explicitly. The data points in Fig. 6 were obtained by substituting (37) and (38) into (30) and numerically integrating the calibrated data. The value for  $n$  was assumed to be 3.3 with an error of 0.15 for each of the material systems measured. The optical confinement factor was assumed to be constant with a value equal to the average of the range used for the gain fits, as shown in Fig. 5(b). The error range is taken from the values of the confinement factor in Fig. 5(b) at the edges of the transformed spontaneous emission spectra. This amounts to an error of about  $\pm 12\%$  for the value of the confinement factor, leading to a total error of slightly over  $\pm 20\%$  for the radiative current density.

From the calculated curves of the radiative current density  $J_{\text{rad}}$  as a function of carrier density  $N$  in Fig. 6, the radiative recombination coefficient  $B_{\text{eff}}$  for each material system is obtained from (30) and is presented in Fig. 8. This parameter is independent of the well width/number product, so it serves as a fair comparison of the relative probability of the radiative recombination of an electron-hole pair for each structure. We see that, at low carrier densities, the compressively strained  $\text{In}_{1-x}\text{Ga}_x\text{As}_y\text{P}_{1-y}$  system has the largest radiative recombination coefficient followed by the compressively strained  $\text{In}_{1-x-y}\text{Ga}_x\text{Al}_y\text{As}$  system and then the lattice-matched  $\text{In}_{1-x-y}\text{Ga}_x\text{Al}_y\text{As}$  system. It is not surprising that the strained samples are more efficient since strain has been shown to decrease the in-plane effective mass in the top ( $hh$ ) valence band, leading to a more symmetric injection of electrons and holes in the conduction and valence bands [27]. Also, the heavy-hole and light-hole subband separation becomes larger with strain, leading to less wasted carriers. At higher carrier densities, all three systems show a decrease in the radiative recombination coefficient. This is especially pronounced in the compressive  $\text{In}_{1-x}\text{Ga}_x\text{As}_y\text{P}_{1-y}$  system. This decrease is probably due to the significant population of higher energy valence subbands while the higher energy conduction subbands are virtually empty. For example, in all of these systems, the second conduction subband has less than 3% of the total carrier population. Meanwhile, for the compressive  $\text{In}_{1-x}\text{Ga}_x\text{As}_y\text{P}_{1-y}$  system, the first two heavy-hole subbands (which are the lowest subbands) have a spacing of 36 meV and a distribution of approximately 60.1% of carriers in the first heavy-hole subband and 29.6% in the second heavy-hole subband. Also, for the compressive  $\text{In}_{1-x-y}\text{Ga}_x\text{Al}_y\text{As}$  sample, there is a spacing of 65 meV between the first two heavy-hole subbands and a carrier distribution of about 80% and 19.4% for the first and second heavy-hole subbands, respectively. This difference is mostly due to the thinner well of the compressive  $\text{In}_{1-x-y}\text{Ga}_x\text{Al}_y\text{As}$  sample. Holes in the second heavy-hole subband are, therefore, unable to

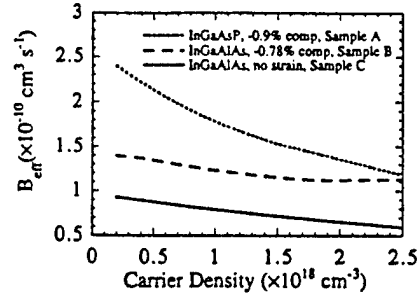


Fig. 8. The radiative recombination coefficient as a function of carrier density extracted from the calculated total radiative current density.

significantly contribute to radiative recombination processes since they can only recombine with electrons in the second conduction subband, which is sparsely populated for each laser system studied. The decrease seen in the compressive  $\text{In}_{1-x}\text{Ga}_x\text{As}_y\text{P}_{1-y}$  system is more significant due to the smaller spacing between valence subbands. At the higher carrier densities, this spacing leads to an even larger increase in the population of higher energy subbands, and thus more wasted carriers.

To study the major recombination mechanisms in each of these lasers, it is convenient to use the measured spontaneous power which has been monitored by an optical power meter. In this case, the data are easily measured over a large current range, and the photodetector performs the integration of the spontaneous emission power spectrum. Fig. 9 shows a log-log plot of the square root of spontaneous emission power versus the total injected current for each device studied. This format was chosen [28] to give an indication of the relative contributions of each recombination mechanism (monomolecular, radiative, and Auger). The value of the  $x$  axis can be expressed as

$$\sqrt{P} = K_2 \sqrt{B_{\text{eff}} N} \quad (39)$$

where  $K_2$  is another unknown coefficient which includes the fraction of spontaneous emission power captured by the optical fiber. We see that this is almost directly proportional to  $N$ , but not perfectly, due to the carrier dependence of  $B_{\text{eff}}$ , as discussed above. This deviation is relatively small, however, since we can see clear regions of slope one and slope three which correspond, respectively, to regimes where  $I$  is proportional to  $N$  (monomolecular mechanisms dominate) and  $N^3$  (where Auger mechanisms dominate). The region of slope two could indicate that the radiative processes are dominant, but this is not clear since there would be a point at which the slope is two due to the transition between the  $N$  and  $N^3$  regimes, even if radiative processes were missing. These issues will be clarified in the following analysis.

It is necessary to transform the measured data into a relationship between total current density and carrier density. Current density is easily obtained from the current as

$$J_{\text{tot}} = \frac{I}{wL} \quad (40)$$

where  $w$  is the stripe width and  $L$  is the cavity length. To obtain  $N$ , however, the unknown coefficient  $K_2$  must be

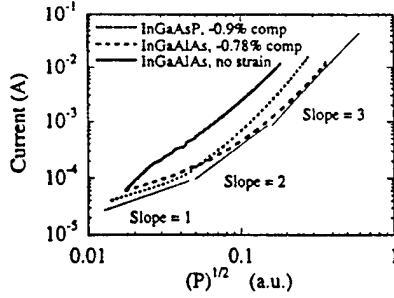


Fig. 9. The square root of the measured integrated spontaneous emission power  $\sqrt{P}$  (plotted along the x axis) versus the measured injection current along the vertical axis. The x axis is roughly proportional to carrier density, and the slope of the lines on the log-log plot give the power law for the injection current and carrier density relation.

determined. The fits of the net modal gain with our theory give a relation between  $I$  and  $N$  over a limited range of the measured data presently under consideration. Using the calculated dependence of  $B_{\text{eff}}$  on the carrier density for each system, and the measured  $\sqrt{P}$  value corresponding to the currents for the fitted gain data, (39) yields a value of  $K_2$  for each material system. The average between the values obtained for each of the  $I$ - $N$  pairs are used for our calculations and are listed in Table IV. All values are within 2% of the average value. Since  $K_2$  should be independent (for the most part) of injection current, it is fair to extrapolate the value of  $K_2$  from this small range of currents to the entire range of data under consideration. Using these  $K_2$  values and the calculated  $B_{\text{eff}}(N)$ , it is straightforward to obtain a value for  $N$  corresponding to the measured  $\sqrt{P}$  for each device.

The extracted relationships between  $J_{\text{tot}}$  and  $N$  are shown as dashed lines in Fig. 10(a) for the  $\text{In}_{1-x}\text{Ga}_x\text{As}_y\text{P}_{1-y}$  system and in Fig. 10(b) for the two  $\text{In}_{1-x-y}\text{Ga}_x\text{Al}_y\text{As}$  systems. The solid lines in these plots correspond to the best fit results using the relation

$$J_{\text{tot}} = \frac{eN_w L_w}{\eta_{\text{inj}}} [AN + B_{\text{eff}}(N)N^2 + CN^3] \quad (41)$$

where  $\eta_{\text{inj}}$  is the injection efficiency accounting for the fraction of carriers which make it into the QW's,  $N_w$  is the number of wells,  $A$  is the monomolecular recombination coefficient,  $B_{\text{eff}}(N)$  is the calculated radiative recombination coefficient, and  $C$  is the Auger recombination coefficient.  $A$  is a fitting parameter, but is only important for very low current densities. Its value is determined by fitting the behavior of the curve at these low current densities.  $\eta_{\text{inj}}$  and  $C$  are the major parameters which control the behavior of the curve. For a set value of  $\eta_{\text{inj}}$ , the penalty function for the fit is very sensitive to the  $C$  coefficient, so the value can be very well determined. However, a range of  $\eta_{\text{inj}}$  will give decent fits, so the extracted  $C$  value has some uncertainty. The best fit values of  $\eta_{\text{inj}}$ ,  $A$ , and  $C$  are presented in Table IV. The uncertainties on  $\eta_{\text{inj}}$  and  $C$  are determined by selecting those values which raise the penalty function 20% over the best fit value. The injection efficiency for the unstrained Sample C appears to have a relatively low injection efficiency.

It should be noted that previous measurements of the Auger coefficient in the  $\text{In}_{1-x}\text{Ga}_x\text{As}_y\text{P}_{1-y}$  material system have

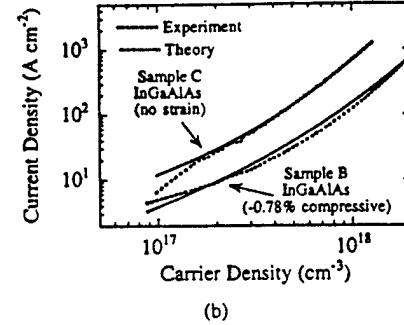
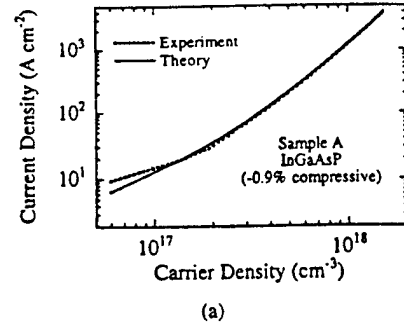


Fig. 10. The extracted current density/carrier density relation (dashed lines) as well as the best fits from the theory (solid lines) are shown for (a) the  $\text{In}_{1-x}\text{Ga}_x\text{As}_y\text{P}_{1-y}$  laser system (Sample A) and (b) the two  $\text{In}_{1-x-y}\text{Ga}_x\text{Al}_y\text{As}$  systems (Samples B and C).

given values between  $2 \times 10^{-29} \text{ cm}^6 \text{ s}^{-1}$  and  $1 \times 10^{-28} \text{ cm}^6 \text{ s}^{-1}$  [29]–[31]. As discussed previously, the fact that a significant amount of holes occupy states where they may only recombine by nonradiative processes could explain why the extracted Auger coefficient for our sample is significantly higher than this range. This indicates that the Auger coefficient can be minimized by selecting the strain and well width to increase the separation of the valence subbands. For the  $\text{In}_{1-x-y}\text{Ga}_x\text{Al}_y\text{As}$  material system, a reported value of the Auger coefficient [9] is  $3.6 \times 10^{-29} \text{ cm}^6 \text{ s}^{-1}$  which is smaller than our value for the compressive sample. Our procedure, based on a comprehensive gain model and a fitting of the gain spectra to determine  $N$  and  $B_{\text{eff}}$ , should provide a reliable estimate of the  $C$  coefficient.

These extracted values are used in Fig. 11 to compare the relative contributions of  $J_{\text{mono}}$ ,  $J_{\text{rad}}$ , and  $J_{\text{Aug}}$  for the compressive  $\text{In}_{1-x-y}\text{Ga}_x\text{Al}_y\text{As}$  and compressive  $\text{In}_{1-x}\text{Ga}_x\text{As}_y\text{P}_{1-y}$  systems. Each device is dominated by the Auger recombination well before the laser reaches threshold. However, due to an Auger coefficient about 10 times larger, the Auger recombination dominates at a much lower point and becomes much larger in the  $\text{In}_{1-x}\text{Ga}_x\text{As}_y\text{P}_{1-y}$  system. This leads to a much larger threshold current density. The  $T_0$  for each of these lasers, measured from the shift in threshold over a temperature range from  $15^\circ$  to  $60^\circ$ , is also presented in Table IV. These relative values agree with the trend in the extracted Auger coefficients, indicating that Auger recombination is a major factor reducing  $T_0$  for these laser systems [28], [32]. Finally, it is interesting to note that the radiative current density never becomes the dominant recombination mechanism. At the injection level where Auger recombination becomes significant, the radiative current density is about the same

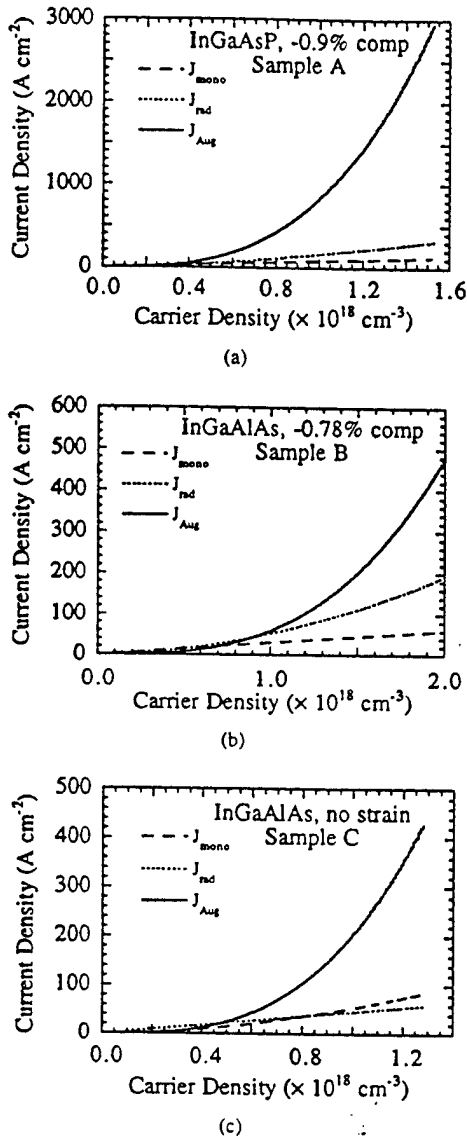


Fig. 11. The relative contributions of the monomolecular, radiative, and Auger recombination currents for (a)  $-0.9\%$  compressively strained  $\text{In}_{1-x}\text{Ga}_x\text{As}_y\text{P}_{1-y}$  (Sample A), (b)  $-0.78\%$  compressively strained  $\text{In}_{1-x-y}\text{Ga}_x\text{Al}_y\text{As}$  (Sample B), and (c) lattice-matched  $\text{In}_{1-x-y}\text{Ga}_x\text{Al}_y\text{As}$  (Sample C).

as the monomolecular current density for each system studied.

## V. CONCLUSION

In this paper, we have presented a comprehensive model for the calculation of the band edges of both  $\text{In}_{1-x}\text{Ga}_x\text{As}_y\text{P}_{1-y}$  and  $\text{In}_{1-x-y}\text{Ga}_x\text{Al}_y\text{As}$  QW lasers with an arbitrary composition. Using a many-body optical gain model, we have compared the net modal gain for both material systems with calculations from the realistic band structure. These comparisons allow us to obtain carrier densities for each of the measured currents. From a calibrated measurement of the spontaneous emission spectrum, we were able to obtain the radiative current density. These results are all in excellent agreement with our calculations. From a fit of the extracted relationship between carrier density and total current density, we were able to extract values for the Auger coefficient of

each material system studied. The relative values of these parameters correspond very well with the observed temperature performance of each device.

From this study, it is difficult to make a strong statement as to which of the two material systems is superior. Obviously, more studies on a variety of active region designs would be needed to gauge all of the relevant factors and draw such a conclusion. Our measurements seem to indicate that the  $\text{InGaAlAs}$  system is at least as good as and probably better than the  $\text{InGaAsP}$  systems in terms of Auger recombination and temperature stability. Also, care should be taken to design the QW's such that there is a large separation between the lowest and highest level subbands, in order to reduce the carriers wasted by nonradiative recombination and to reduce the temperature sensitivity of the lasers.

## ACKNOWLEDGMENT

The authors would like to thank Dr. T. Tanbun-Ek for providing devices for this study. They also wish to thank G. Liu and M. Silver for helpful discussions.

## REFERENCES

- [1] P. J. A. Thijs, L. F. Tiemijer, P. I. Kuindersma, J. J. M. Binsma, and T. van Dongen, "High performance of  $1.5\ \mu\text{m}$  wavelength  $\text{InGaAs-InGaAsP}$  strained quantum-well lasers and amplifiers," *IEEE J. Quantum Electron.*, vol. 27, pp. 1426-1438, 1991.
- [2] P. J. A. Thijs, L. F. Tiemijer, J. J. M. Binsma, and T. van Dongen, "Progress in long-wavelength strained-layer  $\text{InGaAs(P)}$  quantum-well semiconductor lasers and amplifiers," *IEEE J. Quantum Electron.*, vol. 30, pp. 477-499, 1994.
- [3] M. Allovon and M. Quillec, "Interest in  $\text{AlGaInAs}$  on  $\text{InP}$  for optoelectronic applications," *Proc. Inst. Elect. Eng.*, vol. 139, pp. 148-152, 1992.
- [4] C. E. Zah, R. Bhat, B. Pathak, F. Favire, W. Lin, M. C. Wang, N. C. Andreadakis, D. M. Hwang, M. A. Koza, T. P. Lee, Z. Wang, D. Darby, D. Flanders, and J. J. Ssieh, "High performance uncooled  $1.3\ \mu\text{m}$   $\text{AlGaInAs/InP}$  strained-layer quantum well lasers for subscriber loop applications," *IEEE J. Quantum Electron.*, vol. 30, pp. 511-523, 1994.
- [5] T. Tanbun-Ek, S. N. G. Chu, P. W. Wisk, R. Pawelek, J. Minch, E. Young, and S. L. Chuang, "High performance buried heterostructure  $1.55\ \mu\text{m}$  wavelength  $\text{AlGaInAs/InP}$  multiple quantum well lasers grown entirely by MOVPE technique," *IEEE Photon. Technol. Lett.*, submitted for publication. [Author: Please update the status of this paper.—Ed.]
- [6] T. Ishikawa and J. Bowers, "Band lineup and in-plane effective mass of  $\text{InGaAsP}$  or  $\text{InGaAlAs}$  on  $\text{InP}$  strained-layer quantum well," *IEEE J. Quantum Electron.*, vol. 30, pp. 562-569, 1994.
- [7] O. Issanchou, J. Barrou, E. Idiat-Alhor, and M. Quillec, "Theoretical comparison of  $\text{GaInAs/GaAlInAs}$  and  $\text{GaInAs/GaInAsP}$  quantum-well lasers," *J. Appl. Phys.*, vol. 78, pp. 3925-3930, 1995.
- [8] J. Pan and J.-I. Chyi, "Theoretical study of the temperature dependence of  $1.3\ \mu\text{m}$   $\text{AlGaInAs-InP}$  multiple-quantum-well lasers," *IEEE J. Quantum Electron.*, vol. 32, pp. 2133-2138, 1996.
- [9] M. C. Wang, K. Kash, C. Zah, R. Bhat, and S. L. Chuang, "Measurement of nonradiative Auger and radiative recombination rates in strained-layer quantum-well systems," *Appl. Phys. Lett.*, vol. 62, pp. 166-168, 1993.
- [10] S. L. Chuang, *Physics of Optoelectronic Devices*. New York: Wiley, 1995.
- [11] K. H. Hellwege, Ed., *Landolt-Bornstein Numerical Data and Functional Relationships in Science and Technology*. Berlin, Germany: Springer, 1982, new series, group III, 17a; groups III-V 22a, Berlin: Springer, 1986.
- [12] C. G. Van der Walle, "Band lineups and deformation potentials in the model-solid theory," *Phys. Rev. B*, vol. 39, pp. 1871-1883, 1989.
- [13] W. A. Harrison, "Elementary theory of heterojunctions," *J. Vac. Sci. Technol.*, vol. 14, pp. 1016-1021, 1977.
- [14] J. Bohrer, A. Krost, and D. Bimberg, "Composition dependence of band gap and type of lineup in  $\text{InGaAlAs/InP}$  heterostructures," *Appl. Phys. Lett.*, vol. 63, pp. 1918-1920, 1993.

- [15] S. Adachi, *Physical Properties of III-V Semiconductor Compounds*. New York: Wiley, 1992.
- [16] D. Ahn, "Theory of non-Markovian optical gain in quantum well lasers," *Prog. Quantum Electron.*, vol. 21, pp. 249-287, 1997.
- [17] C. S. Chang and S. L. Chuang, "Modeling of strained quantum-well lasers with spin-orbit coupling," *IEEE J. Select. Topics Quantum Electron.*, vol. 1, pp. 218-229, 1995.
- [18] G. Lasher and F. Stern, "Spontaneous and stimulated recombination radiation in semiconductor," *Phys. Rev. A*, vol. 133, pp. 553-565, 1964.
- [19] C. S. Chang, S. L. Chuang, J. Minch, W. Fang, Y. K. Chen, and T. Tanbun-Ek, "Amplified spontaneous emission spectroscopy in strained quantum-well lasers," *IEEE J. Select. Topics Quantum Electron.*, vol. 1, pp. 1100-1107, 1995.
- [20] H. Haug and S. W. Koch, *Quantum Theory of the Optical and Electronic Properties of Semiconductors*. Singapore: World Scientific, 1993.
- [21] W. W. Chow, S. W. Koch, and M. Sargent III, *Semiconductor-Laser Physics*. Berlin, Germany: Springer, 1994, ch. 5.
- [22] B. W. Hakki and T. L. Paoli, "Gain spectra in GaAs double heterostructure injection lasers," *J. Appl. Phys.*, vol. 46, pp. 1299-1306, 1975.
- [23] D. T. Cassidy, "Technique for measurement of the gain spectra of semiconductor diode lasers," *J. Appl. Phys.*, vol. 56, pp. 3096-3099, 1984.
- [24] W. Fang, M. Hattendorf, S. L. Chuang, J. Minch, C. S. Chang, C. G. Bethea, and Y. K. Chen, "Analysis of temperature sensitivity in semiconductor lasers using gain and spontaneous emission measurements," *Appl. Phys. Lett.*, vol. 70, pp. 796-798, 1997.
- [25] G. E. Shtengel, P. A. Morton, R. F. Kazarinov, D. A. Ackerman, M. S. Hybertsen, G. L. Belenky, and C. L. Reynolds, Jr., "Experimental study of physical parameters of semiconductor lasers," *Proc. SPIE*, vol. 2994, pp. 678-689, 1997.
- [26] J. P. Loehr and J. Singh, "Theoretical studies of the effect of strain on the performance of strained quantum-well lasers based on GaAs and InP technology," *IEEE J. Quantum Electron.*, vol. 27, pp. 708-716, 1991.
- [27] E. Yablonovitch and E. O. Kane, "Band structure engineering of semiconductor lasers for optical communications," *J. Lightwave Technol.*, vol. 6, pp. 1292-1299, 1988.
- [28] S. J. Sweeney, A. F. Phillips, A. R. Adams, E. P. O'Reilly, and P. J. A. Thijs, "The effect of temperature dependent processes on the performance of 1.5  $\mu\text{m}$  compressively strained InGaAs(P) MQW semiconductor diode lasers," *IEEE Photon. Technol. Lett.*, vol. 10, pp. 1076-1078, 1998.
- [29] R. Olshansky, C. B. Su, J. Manning, and W. Powazinik, "Temperature sensitivity and high temperature operation of long wavelength semiconductor lasers," *IEEE J. Quantum Electron.*, vol. QE-20, pp. 838-854, 1984.
- [30] Y. Zou, J. S. Osinski, P. Grodzinski, P. D. Dapkus, W. Rideout, W. F. Sharfin, J. Schlafer, and F. D. Crawford, "Experimental study of Auger recombination, gain, and temperature sensitivity of 1.5  $\mu\text{m}$  compressively strained semiconductor lasers," *IEEE J. Quantum Electron.*, vol. 29, pp. 1565-1575, 1993.
- [31] G. Agrawal and N. K. Dutta, *Semiconductor Lasers*, 2nd ed. New York: Van Nostrand Reinhold, 1993.
- [32] E. P. O'Reilly and M. Silver, "Temperature sensitivity and high temperature operation of long wavelength semiconductor lasers," *Appl. Phys. Lett.*, vol. 63, pp. 3318-3320, 1993.

J. Minch, photograph and biography not available at the time of publication.

S. H. Park, photograph and biography not available at the time of publication.

T. Keating, photograph and biography not available at the time of publication.

S. L. Chuang, photograph and biography not available at the time of publication.

# A Wavelength-Tunable Curved Waveguide DFB Laser with Integrated Modulator

A. Hsu, S. L. Chuang,  
W. Fang, L. Adams, G. Nykolak, and T. Tanbun-Ek

**Abstract**— A distributed-feedback (DFB) laser with a curved waveguide in the active region integrated with an electroabsorption modulator is studied experimentally and theoretically. The modulator controls the lasing wavelength of the DFB laser by acting as an optical phase shifter. Our model, which is based on the transfer-matrix method, is used to simulate this multi-section device with the curved waveguide, self-consistently including the effects of spatial hole-burning (SHB). The model explains the features and wavelength-tuning behavior of the spectrum and shows good agreement with experimentally measured spectra. We also show theoretically that the curved waveguide suppresses the longitudinal photon density profile of the device compared with a straight waveguide case, which implies reduced SHB effects.

**Keywords**— Distributed-feedback, modulator, curved waveguide, wavelength-tunable, spatial hole-burning

## I. INTRODUCTION

THE study of wavelength-tunable laser sources is an important topic of research, emphasized by the rapidly expanding development of wavelength-division multiplexed (WDM) optical communications systems, which can presently transmit data at rates of over 1 Tb/sec over a single optical fiber.

Research in multi-section wavelength-tunable lasers has been investigated extensively for use in WDM and coherent optical communications systems and some of the progress in this field is well summarized in Ref. [1], [2]. Originally, the goal of developing distributed-feedback (DFB) lasers integrated with electroabsorption modulators was to improve high-speed performance by reducing frequency chirping of DFB lasers by external modulation [3]–[9]. Recently, these devices have also been used as wavelength-tunable sources [10], [11]. The use of a chirped grating pitch [12]–[14] has been investigated as a way to achieve a distributed phase shift in the grating. Several groups have implemented this chirped grating pitch using a bent or curved waveguide to achieve wavelength tuning or high power operation and have shown promising results [15]–[17]. In previous work, we have modeled a DFB laser and an integrated electroabsorption modulator-laser (EML) using the

transfer-matrix method [18], [19]. Multisection DFB lasers have been modeled using a transmission-line model as well [20].

The wavelength-tunable laser studied here, a possible candidate for WDM systems, consists of a distributed-feedback (DFB) laser with curved waveguide, integrated with an electroabsorption modulator which acts as a wavelength-tuning section. The structure for this device is identical to that of an integrated electroabsorption modulator and laser (EML) with the exception that the facet coatings on the laser and modulator are opposite to those of the conventional EML. A voltage bias applied to the modulator effectively controls the lasing wavelength of the DFB laser. Previously reported results for this device have shown a wavelength tuning range of 3.5 nm and high-speed optical packet switching over four wavelength channels at a rate of 2.5 Gb/s [11].

The purpose of this work is to model this wavelength-tunable multi-section device, including spatial hole burning (SHB) effects self-consistently, and to explain the characteristics of the spectrum and the wavelength-tuning behavior of this device by showing good agreement between theory and experiment. We first describe the device structure in Section II. In Section III, we explain our model based on the transfer-matrix method that includes spatial hole-burning (SHB) effects. In Section IV, we compare measured spectrum with theory and explain the spectral features of this wavelength-tunable laser. This includes explanations for the wavelength-tuning behavior of this device as a function of modulator voltage and theoretical results which show SHB suppression due to the use of a curved waveguide. In Section V, we summarize our work and present our conclusions.

## II. DEVICE STRUCTURE

A schematic of the wavelength-tunable laser, which consists of a DFB laser with curved waveguide integrated with an electroabsorption modulator separated by an isolation region, is shown in Fig. 1. The length of the DFB section is 300  $\mu\text{m}$  long, the isolation region is about 80  $\mu\text{m}$ , and the modulator is 250  $\mu\text{m}$ . The facet reflectivity at the HR coated facet on the modulator side is 99%, and the AR coated facet reflectivity on the DFB laser side is estimated to be 1% using a 50  $\mu\text{m}$  window structure on the AR side of the DFB section. The shape of this curved waveguide has been modeled previously as a raised sine shape [11]. However, this waveguide can also be modelled as an S-bend shape which has more flexible parameters and provides a

A. Hsu, S. L. Chuang, are with the Department of Electrical and Computer Engineering, University of Illinois at Urbana-Champaign, 1406 West Green Street, Urbana, Illinois 61801. E-mail: ahsu@uiuc.edu.

W. Fang was with the department of ECE, University of Illinois at Urbana-Champaign and is currently with Bell Laboratories, Lucent Technologies, 101 Crawford's Corner Road, Holmdel, New Jersey 07733. L. Adams and G. Nykolak are with Bell Laboratories, Lucent Technologies, 700 Mountain Avenue, Murray Hill, New Jersey 07974. T. Tanbun-Ek was with Bell Laboratories, Lucent Technologies and is now with Multiplex, New Jersey.

more general waveguide shape. The shape of the S-bend curved waveguide is given by the following equations [16]:

$$\begin{aligned} y(z) &= 2W \quad \text{for } 0 \leq z \leq L_1 \\ y(z) &= 2W + \frac{W}{L_B} (L_1 - z) + \frac{W}{\pi} \sin\left(\pi \frac{z - L_1}{L_B}\right) \\ &\quad \text{for } L_1 \leq z \leq L_1 + 2L_B \\ y(z) &= 0 \quad \text{for } L_1 + 2L_B \leq z \leq L \end{aligned} \quad (1)$$

where  $L$  is the total length,  $L_1$  is the length of the straight section before the S-bend,  $L_B$  is equal to half of the length of the S-bend region, and  $W$  is the width of half of the S-bend. For this device, we estimated the S-bend parameters to be  $L = 360 \mu\text{m}$ ,  $L_1 = 47 \mu\text{m}$ ,  $L_B = 133 \mu\text{m}$ , and  $W = 10 \mu\text{m}$ .

In both devices, the active region in the DFB and the modulator sections consist of 7 layers of compressively strained InGaAsP quantum wells and were fabricated using a selective area MOVPE technique. The DFB region has an estimated compressive strain of at least  $-1\%$  while the compressive strain in the modulator was measured to be about  $0.5\%$ . The peak wavelength of the photoluminescence was measured at  $1.4891 \mu\text{m}$ . The isolation region between the DFB and modulator sections was created by shallow trenching a depth of about  $0.7 \mu\text{m}$  to yield an electrical isolation with a typical value greater than  $50 \text{ k}\Omega$ .

### III. THEORY

#### A. Longitudinal Fields in a Multi-section Device

We model the longitudinal properties of the optical fields in the curved waveguide DFB laser with integrated modulator and isolation sections using the transfer-matrix method. Most of the development of the transfer-matrix method used in our model can be found in Ref. [18], [19].

The laser, isolation, and modulator sections can each be represented by the transfer matrices  $\overline{\overline{F}}^{DFB}$ ,  $\overline{\overline{F}}^{isol}$ , and  $\overline{\overline{F}}^{mod}$ , respectively, which gives the slowly varying amplitudes of the forward and backward propagating waves,  $A(z)$  and  $B(z)$ , respectively, in each section. The elements of these matrices are given by [18], [19]

$$F_{11}(l) = \frac{1}{1 - r_p r_m} (e^{iq_l} - r_p r_m e^{-iq_l}) \quad (2)$$

$$F_{12}(l) = \frac{-r_m}{1 - r_p r_m} (e^{iq_l} - e^{-iq_l}) \quad (3)$$

$$F_{21}(l) = \frac{r_p}{1 - r_p r_m} (e^{iq_l} - e^{-iq_l}) \quad (4)$$

$$F_{22}(l) = \frac{1}{1 - r_p r_m} (-r_p r_m e^{iq_l} + e^{-iq_l}), \quad (5)$$

where

$$q = \sqrt{\Delta\beta^2 + \kappa_{ab}\kappa_{ba}} \quad (6)$$

and

$$r_p = \frac{\kappa_{ba}}{\Delta\beta + q} \quad (7)$$

$$r_m = \frac{-\kappa_{ab}}{\Delta\beta + q} \quad (8)$$

where  $\beta = 2\pi n_e(\lambda)/\lambda$  is the propagation constant where  $n_e$  is the effective index of the fundamental guided mode,  $\beta_0 = \pi/\Lambda$  where  $\Lambda$  is the grating pitch, and the detuning parameter  $\Delta\beta = \beta - \beta_0$ .

The interface between sections which includes differences in refractive index between each section is also represented by a transfer matrix  $\overline{\overline{T}}^{int}$  and is derived from the boundary conditions that tangential electrical and magnetic fields are continuous at the interface at a given  $z = l_1$  or  $l_2$ , given by

$$\begin{bmatrix} A(l^+) \\ B(l^+) \end{bmatrix} = \overline{\overline{T}}^{int}(l) \begin{bmatrix} A(l^-) \\ B(l^-) \end{bmatrix}. \quad (9)$$

The forward and backward propagating waves in the whole device can be modeled by multiplying the matrices for each section and interface together as given by

$$\begin{bmatrix} A(L_{total}) \\ B(L_{total}) \end{bmatrix} = \left[ \overline{\overline{F}}^{mod}(L_{mod}) \right] \left[ \overline{\overline{T}}^{int}(l_2) \right] \left[ \overline{\overline{F}}^{isol}(L_{iso}) \right] \left[ \overline{\overline{T}}^{int}(l_1) \right] \left[ \overline{\overline{F}}^{DFB}(L_{DFB}) \right] \begin{bmatrix} A(0) \\ B(0) \end{bmatrix} \quad (10)$$

where  $L_{total}$  is the length of the entire device,  $L_{DFB}$ ,  $L_{iso}$ , and  $L_{mod}$  are the lengths of the DFB laser, isolation, and modulator sections, respectively, and  $l_i$  is the location of section  $i$ , where  $l_1 = L_{DFB}$ ,  $l_2 = L_{DFB} + L_{iso}$ , as shown in Fig. 1.

We model the amplified spontaneous emission spectrum for the integrated device by including an equivalent spontaneous emission source [21] into the transfer matrix method. We place an equivalent spontaneous-emission surface current density  $J_s$  at a position  $z_s$  in the (active) DFB section of the cavity and solve the boundary conditions for the electric and magnetic fields on either side of the current sheet. From this, we obtain the relation between the field amplitudes near the source position:

$$\begin{bmatrix} A^+(z_s) \\ B^+(z_s) \end{bmatrix} - \begin{bmatrix} A^-(z_s) \\ B^-(z_s) \end{bmatrix} = \overline{\overline{M}}^{-1} \begin{bmatrix} 0 \\ \omega\mu J_s \end{bmatrix} = \begin{bmatrix} s_{21} \\ s_{22} \end{bmatrix}, \quad (11)$$

where

$$\overline{\overline{M}} = \begin{bmatrix} e^{i\beta_0 z_s} & e^{-i\beta_0 z_s} \\ \beta e^{i\beta_0 z_s} + \kappa_{ba} e^{-i\beta_0 z_s} & \kappa_{ab} e^{i\beta_0 z_s} - \beta e^{-i\beta_0 z_s} \end{bmatrix}. \quad (12)$$

where  $\kappa_{ab}$  and  $\kappa_{ba}$  are the coupling coefficients used in the coupled-mode equations [19]. Next, we match boundary conditions at the facets and obtain

$$\begin{bmatrix} A(L_{total}) \\ B(0) \end{bmatrix} = \overline{\overline{D}}^{-1} \overline{\overline{F}}(L_{total} - z_s) \begin{bmatrix} s_{21} \\ s_{22} \end{bmatrix}. \quad (13)$$

where the matrix  $D$  contains the boundary condition information at the facets

$$\overline{\overline{D}} = \begin{bmatrix} 1 & -r_1 F_{11}(L_{total}) - F_{12}(L_{total}) \\ r_2 & -r_1 F_{21}(L_{total}) - F_{22}(L_{total}) \end{bmatrix}, \quad (14)$$

and  $r_1$  and  $r_2$  are the complex reflectivities at the facets. The matrix  $\bar{F}(L_{total})$  is the product of all the transfer matrices in (10), and it describes the total three-section device whereas the matrix  $\bar{F}(L_{total} - z_s)$  contains only those matrices between  $z_s$  and  $L_{total}$ .

The amplified spontaneous emission intensity from each facet is obtained by summing the square of the electric field envelopes  $B(0)$  and  $A(L)$  due to a single source at  $z_s$  over all the sources  $J_s$  within the cavity ( $0 \leq z_s \leq L$ ) as given by

$$I_{left} = (1 - |r_1|^2) \int_0^L |B(0)|^2 dz_s, \quad (15)$$

$$I_{right} = (1 - |r_2|^2) \int_0^L |A(L)|^2 dz_s. \quad (16)$$

The ASE is calculated using (15) and (16) for each wavelength to get the entire ASE spectrum.

The photon density profile is obtained from the electric field envelopes using

$$S(z) \propto |A(z)|^2 + |B(z)|^2, \quad (17)$$

Again, the total photon density is found by summing the photon density  $S(z)$  due to a single source at  $z_s$  over all the sources  $J_s$  within the cavity.

### B. Spatial Hole Burning

In the first iteration of the photon density calculation, the gain and carrier density profiles along the device are considered uniform. If the applied injection current is above threshold, the calculated photon density profile will be perturbed as a function of longitudinal cavity position and therefore not constant. The carrier density and gain are recalculated using the carrier density rate equation at steady state given by

$$\frac{dN}{dt} = \frac{I}{eV} - AN - BN^2 - CN^3 - v_g g(N) S \quad (18)$$

where  $I$  is the injected current,  $e$  is the electron unit charge,  $V$  is the volume of the laser active region,  $A$  is the mono-carrier lifetime coefficient,  $B$  is the bimolecular carrier recombination coefficient,  $C$  is the Auger carrier recombination coefficient,  $v_g$  is the group velocity,  $g(N)$  is the material gain as a function of carrier density  $N$ , and  $S$  is the photon density. In the model, we consider a linearized material gain given by  $g(N) = g'(N - N_0)$ , where  $g'$  is the differential gain and  $N_0$  is the carrier density at transparency. This results in a nonuniform carrier density and profile. The refractive index profile also becomes nonuniform due to the perturbed carrier density profile through the relation:

$$\Delta n_e = -\frac{\lambda \alpha_e g'}{4\pi} \Delta N. \quad (19)$$

where  $\Delta n_e$  is the change in effective index,  $\lambda$  is wavelength,  $\alpha_e$  is the linewidth enhancement factor, and  $g'$  is differential gain. This change in refractive index to a nonuniform carrier density profile changes the threshold gain of

potential lasing modes and accounts for the decrease in side mode suppression ratio and mode-hopping associated with spatial hole burning. The photon density and carrier density are continually recalculated using (18) until a self-consistent solution is found. Only a single longitudinal mode is taken into account. Our model has been applied to the study of spatial hole burning in conventional DFB lasers with excellent agreement with experimental data [19]. It should be noted that each section of the device is further subdivided into multiple sections, and the coupled-mode equations are used to derive the transfer matrices to account for the spatially-dependent refractive index and gain profiles and the grating pitch parameter.

### C. Curved Waveguide and Dispersion

The curved waveguide in the DFB laser section induces an effective variation in grating pitch  $\Lambda_{eff}$  as a function of longitudinal position and is included by [11]:

$$\Lambda_{eff} = \frac{\Lambda_0}{\cos \phi(z)} \quad (20)$$

$$\phi(z) = \tan^{-1} \frac{y(z)}{z} \quad (21)$$

where  $y$  and  $z$  are defined in (1), and  $\Lambda_0$  is the grating pitch for the straight waveguide case.  $\Lambda_{eff}$  is taken into account in the model through the propagation constant  $\beta_o = \pi/\Lambda_{eff}$ , whereas in our previous work [19],  $\beta_o = \pi/\Lambda_0$ . In addition, the use of a curved waveguide slightly increases the effective length of the waveguide in the DFB laser section through which the fields propagate. This is taken into account in the model.

The effects of dispersion are also considered in the model. Over a narrow range of  $\lambda$  near a reference wavelength  $\lambda_0$ , the effective index  $n_e(\lambda)$  can be approximated by a linear function of  $\lambda$ :

$$n_e(\lambda) = n_e(\lambda_0) - s(\lambda - \lambda_0) \quad (22)$$

where the slope  $s$  is

$$s = \frac{(n_g - n_e(\lambda_0))}{\lambda_0} \quad (23)$$

and  $n_g$  is the group index, which can be approximated as a constant within the wavelength range of interest. We estimate the group refractive index from the mode spacing outside the stop band in the experimental spectrum, and the value of  $s$  is estimated using previous experimental results [21] for the InGaAsP system. We then calculate  $n_e(\lambda_0)$  and solve for  $n_e(\lambda)$  using (22) over the wavelengths of interest.

### D. Voltage-dependent Refractive Index and Gain in the Electroabsorption Modulator

Typically in EMLs, the bandgap of the modulator is slightly larger than that in the DFB laser section with a detuning of about 30-60 nm [8], [9] so that for zero or forward modulator voltage bias, there is no attenuation except for insertion loss. For a positive voltage bias, carriers

are injected so light propagating through the modulator experiences gain, and the refractive index of the modulator decreases. If a negative voltage bias is applied to the modulator, absorption is increased due to quantum-confined Stark effects or Franz-Keldysh effects which in turn increases the refractive index of the modulator. We model the voltage-dependent absorption and refractive index in the modulator through a simple linear additive term as given by

$$g_{mod} \simeq g_0 + \frac{dg}{dV_{mod}} V_{mod} \quad (24)$$

$$n_{mod} \simeq n_0 - \frac{dn}{dV_{mod}} V_{mod} \quad (25)$$

where  $g_{mod}$  and  $n_{mod}$  are the absorption coefficient (1/cm) and effective index in the modulator, respectively,  $g_0$  and  $n_0$  are the gain and effective index in the modulator with no voltage bias,  $dg/dV_{mod}$  and  $dn/dV_{mod}$  are empirical constants, and  $V_{mod}$  is the voltage bias at the modulator. Note that both  $dg/dV_{mod}$  and  $dn/dV_{mod}$  are positive. Because the change in refractive index in the forward bias case is caused by carrier injection while the change in refractive index in the reverse bias case is caused by the electroabsorption effect, the value of  $dn/dV_{mod}$  is different for each case. In both cases, the change in refractive index in the modulator due to the voltage bias is the mechanism responsible for the phase-shifting effect as will be explained in Section IV.

#### E. Leakage Current from the Modulator

The function of the fabricated isolation region is to provide electrical isolation between the modulator and laser sections so that the biasing of one section does not affect the performance of the other. However, the isolation region in this particular device does not provide perfect electrical isolation. When the modulator is forward-biased, carriers are injected into the modulator and a small leakage current flows from the modulator into the laser section. This leakage current will decrease the refractive index of the laser section and is included in the model using a simple empirical relation,

$$n_{DFB} = n_0 - \frac{dn_{leak}}{dV_{mod}} V_{mod} \quad (26)$$

where  $n_{DFB}$  is the modified effective index of the laser section,  $n_0$  is the original effective index and  $dn_{leak}/dV_{mod}$  is the change in effective index due to the leakage current and is determined empirically by the observed shift in lasing wavelength in the measured spectrum as a function of  $V_{mod}$ .

### IV. RESULTS AND DISCUSSIONS

#### A. Wavelength-Tuning Mechanisms: Phase-Shifting and Current Tuning

Although our transfer-matrix method provides the full numerical solution taking into account all multiple reflection, we present a simple physical model to illustrate the

physics of the tuning mechanisms below. Since the isolation region and modulator are homogeneous, meaning that there is no distributed feedback present, the round trip through these sections can also be perceived as an effective reflectivity at the DFB-isolation region interface. Varying the modulator voltage will change the magnitude and phase of the reflectivity at this interface, hence, the modulator acts as a phase-shifting section. The voltage-dependent magnitude and phase of the interface reflectivity is approximately

$$r_{int} = r_{HR} e^{i2\beta_{iso}L_{iso}} e^{i2\beta_{mod}L_{mod}} \quad (27)$$

where  $r_{int}$  and  $r_{HR}$  are the magnitudes of the field reflectivity at the laser-isolation region and HR facet, respectively,  $L_{iso}$  and  $L_{mod}$  are the lengths of the isolation region and modulator, respectively,  $\beta_{iso}$  is the propagation constant of the isolation region, and  $\beta_{mod}$  is the voltage-dependent propagation constant of the modulator given by

$$\beta_{mod} = \frac{2\pi}{\lambda} n_{mod} - i \frac{g_{mod}}{2} \quad (28)$$

where  $g_{mod}$  and  $n_{mod}$  are functions of modulator voltage and given by (24) and (25) respectively. Therefore, the change in phase at the interface due to a voltage-dependent change in refractive index is given by

$$\Delta\phi = \frac{4\pi\Delta n_e L_{mod}}{\lambda} \quad (29)$$

where  $\Delta n_e$  is given by the voltage-dependent term in (25).

It is well known that in an HR/AR coated DFB laser, the lasing wavelength can change dramatically for different phases at the HR facet [22]. By integrating a phase-tuning section into the HR-coated side of the DFB laser, we use this idea to achieve voltage-controlled wavelength tuning over the stopband of the DFB laser.

The other mechanism behind wavelength tuning in this integrated device is due to leakage current from the modulator. An increasing positive modulator voltage will inject carriers into the laser section, decrease the refractive index of the laser, and shift the spectrum toward longer wavelengths. For larger negative voltage biases, carriers are absorbed from the laser and the spectrum shifts toward shorter wavelengths. Although leakage current is not usually viewed favorably, this effect, when combined with the phase-shifting effect, actually allows this device to achieve a larger wavelength-tuning range than phase-shifting alone.

The wavelength-tuning behavior of this device naturally leads to a discussion on the advantages and disadvantages of current tuning and phase-shifting as wavelength-tuning mechanisms in lasers. The idea of using different injection currents and operating temperatures to produce a change in the wavelength of the lasing mode has long been known and has been extended to a variety of other types of devices including multi-section lasers. The advantage of current tuning is that one can achieve a continuous tuning range. The main disadvantage is that for wavelength switching, as used in traffic routing applications, current tuning is a relatively slow process, limited by the carrier lifetime,

and cannot support wavelength switching at rates in the multi-GHz range. In order to increase wavelength switching rates, several groups have taken advantage of the faster Franz-Keldysh effects in a reverse-biased electroabsorption modulator to produce wavelength switching. Nakajima et al. demonstrated wavelength switching at 10 Gb/s over a 0.2 nm range [10]. This wavelength tuning was achieved by absorption of carriers by the modulator and is essentially current tuning using a faster process.

Using the same type of device presented here, it has been shown that wavelength switching at 2.5 Gb/s between 4 wavelength channels spanning a 2.1 nm range can be achieved [11]. The wider wavelength range achieved here is due the fact that both phase-shifting and current tuning from quantum-confined Stark effects were used to produce the wavelength tuning.

### B. Spectrum of the Integrated DFB Laser-Modulator

Our model was first used to explain some of the features present in the output spectrum of this curved waveguide DFB laser with integrated modulator. The spectrum of a conventional HR/AR coated DFB laser was measured above threshold as shown in Fig. 2(a). The DFB laser spectrum typically has a lasing mode with a side mode suppression ratio (SMSR) greater than 30dB on one side of the stopband and side modes with amplitudes which decrease gradually for shorter and longer wavelengths away from the stopband. The measured spectrum of the integrated device with no modulator voltage bias is shown in Fig. 2(b) and shows several interesting features which differ from the conventional DFB laser. The first feature is the absence of a visible stopband. The second feature is that the modes alternate in amplitude, whereas the mode amplitudes of the conventional DFB laser gradually decrease away from the stopband. The third feature is that competing side modes can be seen on both sides of the lasing mode, whereas in the conventional DFB laser, there is usually only one competing mode located on the other side of the stopband. The theoretically calculated spectrum shown in Fig. 2(c) exhibits features which are very similar to the measured spectrum shown in Fig. 2(b). The parameters used in simulations of the integrated wavelength-tunable device are shown in Table I.

The spectrum of the integrated device can be explained by looking at the threshold gain of the modes as a function of wavelength for several cases. First we consider the effect of using a two-section DFB laser-modulator device compared to the single-section DFB laser case. Shown in Fig. 3(a) are the modes for a single-section DFB laser with straight waveguide case. Shown in Fig. 3(b) are the modes for the two-section integrated laser-modulator. For the single-section DFB laser, the modes show a well-defined stopband. However, for the two-section DFB laser-modulator device, the modes seem to separate into two sets near the stopband, where the set of modes with higher threshold gain correspond to the coupled-cavity effects from the modulator region, and the modes with lower threshold gain correspond to the DFB laser region. This

accounts for the alternating mode amplitude behavior away from the stopband toward shorter and longer wavelengths as seen in the spectrum.

In a straight waveguide, the grating pitch is constant as a function of longitudinal cavity position which produces two well-defined Bragg frequency modes located oppositely across the stopband. In the curved waveguide, the grating pitch is chirped as a function of cavity position which produces a mode-flattening effect around the stopband which increases as a function of S-bend width  $W$ . This effect is illustrated by simulating a single-section AR/AR coated DFB laser in order to isolate the effects of using the curved waveguide and more clearly illustrate the effect. Figs. 4(a)-(c) where the threshold gain of the theoretically calculated modes are plotted versus wavelength for increasing values of  $W$ . The mode-flattening effect comes from the fact that using a curved waveguide or chirped grating pitch, the Bragg wavelength is no longer defined as a single frequency but a range of frequencies. Therefore, the distributed-feedback is weaker for one particular frequency, and the SMSR as determined by the threshold gain decreases as a result. This mode-flattening effect around the stopband accounts for the presence of multiple competing side modes in the spectrum of the integrated device as well as the absence of a stopband. Although a reduced SMSR is not desirable, this mode-flattening effect may extend the wavelength-tuning range of this type of device by providing more competing modes for lasing, which may be selected by the modulator section. Far outside the stopband, the mode behavior was observed to be determined by the Fabry-Perot cavity in both experiment and theory as expected. Simulations of the modes for an HR/AR coated DFB laser shows a similar mode-flattening effect due to the curved waveguide.

### C. Wavelength Tuning of the Lasing Mode

The model was used to simulate the wavelength-tuning behavior in the integrated DFB laser-modulator for several values of modulator voltage. Fig. 5(a) shows the measured spectrum of the integrated device for modulator voltage values of 0, +0.47, +0.78, +0.87, +0.92, and +1.03 V. As explained earlier, the wavelength tuning occurs due to a combination of phase-shifting and current tuning. In general, the wavelength tuning behavior of this device can be described in the following way. As the modulator voltage is increased from 0 V, the lasing mode remains at one wavelength until +0.47 V, where the lasing mode switches abruptly to a second wavelength. As the modulator is increased further, the lasing mode remains at this second wavelength until +0.78 V, where the lasing mode switches to another wavelength, and this behavior continues until +1.03 V. Fig. 5(b) shows the theoretically calculated spectrum for modulator values of 0, +0.65, +0.75, +0.85, +0.95, and +1.10 V, which shows reasonably good agreement using the linear model for voltage-dependent refractive index.

For a positive voltage bias, the modulator gain and refractive index could be modeled more accurately by making them functions of carrier density in the modulator which

is a function of injected current in the modulator. Also, wavelength-tuning of the lasing mode for positive bias voltages is also associated with changes in threshold current, linewidth, and output power. This was not included here, but we refer to Ref. [24] for a more detailed treatment.

Wavelength-tuning of the lasing mode was also observed for negative modulator bias voltages, although for a more limited range for this particular device. While in the positive voltage bias case, the refractive index decreases due to the injection of carriers, for this case, the refractive index increases due to absorption of carriers from quantum-confined Stark effects. Fig. 6(a) shows the measured spectrum for modulator voltage values of 0, -0.45, and -0.78 V. Fig. 6(b) shows the theoretically calculated spectrum for modulator values of 0, -0.50, and -0.90 V, which shows good agreement with the measured spectrum. The lasing wavelength as a function of positive and negative modulator voltages is shown for both the experimentally measured and theoretically calculated spectrum in Fig. 7. The closed circles are measured data points. The lasing wavelengths between data points, shown by the lines, were observed but not measured and are accurate to within  $\pm 1$  angstrom. The open triangles are the theoretically calculated values and show reasonably good agreement with the measured spectrum values.

#### D. Reduced Spatial Hole Burning due to the Curved Waveguide

Spatial hole burning (SHB) is an important phenomena which has been studied extensively [25]-[32], particularly in DFB lasers, because it can severely limit the maximum output power and cause mode-hopping or multimode behavior. SHB is caused by a nonuniform distribution of the photon density along the longitudinal cavity which can be caused by the distributed feedback in DFB lasers as well as asymmetries in HR/AR coated DFB lasers. A greater photon density in one region of a DFB laser will cause greater carrier depletion in that region so the carrier density profile also becomes nonuniform along the cavity. This in turn produces a nonuniform refractive index profile which affects the threshold gain conditions of the modes and can result in mode-hopping or multimode lasing at moderate injection currents above threshold. The model was used to calculate the longitudinal photon density profile for the straight and curved waveguide cases as shown in Fig. 8. The corresponding facet coatings and device sections are labelled with cavity position. The solid lines are for  $V_{mod}=0$ , and dashed lines are for  $V_{mod}=+0.65$  V. Considering only the laser section, the photon density profile shows a larger perturbation in the straight waveguide case than the curved waveguide case. One way to evaluate the amount of spatial hole burning present in a DFB laser is to calculate a flatness parameter [33]. We use a modified flatness parameter given by

$$F = \frac{1}{L} \int (I(z)_{norm} - I_{avg})^2 dz \quad (30)$$

where  $L$  is the length of the DFB laser section,  $I(z)_{norm}$  is the normalized local field intensity, and  $I_{avg}$  is the average normalized intensity. The integration is performed only over the DFB laser cavity length. Note that a greater  $F$  value indicates larger SHB effects. For the  $V_{mod} = 0$  V case, the calculated value of  $F$  was 0.78 for the straight waveguide and 0.21 for the curved waveguide. Very similar results were obtained for the other values of  $V_{mod}$ . These results suggest that the curved waveguide exhibits less SHB than the straight waveguide case. This is significant because a device with less SHB can remain at stable operation at higher output powers.

The photon density profile of the curved waveguide as shown in Fig. 8 exhibits an oscillatory behavior [34], [35]. This can be explained by the fact that this curved waveguide produces multiple distributed phase shifts due to the chirped pitch grating. Other groups have modeled multiple phase-shift devices which show multiple peaks in the photon density profile [36] and also distributed phase-shift devices which exhibit a rounding and flattening of a photon density profile peak when compared to an abrupt phase shift [16].

Several designs can be implemented to improve the performance of this device.

1) The present device mode-shifts between only two modes. By optimizing the curved waveguide shape and increasing the mode-flattening effect, we should be able to obtain mode-shifting between three or more modes, thereby increasing the wavelength-tuning range. However, the tradeoff would be a decrease in side-mode suppression ratio.

2) The concept of an amplitude-modulated grating [37] can be used to extend the phase-shifting range. Although originally designed to flatten the photon profile and reduce SHB effects, this idea may also be used to enhance the phase-shifting range.

## V. CONCLUSIONS

In conclusion, we have theoretically modeled a DFB laser with a curved waveguide integrated with an electroabsorption modulator which acts as a wavelength-tuning section. The characteristics of the output spectrum have been identified, and the mechanisms behind the wavelength tuning, namely, phase-shifting and current tuning have been explained using simulation results which show good agreement with experiment. The model also shows that the curved waveguide suppresses the photon density profile and reduces SHB compared to the straight waveguide case. The development of wavelength-tunable lasers with greater tuning range and higher power operation should be achievable using a curved waveguide.

## ACKNOWLEDGMENTS

This work was supported by ONR under Grant N00014-96-1-0303 and N00014-96-1-0902. The authors would like to acknowledge R. People, C. Bethea, A. M. Sergent, and W. T. Tsang for their technical expertise and discussions.

## REFERENCES

- [1] K. Kobayashi and I. Mito, "Single frequency and tunable laser diodes," *IEEE J. Lightwave Tech.*, vol. 6, pp. 1623-1633, 1988.
- [2] H. Kawaguchi, "Progress in optical functional devices using two-section laser diodes/amplifiers," *IEE Proceedings-J*, vol. 140, pp. 3-15, 1993.
- [3] Y. Kawamura, K. Wakita, Y. Yoshikuni, Y. Itaya, and H. Asahi, "Monolithic integration of a DFB laser and an MQW optical modulator in the 1.5  $\mu\text{m}$  range," *IEEE J. Quantum Electron.*, vol. 23, pp. 915-918, 1987.
- [4] M. Suzuki, Y. Noda, H. Tanaka, S. Akiba, Y. Kushihiro, and H. Issikhi, "Monolithic integration of an InGaAsP/InP distributed feedback laser and electroabsorption modulator and vapor phase epitaxy," *IEEE J. Quantum Electron.*, vol. 23, pp. 915-918, 1987.
- [5] M. Aoki, M. Suzuki, H. Sano, T. Kawano, T. Ido, T. Tanawatari, K. Uomi, and A. Takai, "InGaAs/InGaAsP MQW electroabsorption modulator integrated with a DFB laser fabricated by band-gap energy control selective area MOCVD," *IEEE J. Quantum Electron.*, vol. 29, pp. 2088-2096, 1993.
- [6] T. Kato, T. Sasaki, K. Komatsu, and I. Mito, "DFB-LD/modulator integrated light source by bandgap energy controlled selective MOVPE," *Electron. Lett.*, vol. 28, pp. 153-154, 1992.
- [7] T. Tanbun-Ek, Y. K. Chen, J. A. Grenko, E. K. Byrne, J. E. Johnson, R. A. Logan, A. Tate, A. M. Sergeant, K. W. Wecht, P. F. Sciortino, Jr., S. N. G. Chu, "Integrated DFB-DBR laser modulator grown by selective area metalorganic vapor phase epitaxy growth technique," *J. Crystal Growth*, vol. 145, pp. 902-906, 1994.
- [8] A. Ramdane, F. Devaux, N. Souli, D. Delprat, and A. Ougazaden, "Monolithic integration of multiple-quantum-well lasers and modulators for high-speed transmission," *IEEE J. Selected Topics Quantum Electron.*, vol. 2, pp. 326-335, 1996.
- [9] H. Takeuchi, K. Tsuzuki, K. Sato, M. Yamamoto, Y. Itaya, A. Sano, M. Yoneyama, and T. Otsuji, "Very high-speed light-source module up to 40 Gb/s containing an MQW electroabsorption modulator integrated with a DFB laser," *IEEE J. Selected Topics Quantum Electron.*, vol. 3, pp. 336-343, 1997.
- [10] H. Nakajima, J. Charil, S. Slempek, A. Gloukhian, B. Pierre, J. Landreau, and Y. Raffle, "Very high-speed wavelength switching capability Franz-Keldysh electroabsorption DFB lasers," *Optical Fiber Conf. Tech. Digest*, p. 276, 1996.
- [11] T. Tanbun-Ek, L. Adams, G. Nykolak, C. Bethea, R. People, A. Sergeant, P. Wisk, P. Sciortino, Jr., S. Chu, T. Fullowan, and W. T. Tsang, "Broad-band tunable electroabsorption modulated laser for WDM application," *IEEE J. Selected Topics Quantum Electron.*, vol. 3, pp. 960-966, 1997.
- [12] A. Katzir, A. C. Livanos, and A. Yariv, "Chirped-grating output couplers in dielectric waveguides," *Appl. Phys. Lett.*, vol. 30, pp. 225-226, 1977.
- [13] P. Zhou and G. S. Lee, "Chirped grating  $\lambda/4$  shifted DFB laser with uniform longitudinal field distribution," *Electron. Lett.*, vol. 26, pp. 16660-1661, 1990.
- [14] M. Okai, T. Tsuchiya, K. Uomi, N. Chinone, and T. Harada, "Corrugation-pitch modulated MQW-DFB lasers with narrow spectral linewidth," *IEEE J. Quantum Electron.*, vol. 27, pp. 1767-1772, 1991.
- [15] W. T. Tsang, R. M. Kapre, R. A. Logan, and T. Tanbun-Ek, "Control of lasing wavelength in distributed feedback lasers by angling the active stripe with respect to the grating," *IEEE Photon. Technol. Lett.*, vol. 5, pp. 10-12, 1993.
- [16] H. Hillmer, A. Grabmaier, S. Hansmann, H.-L. Zhu, H. Burkhard, and K. Magari, "Tailored DFB lasers properties by individually chirped gratings using bent waveguide," *IEEE J. Selected Topics Quantum Electron.*, vol. 1, pp. 356-362, 1995.
- [17] J. Salzman, H. Olesen, A. Moller-Larson, O. Albrechtsen, J. Hanberg, J. Norregaard, B. Jonsson, and B. Tromborg, "Distributed feedback lasers with an S-bent waveguide for high-power single-mode operation," *IEEE J. Selected Topics Quantum Electron.*, vol. 1, pp. 346-355, 1995.
- [18] W. Fang, S. L. Chuang, T. Tanbun-Ek, and Y. K. Chen, "Modeling and experiment of 1.55  $\mu\text{m}$  integrated electroabsorption modulator with distributed-feedback laser," *Proc. SPIE: Optoelectronic Integrated Circuits*, Eds. Y. S. Park and R. V. Ramaswamy, vol. 3006, pp. 207-215, 1997.
- [19] W. Fang, A. Hsu, S. L. Chuang, T. Tanbun-Ek, and A. M. Sergeant, "Measurement and modeling of distributed-feedback Lasers with spatial hole burning," *IEEE J. Selected Topics Quantum Electron.*, vol. 3, pp. 547-554, 1997.
- [20] C. H. Chen and G. Griffel, "Static, dynamic, and noise analysis of multisection DFB lasers using frequency-domain transmission line model," *IEEE J. Quantum Electron.*, vol. 34, pp. 1533-1544, 1998.
- [21] C. S. Chang, S. L. Chuang, J. R. Minch, W. Fang, Y. K. Chen, and T. Tanbun-Ek, "Amplified spontaneous emission spectroscopy in strained quantum-well lasers," *IEEE J. Selected Topics Quantum Electron.*, vol. 1, pp. 1100-1107, 1995.
- [22] S. Chinn, "Effects of mirror reflectivity in a distributed-feedback laser," *IEEE J. Quantum Electron.*, vol. 9, pp. 574-580, 1973.
- [23] M. Kitamura, M. Yamaguchi, K. Emura, I. Mito, and K. Kobayashi, "Lasing Mode and Spectral Linewidth Control by Phase Tunable Distributed Feedback Laser Diodes with Double Channel Planar Buried Heterostructure (DFB-DC-PBH LD's)," *IEEE J. Quantum Electron.*, vol. 21, pp. 415-417, 1985.
- [24] H. Olesen, X. Pan, and B. Tromborg, "Theoretical Analysis of Tuning Properties for a Phase-Tunable DFB Laser," *IEEE J. Quantum Electron.*, vol. 24, pp. 2367-2375, 1987.
- [25] M. Aoki, K. Uomi, T. Tsuchiya, S. Sasaki, M. Okai, and N. Chinone, "Quantum size effect on longitudinal spatial hole burning in MQW  $\lambda/4$ -shifted DFB lasers," *IEEE J. Quantum Electron.*, vol. 27, pp. 1782-1789, 1991.
- [26] F. Girardin, G. H. Duan, and A. Talneau, "Modeling and measurement of spatial-hole-burning applied to amplitude modulated coupling distributed feedback lasers," *IEEE J. Quantum Electron.*, vol. 3, pp. 834-841, 1995.
- [27] M. R. Phillips, T. E. Darcie, and E. J. Flynn, "Experimental measure of dynamic spatial-hole burning in DFB lasers," *IEEE Photon. Tech. Lett.*, vol. 4, pp. 1201-1203, 1992.
- [28] S. Hansmann, H. Walter, H. Hillmer, and H. Burkhard, "Static and dynamic properties of InGaAsP-InP distributed feedback lasers - A detailed comparison between experiment and theory," *IEEE J. Quantum Electron.*, vol. 30, pp. 2477-2484, 1994.
- [29] I. Orfanos, T. Spicopoulos, A. Tsigopoulos, and C. Caroubalos, "A tractable above-threshold model for the design of DFB and phase-shifted DFB lasers," *IEEE J. Quantum Electron.*, vol. 27, pp. 946-956, 1991.
- [30] M. G. Davis and R. F. O'Dowd, "A transfer matrix method based large-signal dynamic model for multielectrode DFB lasers," *IEEE J. Quantum Electron.*, vol. 30, pp. 2458-2466, 1994.
- [31] P. Correc, "Stability of phase-shifted DFB lasers against hole burning," *IEEE J. Quantum Electron.*, vol. 30, pp. 2467-2476, 1994.
- [32] S. F. Yu, "A quasi-three-dimensional large-signal dynamic model of distributed feedback lasers," *IEEE J. Quantum Electron.*, vol. 32, pp. 424-432, 1996.
- [33] H. Soda, Y. Kotaki, H. Sudo, H. Ishikawa, S. Yamakoshi, and H. Imai, "Stability in single longitudinal mode operation in GaInAsP/InP phase adjusted DFB lasers," *IEEE J. Quantum Electron.*, vol. 23, pp. 804-814, 1987.
- [34] A. Hsu, W. Fang, S. L. Chuang, T. Tanbun-Ek, C. Bethea, and R. People, "Integrated tunable laser with mode selection modulator," *Photonics West*, San Jose, CA, January 24-30, 1998.
- [35] A. Hsu, W. Fang, and S. L. Chuang, "Modeling of normal and backward integrated electroabsorption modulator and laser" *Integrated Photonics Research*, Victoria, British Columbia, Canada, March 29-April 3, 1998.
- [36] H. Ghafouri-Shiraz and B. S. K. Lo, *Distributed Feedback Laser Diodes*, New York, NY: Wiley, 1996.
- [37] G. Morthier, K. David, P. Vankwikelberge, and R. Baets, "A new DFB-laser diode with reduced spatial hole burning," *IEEE Photon. Technol. Lett.*, vol. 2, pp. 388-390, 1990.

A. Hsu.  
  
S. L. Chuang.  
  
W. Fang.  
  
L. E. Adams.  
  
G. Nykolak.  
  
T. Tanbun-Ek.

Fig. 1. Top: A side view schematic of the two-section wavelength-tunable laser which consists of a DFB laser section at the AR side and a modulator at the HR side of the device which tunes the lasing wavelength.  $L_{total}$  is the length of the entire device,  $L_{DFB}$ ,  $L_{iso}$ , and  $L_{mod}$  are the lengths of the DFB laser, isolation, and modulator sections, respectively,  $l_1 = L_{DFB}$ , and  $l_2 = L_{DFB} + L_{iso}$ . Bottom: A top view schematic illustrating the curved waveguide of the DFB laser section.

Fig. 2. (a) Measured spectrum of a conventional HR-AR coated DFB laser. The spectrum typically has a lasing mode with good SMSR on one side of the stopband and side modes with amplitudes which decrease gradually for shorter and longer wavelengths away from the stopband. (b) Measured spectrum for the integrated wavelength-tunable laser. This spectrum differs from the conventional DFB laser in that the stopband is less visible, the modes alternate amplitudes away from the stopband, and competing side modes are present on either side of the lasing mode. (c) Theoretically calculated spectrum of the integrated wavelength-tunable laser. This spectrum shows similar features to the experimentally measured spectrum in (b).

Fig. 3. (a) Modes for a one-section DFB laser, where the modes show a well-defined stopband. (b) Modes for the two-section integrated laser-modulator: The modes show a splitting near the stopband, the upper modes corresponding to the modulator region and the lower modes corresponding to the DFB laser region.

Fig. 4. The theoretically calculated threshold gain of the modes for an AR/AR coated DFB laser as a function of wavelength for (a)  $W = 0\mu\text{m}$ , (b)  $W = 5\mu\text{m}$ , and (c)  $W = 15\mu\text{m}$ . In general, increasing the width of curved waveguide  $W$  produces a mode-flattening effect around the stopband, which can enhance mode tunability.

Fig. 5. (a) Measured spectrum of the integrated device at modulator voltage values of 0, +0.47, +0.78, +0.87, +0.92, and +1.03. (b) Theoretically calculated spectrum of the integrated devices at modulator voltage values of 0, +0.65, +0.75, +0.85, +0.95, and +1.10.

Fig. 6. (a) Measured spectrum of the integrated device at modulator voltage values of 0, -0.45, and -0.78. (b) Theoretically calculated spectrum of the integrated devices at modulator voltage values of 0, -0.50, and -0.90.

Fig. 7. Measured and theoretically calculated values of the lasing wavelength as a function of modulator voltage. The closed circles represent measured lasing wavelengths. The lines represent observed lasing wavelengths and are accurate to within  $\pm 1$  angstrom. The open triangles represent the theoretically calculated values.

Fig. 8. The theoretically calculated photon density as a function of longitudinal cavity position for the straight waveguide ( $W=0$   $\mu\text{m}$ ) and curved waveguide ( $W=10$   $\mu\text{m}$ ) cases. The solid lines are for  $V_{\text{mod}}=0$ , and dashed lines are for a different lasing mode at  $V_{\text{mod}}=+0.65$ . The curved waveguide shows less perturbation in the photon density profile and therefore less SHB effects compared to the straight waveguide case.

Table I

Parameter List Used for Simulations	
power reflectivity at HR facet $R_{HR}$	0.99
power reflectivity at AR facet $R_{AR}$	0.01
phase at HR facet $\phi_{HR}$	$30^\circ$
phase at AR facet $\phi_{AR}$	$0^\circ$
coupling coefficient-length product $\kappa L$	3.0
length of laser section $L_{DFB}$ ( $\mu m$ )	360
length of isolation section $L_{ISO}$ ( $\mu m$ )	80
length of modulator section $L_{MOD}$ ( $\mu m$ )	260
grating pitch $\Lambda_o$ ( $\mu m$ )	0.2308
S-bend parameter $L_1$ ( $\mu m$ )	47
S-bend parameter $L_B$ ( $\mu m$ )	133
S-bend parameter $W$ ( $\mu m$ )	10
group index $n_g$	3.6
linewidth enhancement factor $\alpha_e$	4
optical confinement factor $\Gamma$	0.03
transparent carrier density $N_o$ ( $cm^{-3}$ )	$1.5 \times 10^{-18}$
differential gain $g'$ ( $cm^{-2}$ )	$2.7 \times 10^{-16}$
$dn_{leak}/dV_{mod}$ ( $V^{-1}$ )	0.002169
$dg/dV_{mod}$ ( $cm^{-1} V^{-1}$ )	8.0
$dn/dV_{mod}$ for $V_{mod} > 0$ ( $V^{-1}$ )	0.013135
$dn/dV_{mod}$ for $V_{mod} < 0$ ( $V^{-1}$ )	0.01129
group velocity $v_g$ (m/s)	$8.33 \times 10^8$
dispersion parameter $s$	0.21930

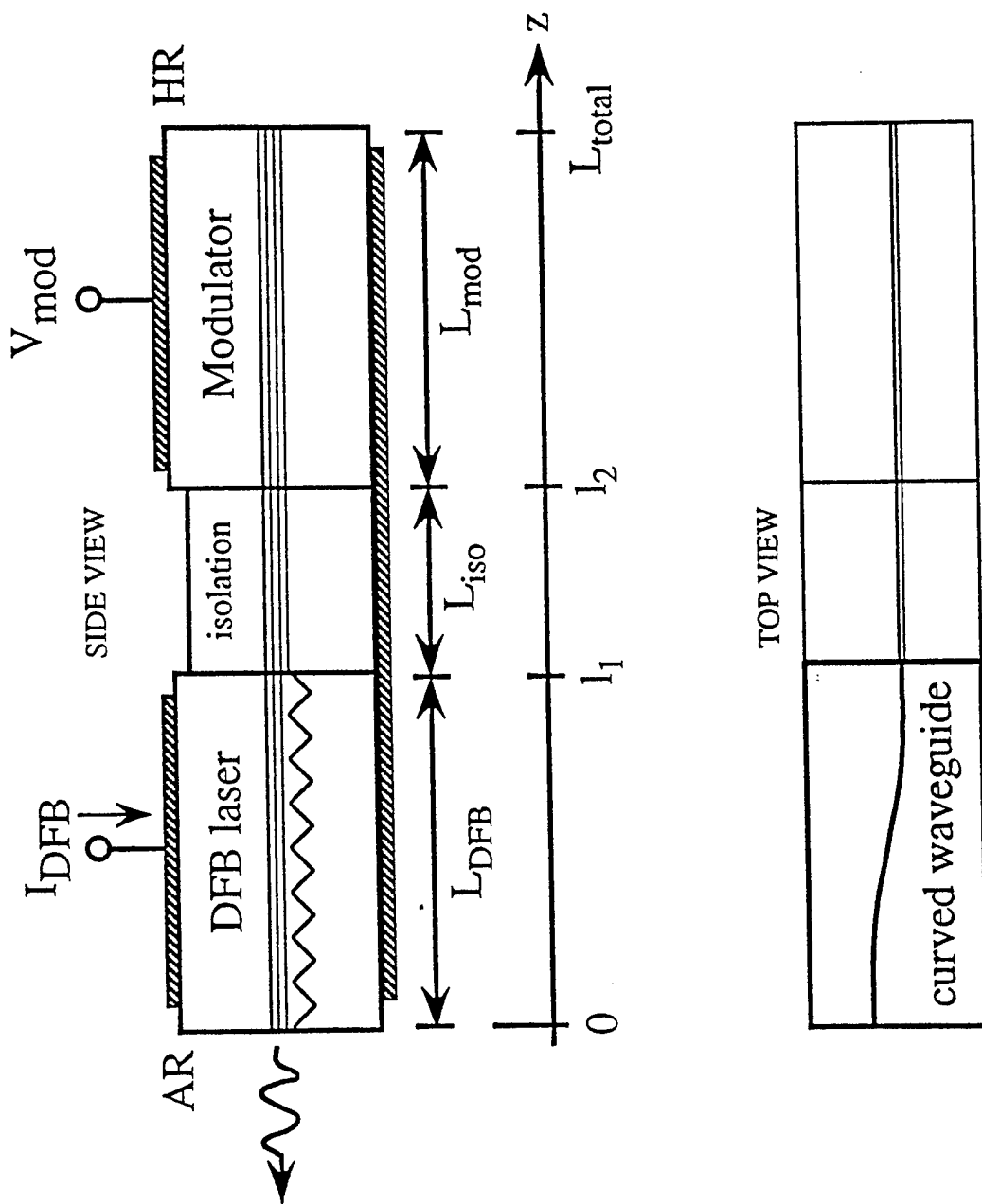
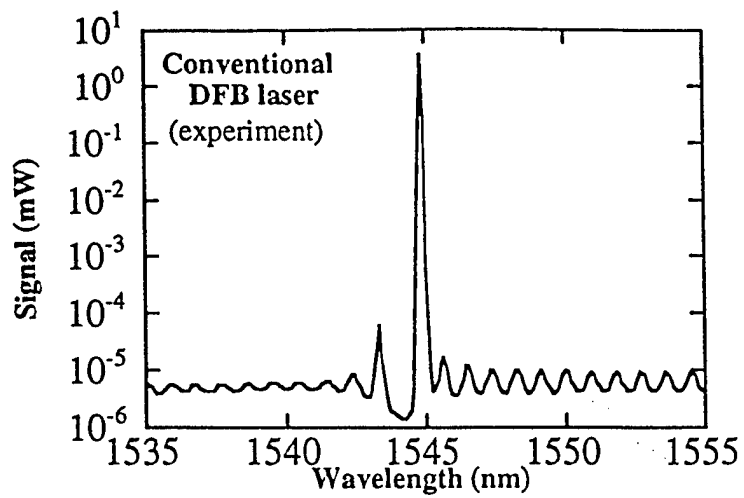
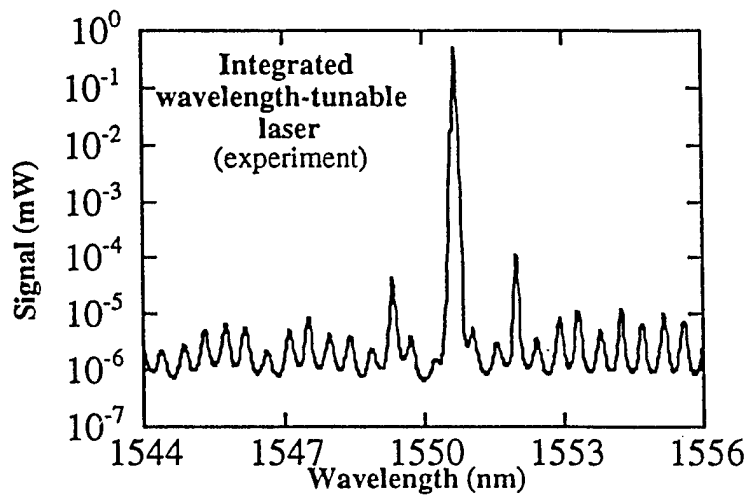


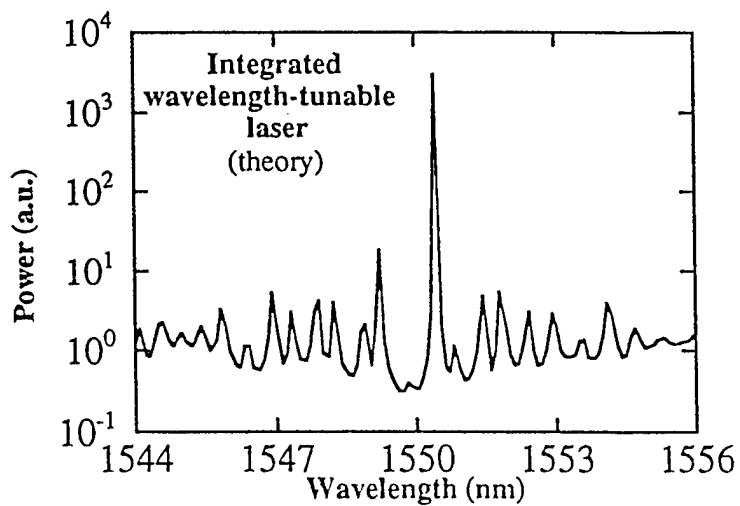
Figure 1



(a)

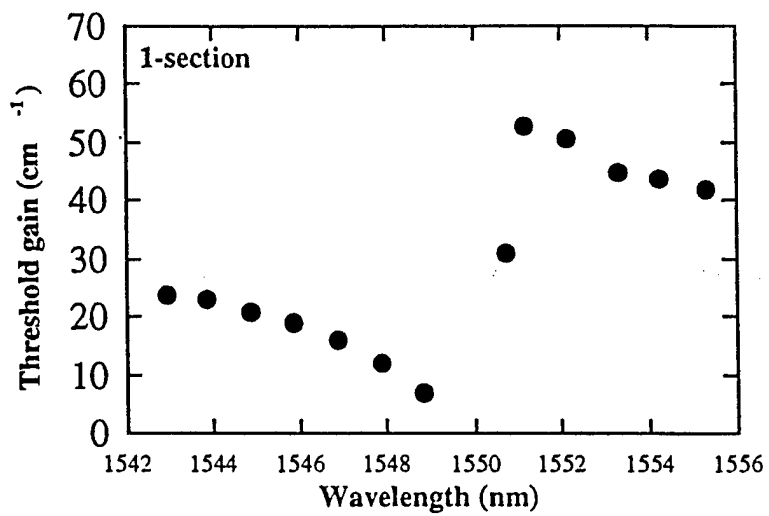


(b)

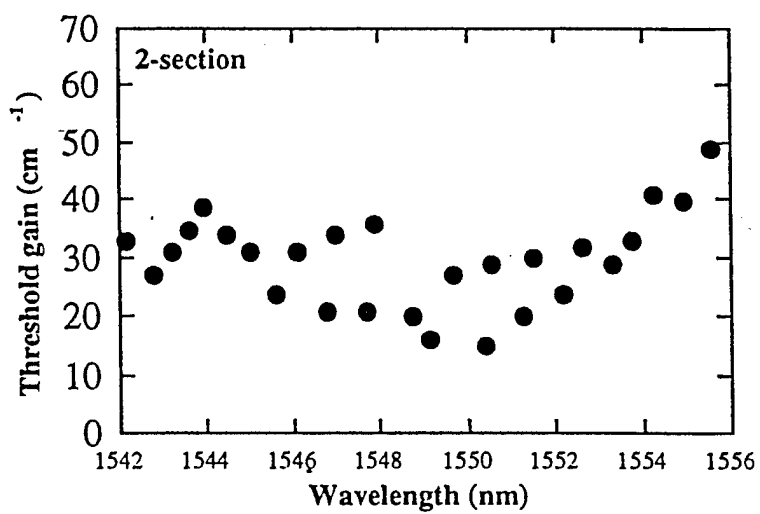


(c)

Figure 2(a),(b),(c)

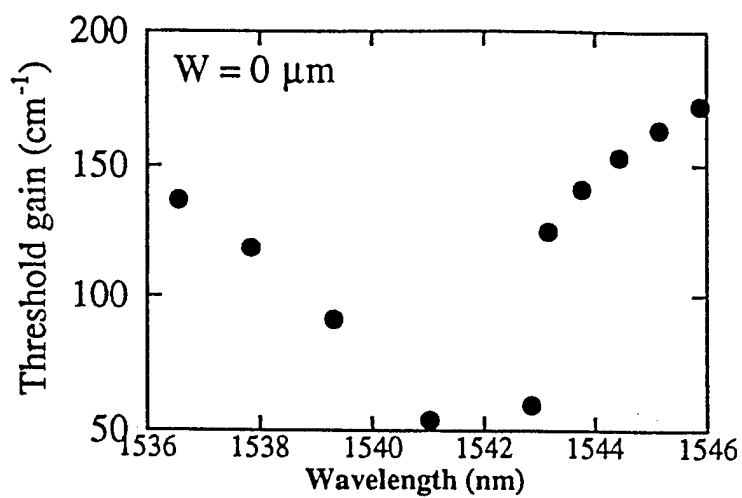


(a)

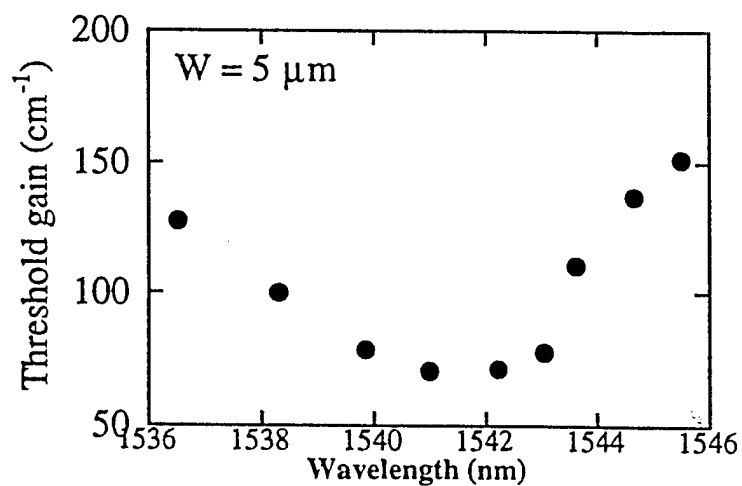


(b)

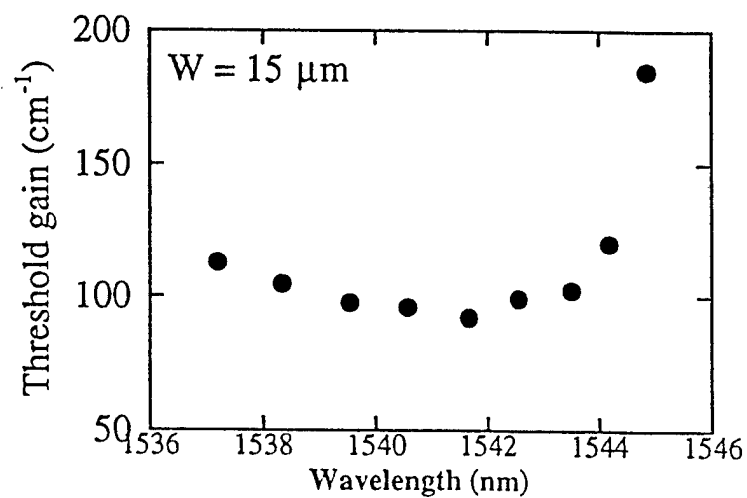
Figure 3 (a), (b)



(a)

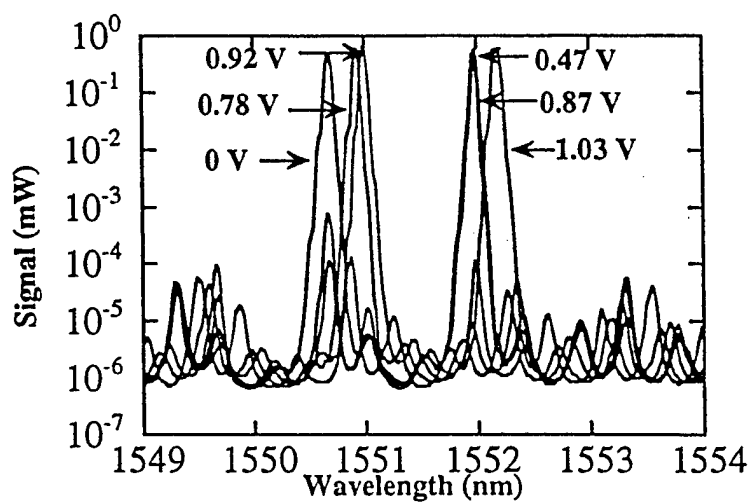


(b)

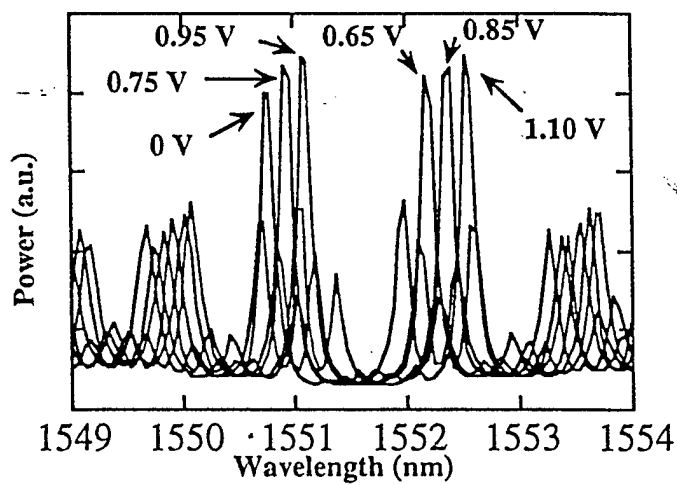


(c)

Figure 4 (a), (b), (c)

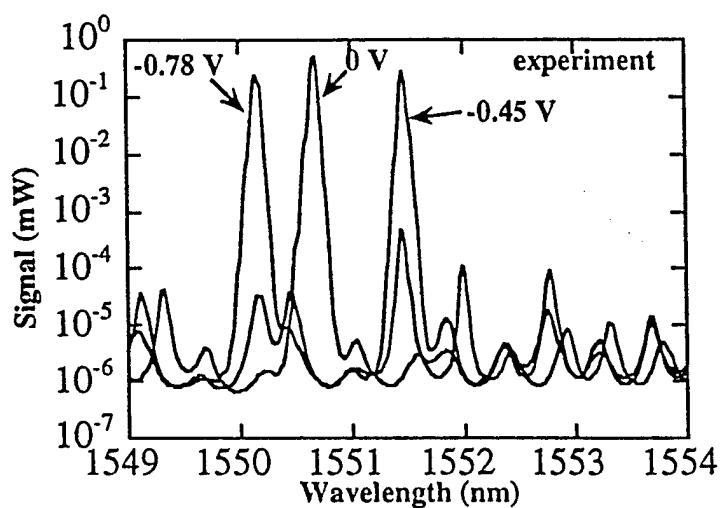


(a)

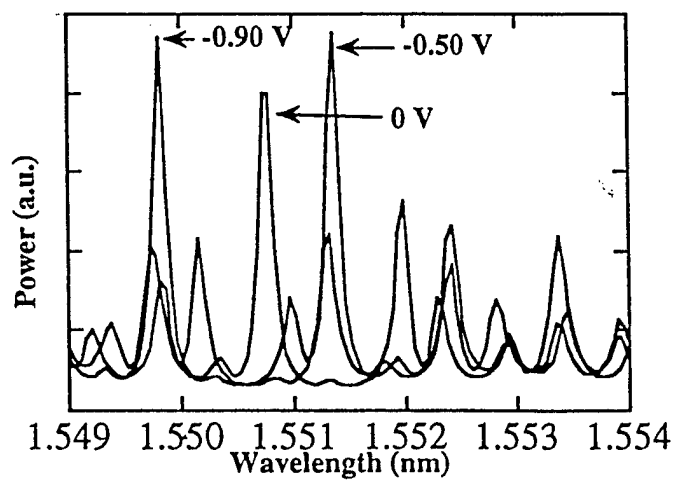


(b)

Figure 5 (a) (b)



(a)



(b)

Figure 6(a), (b).

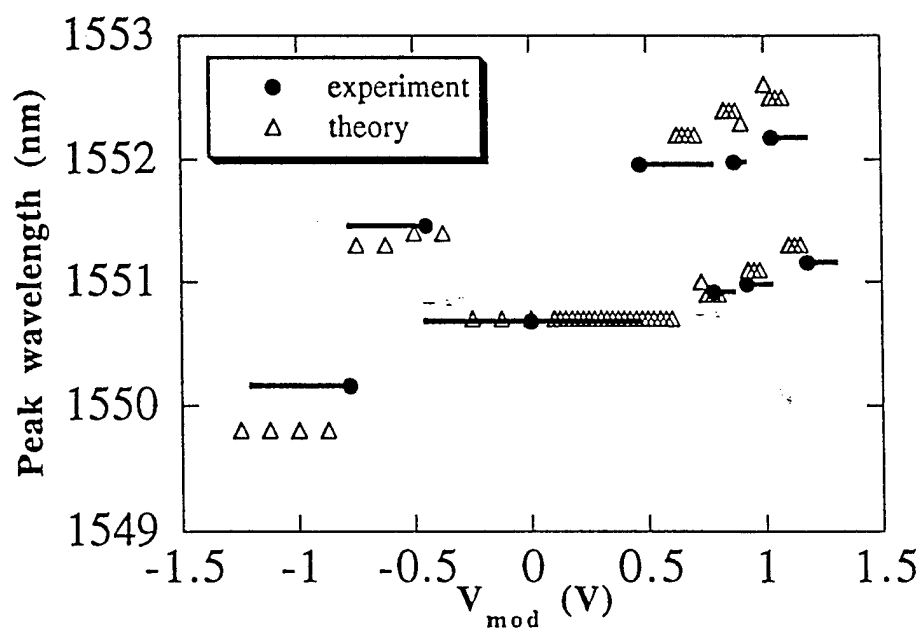


Figure 7

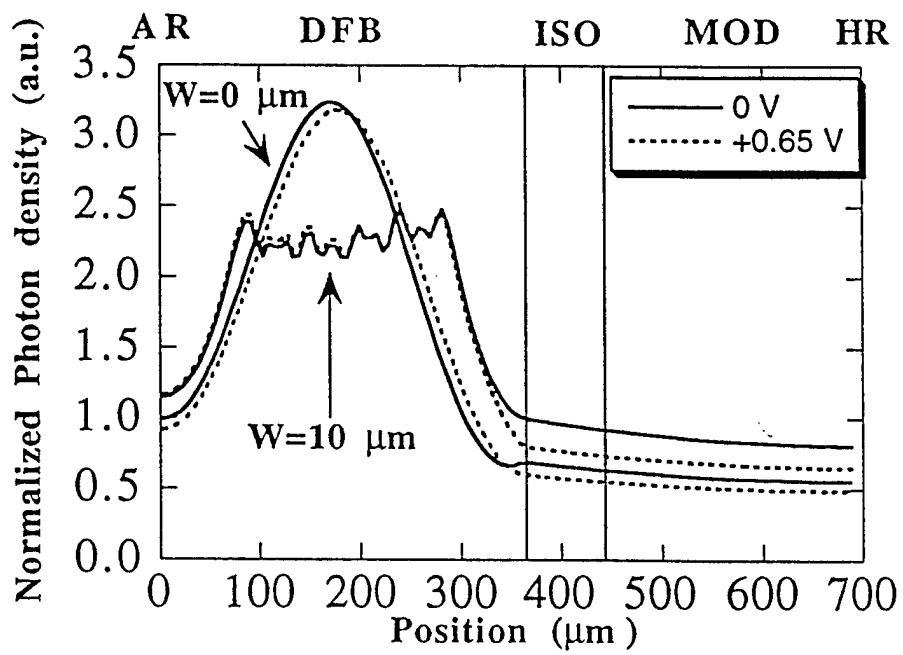


Figure 8

# Wavelength Conversion in Distributed-Feedback Lasers

Jeffrey R. Minch, *Student Member, IEEE*, Chih-Sheng Chang, *Member, IEEE*, and Shun-Lien Chuang, *Fellow, IEEE*

**Abstract**—We present both theoretical and experimental studies of four-wave mixing in a distributed-feedback (DFB) laser. The measured amplified spontaneous emission and probe gain spectra are also used to extract the DFB laser parameters. We use mean-field theory to investigate both nearly degenerate and non-degenerate four-wave mixings. For small pump-probe detunings, the dependence of multiple conjugate waves on the pump and probe powers is measured. For larger detunings, the gain of the probe signal and the conversion efficiency are measured in great detail up to a detuning of  $\pm 550$  GHz. The measured conversion efficiencies as a function of the pump-probe detuning and the power scaling laws are compared with those of the theoretical results. We also demonstrate the DFB cavity effects on the conversion efficiency spectrum.

**Index Terms**—Amplified spontaneous emission, distributed-feedback lasers, optical frequency conversion, optical mixing, wavelength-division multiplexing.

## I. INTRODUCTION

FOUR-WAVE MIXING (FWM) is one of the top contending technologies for wavelength conversion applications in future multiple wavelength telecommunication systems [1]. Wavelength conversion using four-wave mixing in semiconductor optical amplifiers has been demonstrated at high bit rates [2]–[5] and for frequency shifts of several THz [6]. Four-wave mixing is one of the few technologies which converts amplitude and frequency modulation equally well and has the ability to convert multiple signals in parallel.

Most four-wave mixing experiments for wavelength conversion reported in the literature use a semiconductor optical amplifier (SOA) as the mixing device. A strong external pump signal, and a weaker external probe signal, are typically injected into the SOA and the new signal, called the conjugate wave, is extracted from the device. A simpler method to obtain four-wave mixing is to use a distributed-feedback (DFB) laser as the mixing device. It is well known that DFB lasers provide a single, stable lasing mode. This feature provides a mixing medium with a very intense pump beam already in the cavity. All that is needed is an external probe signal to be injected into the cavity to create four-wave mixing. Thus, only two laser devices are needed to perform the experiment.

Studies of four-wave mixing in DFB lasers for small detunings have recently been reported [7], [8]. Also, four-wave mixing with higher detunings (greater than 1 THz) has been

observed for a conventional DFB laser [9], although restricted to a few cavity resonances, and a quarter-wavelength shifted DFB laser [10]. Recently, we observed higher-order mixing peaks for small detunings of the probe beam from the pump and demonstrated the dependence of the scaling law of the power of the conjugate waves on the powers of the pump and probe signals [11]. We also studied the efficiency of the four-wave mixing wavelength conversion process up to detunings of  $\pm 550$  GHz.

In this paper, we present new experimental data for the probe gain and conversion efficiency spectra and compare with the results of a general theory for four-wave mixing inside a cavity of a laser operating above threshold. The probe gain and the amplified spontaneous emission spectrum from the DFB lasers are measured and compared with our theoretical model with excellent agreement. Our experimental results for the four-wave mixing are also well explained by the theoretical model. The general FWM theory includes carrier density modulation (CDM), spectral-hole burning (SHB), and carrier heating (CH) and can thus be used for both nearly degenerate and nondegenerate detuning cases. Two special cases are derived to account for our experimental conditions. For the nearly degenerate case, we focus on the multiple conjugate waves and their dependences on both the powers of the pump and probe waves. The contributions from the SHB and CH nonlinearities are negligible in this case. We keep the general power level of both the pump and probe waves. For the conversion efficiency measurements, we consider a probe wave power much smaller than the pump power. An undepleted pump power approximation is then used to consider the FWM conversion efficiency for the whole range of the detuning frequency.

In Section II, we first derive an expression for the gain of a signal injected into a DFB cavity for comparison with the probe gain spectrum. We then present a general theory for four-wave mixing in a DFB laser. We detail our experimental measurements in Section II. In Section III, we discuss our experimental results and compare with the theory. Finally, in Section IV, we end with a brief conclusion.

## II. THEORY

### A. Probe Gain

Light traveling in a DFB cavity can be described with an electrical field of the form

$$E(z) = \hat{y}U(x) [A(z)e^{i\beta_0 z} + B(z)e^{-i\beta_0 z}] \quad (1)$$

Manuscript received December 3, 1996; revised March 25, 1997. This work was supported by the National Science Foundation under Grant ECS 95-22864 and by the U.S. Office of Naval Research under Grant N00014-96-1-0303.

The authors are with the University of Illinois at Urbana-Champaign, Department of Electrical and Computer Engineering, Urbana, IL 61801 USA. Publisher Item Identifier S 1077-260X(97)04586-3.

where  $U(x)$  is the transverse waveguide mode profile,  $\beta_0 = m\pi/\Lambda$  is the Bragg wave number where  $\Lambda$  is the period of the grating and  $m$  is the order of the grating, and  $A(z)$  and  $B(z)$  are the coefficients representing the slowly varying amplitudes of the forward and backward propagating waves, respectively. These quantities obey the well-known coupled-mode equations [12] whose solutions can be written as

$$A(z) = A_0 e^{iqz} + B_0 r_m e^{-iqz} \quad (2)$$

$$B(z) = A_0 r_p e^{iqz} + B_0 e^{-iqz} \quad (3)$$

where

$$r_p = \frac{\kappa_{ba}}{q + \Delta\beta} \quad (4)$$

$$r_m = \frac{-\kappa_{ab}}{q + \Delta\beta} \quad (5)$$

$$q = \pm \sqrt{(\Delta\beta)^2 + \kappa_{ab}\kappa_{ba}} \quad (6)$$

$$= q_r + iq_i \quad (7)$$

and  $\Delta\beta = \beta - \beta_0$  where  $\beta = k_0 n_{\text{eff}} - i(G/2)$  is the propagation constant of the guided (fundamental) optical mode, with  $n_{\text{eff}}$  as the effective refractive index,  $k_0$  as the wave number in free-space and  $G$  is the net modal gain.  $\kappa_{ab}$  and  $\kappa_{ba}$  are the coupling coefficients of the DFB grating.  $A_0$  and  $B_0$  are constants.

Assume that the facet at  $z = 0$  has a field reflection coefficient  $r_1$  and the facet at  $z = L$  has a reflection coefficient  $r_2$ . For an incident (probe) wave at  $z = 0$  with an electric field  $E_{\text{in}}$ , the boundary conditions are

$$A(0) = r_1 B(0) + t_{12} E_{\text{in}} \quad (8)$$

$$r_2 e^{2i\beta_0 L} A(L) = B(L) \quad (9)$$

$$E_{\text{out}} = t_{21} A(L) \quad (10)$$

where  $t_{12}$  is the field transmission coefficient from the air into the semiconductor and  $t_{21}$  is the transmission coefficient from the semiconductor into the air. We derive the expression for the power gain of the incident electric field to be

$$\begin{aligned} G_p &= \frac{P_{\text{out}}}{P_{\text{in}}} \\ &= \frac{|E_{\text{out}}|^2}{|E_{\text{in}}|^2} \\ &= \frac{|t_{12} t_{21}|^2 |(1 + c_2 r_m) e^{iqL}|^2}{|1 - r_1 r_p|^2 |1 - c_1 c_2 e^{2iqL}|^2} \end{aligned} \quad (11)$$

where the coefficients  $c_1$  and  $c_2$  are

$$c_1 = \frac{r_1 - r_m}{1 - r_1 r_p} \quad (12)$$

$$c_2 = \frac{r_2 e^{2i\beta_0 L} - r_p}{1 - r_2 e^{2i\beta_0 L} r_m} \quad (13)$$

Note that the power gain expression (11) is derived without the presence of the pump wave. The calculated power gain spectrum of the probe wave using (11) will be compared with the measured data to extract the parameters for the mixing DFB laser.

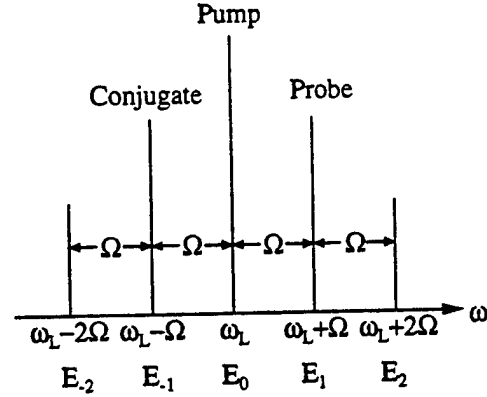


Fig. 1. A plot showing pump, probe, and multiple conjugate waves used in the four-wave-mixing theory.

### B. Four-Wave Mixing Theory

We first consider a general model for the four-wave mixing for both nearly degenerate and nondegenerate cases. The three mechanisms: carrier-density modulation, spectral-hole burning, and carrier heating are treated with equal footing. The electrical field inside the mixing laser cavity is expressed as  $E^L = E(t) \exp(-i\omega_L t)$  where  $\omega_L$  is the frequency of the mixing laser (pump beam). Similarly, the electrical field of the injection laser beam (probe beam) is written as  $E_{\text{in}}^L = E_{\text{in}}(t) \exp[-i(\omega_L + \Omega)t]$  where  $\Omega$  is the detuning frequency between the pump and probe beams. Based on the mean-field theory [7], [8], the rate equations for the carrier density  $N(t)$  and field  $E(t)$  are

$$\frac{dN}{dt} = \frac{J}{qd} - \frac{N}{\tau_c(N)} - \frac{\epsilon_0 n_r^2}{2\hbar\omega_L} v_g g |E|^2 \quad (14)$$

$$\frac{dE}{dt} = \Gamma v_g \left[ \frac{g}{2} - i(k - k_e) \right] E - \frac{E}{2\tau_p} + k_c E_{\text{in}} e^{-i\Omega t} \quad (15)$$

where  $J$  is the injection current density,  $q$  is the magnitude of a unit electron charge,  $d$  is the thickness of the active region,  $v_g$  is the group velocity,  $\hbar$  is Planck's constant,  $n_r$  is the refractive index,  $\tau_c$  and  $\tau_p$  are the carrier and photon lifetimes, respectively,  $k_c$  is the coupling constant which accounts for the coupling of the probe beam into the mixing cavity,  $g$  is the material gain,  $k_e$  is the wave number of the pump beam, and  $k$  is the wave number of the mixing device. In general, both  $g$  and  $k$  are functions of the carrier density  $N$  and the optical field intensity  $S = |E|^2$ .

Let us first consider that the probe beam is absent (i.e.,  $E_{\text{in}} = 0$ ). By setting the time derivative to zero and adding a subscript "e" to the variables, we obtain the threshold condition

$$\Gamma v_g g_e = \frac{1}{\tau_p} \quad (16)$$

and the field intensity of the pump beam

$$|E_e|^2 = 2 \frac{\hbar\omega_L}{\epsilon_0 n_r^2} \Gamma \tau_p \left( \frac{J - J_{th}}{qd} \right) \quad (17)$$

where the threshold current density is  $J_{th} = qdN_e/\tau_c(N_e)$ . If we include the probe beam, we can express the carrier density

$N$ , the optical field  $E$ , and the optical field intensity  $S$  as linear combinations of harmonics with frequencies equal to  $m\Omega$ , where  $m$  is an integer [13]

$$E = \sum_{m=-M_1}^{M_2} E_m e^{-im\Omega t} \quad (18)$$

$$S = \sum_{m=-(M_1+M_2)}^{M_1+M_2} S_m e^{-im\Omega t} \quad (19)$$

$$N = N_e + \sum_{m=-(M_1+M_2)}^{M_1+M_2} \Delta N_m e^{-im\Omega t} \quad (20)$$

where  $M_1$  and  $M_2$  are integers chosen according to the desired spectrum to be modeled. Fig. 1 illustrates the frequency relations of the optical field of the pump, probe, and multiple conjugate waves used in the four wave-mixing theory. The harmonics of the field intensity  $S_m$  are related to  $E_m$  as

$$S_m = \sum_l E_l^* E_{m+l} \quad (21)$$

where the superscript "\*" means the complex conjugate. Note that both  $S$  and  $\Delta N = N - N_e$  are real quantities. The material gain  $g$  including the nonlinear gain suppression due to the spectral-hole burning (SHB) and carrier-heating can be written as [14]

$$g(N, S) = g_o(N_e + \Delta N) \left[ 1 - \epsilon_{sh} \sum_m H_m^{sh} S_m e^{-im\Omega t} \right] - g_{ch} \sum_m H_m^{ch} S_m e^{-im\Omega t} \quad (22)$$

$$g_o(N_e + \Delta N) \approx g_o(N_e) + \frac{\partial g_o}{\partial N} (N - N_e) = g_{oe} + g' \sum_m \Delta N_m e^{-im\Omega t} \quad (23)$$

where  $g_o(N)$  is the linear part of the material gain,  $g'$  is the differential gain,  $\epsilon_{sh}$  and  $g_{ch}$  represent the relative strengths of the spectral-hole burning and carrier-heating processes, respectively, and the response functions of the two processes are [14], [15]

$$H_m^{sh} = \frac{1}{1 - im\Omega\tau_2} \quad (24)$$

$$H_m^{ch} = \frac{1}{(1 - im\Omega\tau_1)(1 - im\Omega\tau_2)} \quad (25)$$

where  $\tau_2$  is the time constant of the carrier-carrier scattering which is responsible for the intraband relaxation, and  $\tau_1$  is the time constant of the carrier-LO phonon scattering which is responsible for the heating or cooling of the carriers. Typical values [16] for the time constants  $\tau_1$  and  $\tau_2$  are 650 fs and 100 fs, respectively. A similar expression can be used to describe the wave number of the cavity  $k$ . However, for simplicity, we neglect the nonlinear effects in  $k$ .

$$k = k(N_e + \Delta N) \approx k_e - \alpha_e \frac{g'}{2} \sum_m \Delta N_m e^{-im\Omega t} \quad (26)$$

where  $\alpha_e$  is the linewidth enhancement factor. Also note that

$$g_e = g_{oe}(1 - \epsilon_{sh} |E_e|^2) - g_{ch} |E_e|^2. \quad (27)$$

By equating both sides of the rate equations with the harmonic expansions, we obtain the equations for the normalized carrier density  $[\Delta \bar{N}_m = (g'/g_e) \Delta N_m]$

$$\begin{aligned} & (1 - im\Omega) \Delta \bar{N}_m \\ & + \sum_l \left[ \bar{S}_{m-l} - \sum_{l'} \bar{\epsilon}_{sh} H_{l'}^{sh} \bar{S}_{l'} \bar{S}_{m-l-l'} \right] \Delta \bar{N}_l \\ & = |\bar{E}_e|^2 \delta_{m,0} - \frac{g_{oe}}{g_e} \bar{S}_m \\ & + \sum_l \frac{g_{oe}}{g_e} (\bar{\epsilon}_{sh} H_l^{sh} + \bar{\epsilon}_{ch} H_l^{ch}) \bar{S}_l \bar{S}_{m-l} \end{aligned} \quad (28)$$

and the normalized field ( $\bar{E}_m = E_m/E_s$ )

$$\begin{aligned} & \left[ \frac{\tau'_c}{2\tau_p} \left( 1 - \frac{g_{oe}}{g_e} \right) - im\Omega \right] \bar{E}_m + \frac{\tau'_c}{2\tau_p} \sum_l \\ & \cdot \left[ - (1 + i\alpha_e) \Delta \bar{N}_{m-l} + \frac{g_{oe}}{g_e} (\bar{\epsilon}_{sh} H_{m-l}^{sh} + \bar{\epsilon}_{ch} H_{m-l}^{ch}) \bar{S}_{m-l} \right. \\ & \left. + \sum_{l'} \bar{\epsilon}_{sh} H_{l'}^{sh} \bar{S}_{l'} \Delta \bar{N}_{m-l-l'} \right] \bar{E}_l = \bar{E}'_{in} \delta_{m,1} \end{aligned} \quad (29)$$

where

$$E_s^2 = \frac{2}{\epsilon_o n_r^2} \frac{\hbar \omega_L}{v_g g' \tau'_c} \quad (30)$$

$I_s = (\frac{1}{2}) \epsilon_o n_r^2 v_g E_s^2$  is the saturation intensity,  $\tau'_c$  is the differential carrier lifetime,  $\bar{\Omega} = \Omega \tau'_c$ ,  $\bar{E}'_{in} = k_c \tau'_c E_{in}/E_s$ ,  $\bar{S}_m = S_m/E_s^2$ ,  $\bar{\epsilon}_{sh} = \epsilon_{sh} E_s^2$ , and  $\bar{\epsilon}_{ch} = (g_{ch}/g_{oe}) E_s^2$ .

Equations (21), (28), and (29) form a system of nonlinear equations which can be solved to obtain the field harmonics  $E_m$  inside the cavity as a function of the detuning  $\Omega$ , injection probe beam intensity  $|E_{in}|^2$ , and the injection current density  $J$  (i.e.,  $|E_e|^2$ ). The general model is then further simplified to consider two of our experimental conditions.

1) *Multiple-Wave Generation From Nearly Degenerate FWM*: For the nearly degenerate FWM, we may neglect both the SHB and CH (i.e.,  $\epsilon_{sh} = 0$  and  $g_{ch} = 0$ ). The material gain is then a linear function of only the carrier density. We can then numerically integrate the rate equations (14) and (15) with the initial conditions

$$E(0) = E_e \quad (31)$$

$$N(0) = N_e. \quad (32)$$

After some initial oscillations, the optical field  $E(t)$  reaches steady state and becomes a periodic function of time. The harmonics  $E_m$ s can then be obtained by finding the coefficients of the Fourier series of the periodic part of the field.

2) *Weak Probe Beam Injection*: With a weak probe beam injection, i.e.,  $|E_{in}| \ll |E_e|$ , we consider only three waves: probe ( $E_1$ ), pump ( $E_0$ ), and conjugate ( $E_{-1}$ ), and assume that  $E_0 = E_e$  and  $\Delta N_0 = 0$ .

From (21), we have the following approximations

$$\bar{S}_0 \approx |\bar{E}_e|^2 \quad (33)$$

$$\bar{S}_1 \approx \bar{E}_e^* \bar{E}_1 + \bar{E}_e \bar{E}_{-1}^* \quad (34)$$

$$\bar{S}_{-1} = \bar{S}_1^* \quad (35)$$

$$\bar{S}_{-2} = \bar{S}_2^* \approx 0. \quad (36)$$

Using these approximations in (28) we have

$$\Delta \bar{N}_1 = A(\bar{E}_e^* \bar{E}_1 + \bar{E}_e \bar{E}_{-1}^*) \quad (37)$$

$$\Delta \bar{N}_{-1} = \Delta \bar{N}_1^* \quad (38)$$

$$A = -\frac{g_{oe}}{g_e} \frac{1 - |\bar{E}_e|^2 [\bar{\epsilon}_{sh}(1 + H_1^{sh}) + \bar{\epsilon}_{ch}(1 + H_1^{ch})]}{1 - i\bar{\Omega} + (1 - \bar{\epsilon}_{sh}|\bar{E}_e|^2)|\bar{E}_e|^2} \quad (39)$$

The above equations for  $\Delta \bar{N}_1$  and  $\Delta \bar{N}_{-1}$  can then be put into (29) for  $m = \pm 1$  to form a system of linear equations of variables  $\bar{E}_1$  and  $\bar{E}_{-1}$ .

$$\begin{bmatrix} M_{11} & M_{12} \\ M_{21} & M_{22} \end{bmatrix} \begin{bmatrix} \bar{E}_1 \\ \bar{E}_{-1} \end{bmatrix} = \begin{bmatrix} \bar{E}_{in} \\ 0 \end{bmatrix} \quad (40)$$

where

$$M_{11} = \frac{\tau'_c}{2\tau_p} \left\{ 1 - \frac{g_{oe}}{g_e} [1 - |\bar{E}_e|^2 \bar{\epsilon}_{sh}(1 + H_1^{sh}) - |\bar{E}_e|^2 \bar{\epsilon}_{ch}(1 + H_1^{ch})] - (1 + i\alpha_e)A|\bar{E}_e|^2 \right\} - i\bar{\Omega} \quad (41)$$

$$M_{12} = \frac{\tau'_c}{2\tau_p} \bar{E}_e^2 \left[ -(1 + i\alpha_e)A + \frac{g_{oe}}{g_e} (\bar{\epsilon}_{sh} H_1^{sh} + \bar{\epsilon}_{ch} H_1^{ch}) \right] \quad (42)$$

$$M_{21} = \frac{\tau'_c}{2\tau_p} (\bar{E}_e^*)^2 \left[ -(1 - i\alpha_e)A + \frac{g_{oe}}{g_e} (\bar{\epsilon}_{sh} H_1^{sh} + \bar{\epsilon}_{ch} H_1^{ch}) \right] \quad (43)$$

$$M_{22} = \frac{\tau'_c}{2\tau_p} \left\{ 1 - \frac{g_{oe}}{g_e} [1 - |\bar{E}_e|^2 \bar{\epsilon}_{sh}(1 + H_1^{sh}) - |\bar{E}_e|^2 \bar{\epsilon}_{ch}(1 + H_1^{ch})] - (1 - i\alpha_e)A|\bar{E}_e|^2 \right\} - i\bar{\Omega}. \quad (44)$$

### III. EXPERIMENTS AND COMPARISON WITH THEORY

#### A. Experimental Setup

For our experiments, we use an index-coupled DFB laser with a lasing wavelength of about 1.535  $\mu\text{m}$  as the mixing device. Fig. 2 shows a diagram of the experimental setup. Another DFB laser similar to the mixing laser is used to provide the probe signal. The probe signal is coupled into a fiber and passed through an optical isolator to eliminate injection of light from the mixing DFB laser into the probe DFB laser. The probe light is then passed through a 20-dB fiber coupler to monitor the power of the probe signal injected into the mixing DFB laser. Light emitted from the other facet

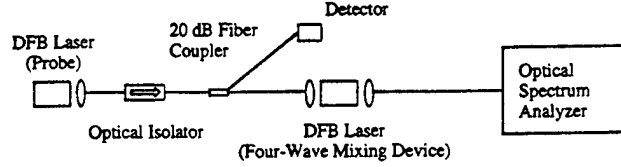


Fig. 2. A diagram showing the experimental setup for four-wave mixing using two DFB lasers. The probe beam is coupled from the first laser into an optical fiber and passed through an optical isolator to remove unwanted optical feedback. The probe power injected into the second DFB laser is monitored using a 20-dB fiber directional coupler. The output pump, probe and conjugate waves are coupled into another fiber at the other laser facet and then measured with an HP Optical Spectrum Analyzer.

of the mixing DFB laser is coupled into another fiber and monitored using an HP optical spectrum analyzer to obtain the output powers of the pump, probe, and conjugate signals. The operating temperatures of both probe and mixing DFB lasers are maintained using thermoelectric controllers. Tuning of the probe signal is accomplished by changing the operating bias current and temperature of the probe DFB laser. A single probe DFB laser has a typical span of 2.5–3.0 nm with a temperature range of 35  $^{\circ}\text{C}$  and a current range of laser threshold to 60 mA. A larger tuning range is achieved by using several different probe DFB lasers.

#### B. Characterization of Mixing Laser

In order to obtain the gain, refractive index, and DFB cavity parameters in our models, we first characterized the mixing DFB laser ( $I_{th} = 8.4$  mA) using the amplified spontaneous emission (ASE) spectrum of the laser just below threshold and at the operating bias (40 mA, 20  $^{\circ}\text{C}$ ) used in the four-wave mixing experiments. The details of this procedure are described in [17]. The ASE spectrum shown in Fig. 3(a) (40 mA, 20  $^{\circ}\text{C}$ ) allows us to obtain the gain spectrum from the ratio of the maximum and minimum envelopes based on the Hakki-Paoli method [18], [19]. Fig. 3(b) shows the extracted net round-trip gain spectrum at both 8.2 mA ( $I_{th} = 8.4$  mA) and 40 mA. Far above the bandedge, these two spectra are the same since the carrier concentration in the active region is more or less pinned above threshold. Near the bandedge, the two diverge, however, because of an increase in the background noise which leads to an artificial decrease in the extracted Hakki-Paoli gain. To obtain the true intrinsic loss level and the quasi-Fermi level separation, we must use the plateau of the net gain spectrum at 8.2 mA. Unfortunately, near the stopband region, the strong dependence of the reflectivity of the DFB grating causes the extracted data to deviate sharply from the actual gain spectrum. The actual gain must be interpolated from the surrounding data [17]. Also, an effective refractive index spectrum is extracted to match the peaks in the ASE spectrum far away from the stopband region. The effective refractive index in the vicinity of the stopband is interpolated from this data. The cavity length of the laser was measured to be about 255  $\mu\text{m}$ . Using these parameters, the coupling coefficient, the facet reflectivities, and the Bragg wavelength can be found by performing a fit of the ASE spectrum as done in reference [17]. This fit is not shown because the same parameters are used later in this section

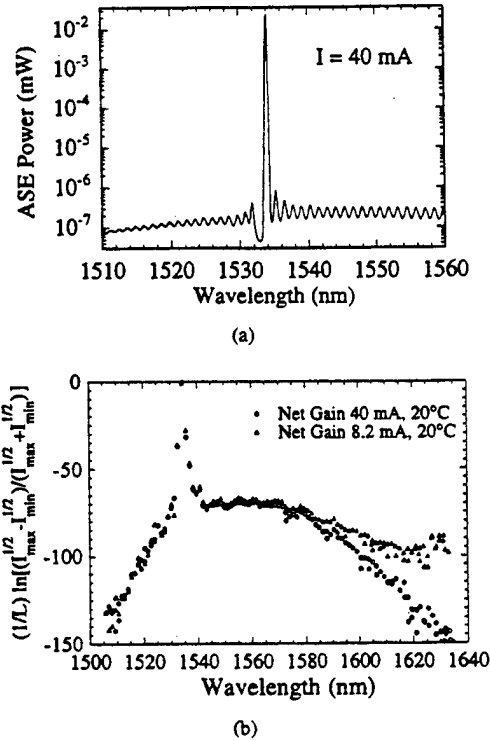


Fig. 3. (a) The measured amplified spontaneous emission spectrum of the mixing DFB laser well above threshold (40 mA, 20 °C). This spectrum is used to characterize this laser. (b) The extracted net round-trip gain of the mixing DFB laser obtained from the maxima ( $I_{\max}$ ) and the minima ( $I_{\min}$ ) of the ASE spectrum such as given in part (a) Circles show the net round-trip gain well above threshold at  $I = 40$  mA, triangles show the net round-trip gain just below the laser threshold at  $I = 8.2$  mA ( $I_{th} = 8.4$  mA).

to fit the probe gain spectrum which is nearly identical to the ASE spectrum.

### C. Power Dependence and Multiple Conjugate Waves

For our four-wave mixing measurements, we studied both pump-probe detunings in the nearly degenerate and the non-degenerate regimes. For small detunings we observed multiple conjugate signals for a single injected probe beam. Fig. 4 shows a typical spectrum demonstrating our observations. Note that the linewidths of the spectra shown in Fig. 4 are limited by the minimum resolution of the optical spectrum analyzer. The true linewidths are much narrower than those shown. By varying the coupling of the emitted light from the probe DFB laser to the optical fiber, we were able to control the power of the probe signal injected into the mixing DFB laser. This enabled us to study the dependence of higher order conjugate signals on the power of the probe. Fig. 5(a) shows the measured powers of four of the conjugate waves as a function of the measured probe power. The slopes of the lines shown on the log-log plot give the power law for each of these conjugate signals.

The dependence of the conjugate waves on the pump power is much more difficult to measure because the lasing wavelength of the mixing DFB laser will change as the injection current is changed. So, it is difficult to change the pump power without changing the pump-probe detuning at a

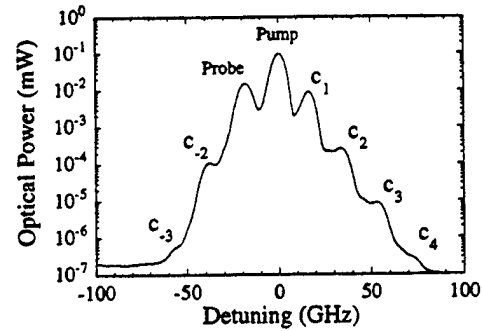


Fig. 4. A measured optical spectrum showing multiple conjugate signals for a pump and probe with a small detuning for nearly degenerate four-wave mixing.

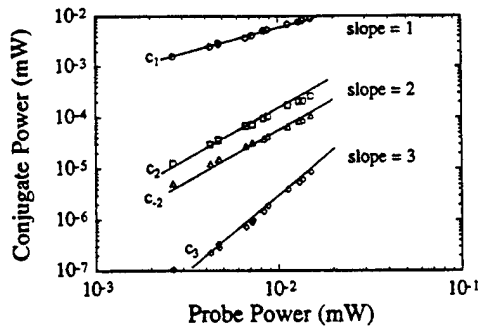
fixed temperature. In our measurements, the probe signal was tuned to a fixed detuning from the pump for each injection current used in the DFB mixing laser. As before, the power of the probe signal was varied, and the power of the output pump, probe, and conjugate signals were measured. The dependence of the conjugate powers on the pump power was obtained by selecting a pump power common to the range measured for each bias level of the mixing DFB laser and interpolating the value of the conjugate power at each bias level. The interpolated conjugate powers and the measured pump powers are shown in Fig. 5(b).

Our model for the nearly degenerate case is applied to compare with our experimental data shown in Fig. 5(a) and (b). We change the normalized injection field ( $\bar{E}_{in}$ ) and the injection current ( $\bar{E}_e$ ) and calculate the normalized power of the multiple conjugate waves. The results are shown in Fig. 5(c) and (d). A linewidth enhancement factor of  $\alpha_e = 5$  is used in the calculation. The differential carrier lifetime is treated as a fitting parameter and was found to be about 110 ps. The saturation intensity  $I_s$  is then found to be 2.35 MW/cm<sup>2</sup>. With an emitting area of  $1 \mu\text{m} \times 0.02 \mu\text{m}$ , the corresponding normalization power for Fig. 5 (c) and (d) is 0.47 mW. The slopes of the log-log plot of the theoretical probe and pump power laws are close to the experimental data. The relative magnitudes of the conjugate waves show some disagreement between experimental and theoretical results. A better estimate of the saturation intensity should improve the comparisons.

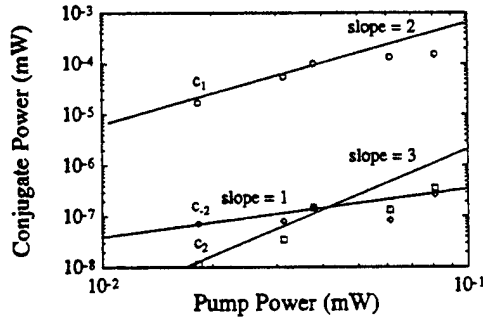
### D. Probe Gain and Conjugate Conversion Efficiency

Measurements were also made for large detunings of the pump and probe. Fig. 6 shows the measured output spectrum for several detunings of the pump and the probe. In order to maintain a constant pump power, the temperature and operating bias current of the mixing laser were held constant. The probe input power was monitored through the fiber coupler and was typically controlled to be between 10 and 100 times smaller than the pump power so that the pump signal of the mixing DFB laser would not be affected. The probe beam was tuned from about 550 GHz below to about 550 GHz above the pump frequency.

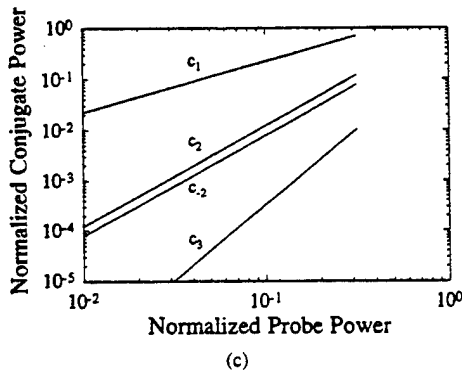
Fig. 7 shows the ratio of the measured output probe power to the measured input probe power. We have not included the



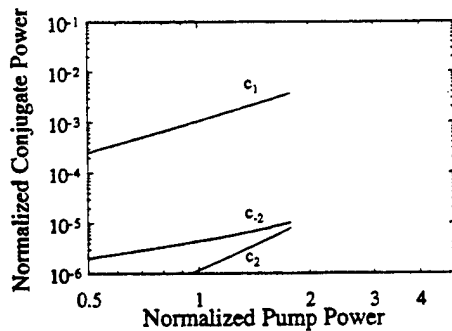
(a)



(b)



(c)



(d)

Fig. 5. Plots of the dependence of the measured multiple conjugate-wave output powers on (a) the probe power and (b) the pump power. Theoretical results for the normalized conjugate-wave intensity as a function of (c) the normalized probe intensity and (d) the normalized pump intensity are also shown. All of the powers are normalized by 0.47 mW. The slopes of the log-log plots give the power dependence on the pump or probe for each conjugate wave shown.

coupling losses from the fiber to the mixing DFB laser and from the laser to the fiber, but this factor will just scale our

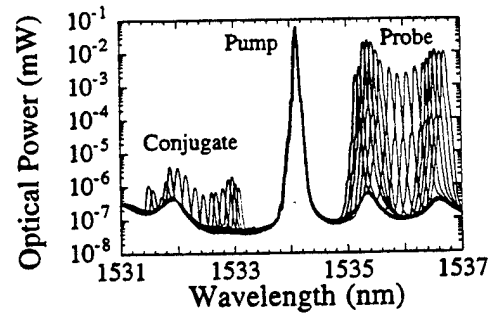


Fig. 6. Measured DFB laser spectra with several probe detunings for non-degenerate four-wave mixing.

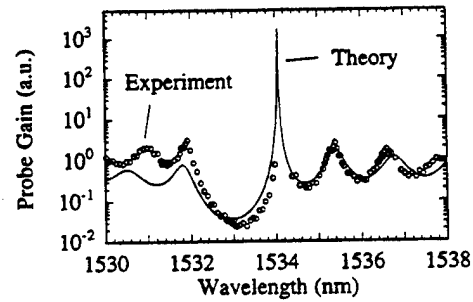


Fig. 7. A plot of the gain experienced by the probe through the DFB cavity. Symbols show the measured data and the solid line shows the best fit using parameters extracted from the laser ASE spectrum.

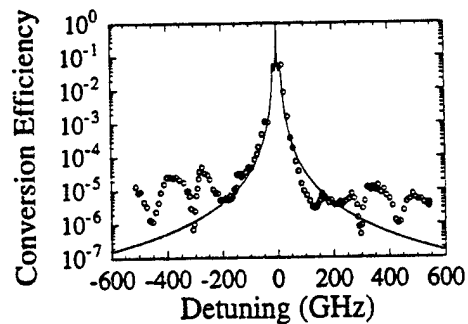


Fig. 8. Measured four-wave mixing conversion efficiency (symbols) as a function of the probe detuning. The solid curve gives a fit using the presented model based on the mean-field theory.

measured ratio by a constant. To match this spectra, we use the same parameters as before from our fit of the ASE spectrum in (11). Fig. 7 shows the best theoretical fit of the probe gain yielding  $R_1 = r_1^2 = 0.9$ ,  $\Phi_1 = 320^\circ$ ,  $R_2 = r_2^2 = 0.01$ ,  $\Phi_2 = 30^\circ$ ,  $\kappa = 66.7 \text{ cm}^{-1}$ , and  $\lambda_B = 1.5334 \text{ }\mu\text{m}$ . Fig. 8 shows the conversion efficiency of the four-wave mixing defined to be the ratio of the measured output conjugate power to the input probe power. Again, this ratio needs to be modified by the same coupling loss factor as in the probe gain in order to give the true conversion efficiency.

The weak-probe wave theory is used to study the conversion efficiency of FWM. The theoretical conversion efficiency is calculated as the product of a coupling constant and the ratio between the normalized power of the conjugate wave ( $|\bar{E}_{-1}|^2$ ) and that of the injected probe wave ( $|\bar{E}'_{in}|^2$ ). The coupling

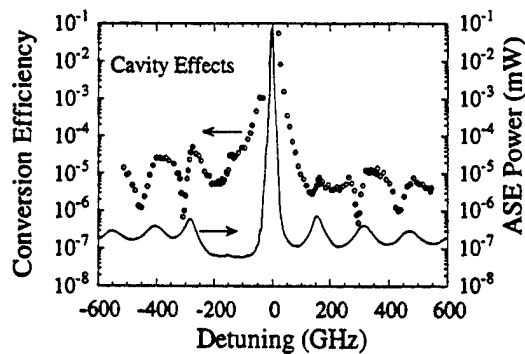


Fig. 9. A plot showing the cavity effects of the conversion efficiency. The solid line corresponds to the measured ASE power spectrum of the mixing DFB laser at the conjugate signal frequency.

constant is used to account for the coupling of the probe wave from fiber into the cavity of the mixing laser and the coupling of the conjugate wave from the cavity to the collecting fiber. We treated the coupling constant as a fitting parameter to fit the overall shape of the measured conversion efficiency. The theoretical results of the conversion efficiency are shown as the solid line in Fig. 8. The coupling constant used is 0.01. The time constants used are 650 fs and 100 fs for  $\tau_1$  and  $\tau_2$ , respectively. The normalized strength of the CH and SHB nonlinearities are  $\bar{\epsilon}_{ch} = 0.004$  and  $\bar{\epsilon}_{sh} = 0.016$ . The peaks of the solid line in Fig. 8 near detunings of  $\pm 15$  GHz are due to the resonance of the carrier density modulation. These peaks are the same as the resonance peaks which occur in direct modulation of semiconductor lasers. When the detuning is much larger than the CDM resonance frequency, the contribution from CDM to the FWM process decreases quickly and then nonlinear processes become dominant. The CH ( $\tau_1$ ) is the dominant nonlinear mechanism in the FWM process for the detuning range of our experiment data, while the contribution from the SHB ( $\tau_2$ ) is almost negligible. The conversion efficiency from the CH contribution has a much larger bandwidth than the CDM process. The experimental data show some resonance peaks which are not predicted by the theory. These resonance peaks are due to the DFB cavity resonance effects which are neglected in the mean-field theory and are explained below.

There are several mechanisms which can contribute to the overall cavity effects in the four-wave mixing efficiency spectrum. The enhancement of the probe and conjugate beams by the cavity is the most obvious effect. In Fig. 9, the conversion efficiency is superimposed with a curve showing the power of the ASE spectrum of the mixing DFB laser at 40 mA and 20 °C at the wavelength of the conjugate signal. This curve gives a very good indication of the enhancement that the cavity gives to the conjugate wave. One can see that some of the general trends of the cavity effects in the conversion efficiency correlate very well to this curve. It is difficult to correlate a similar curve showing the enhancement of the probe wave (the probe gain in Fig. 6) to the conversion efficiency because large dips, which are present in the conversion efficiency spectrum, seem to occur near the peaks in the probe gain curve. These dips are probably caused by more subtle effects, such as the

phase distribution of the created conjugate waves in the laser cavity. These effects need further investigation.

#### IV. CONCLUSION

In this paper, we have presented both theoretical and experimental investigations of wavelength conversion in a DFB laser using four-wave mixing. For detunings in the nearly degenerate regime, we observed multiple conjugate signals. We have characterized the dependence of the power of these conjugate signals on both the probe and pump powers. Our measured data agree very well with the theoretical results based on the mean-field theory. For larger detunings in the nondegenerate regime, we present a detailed measurement of the four-wave mixing conversion efficiency. We point out the noticeable DFB cavity effect on the spectrum and correlate the effects with the cavity enhancement of the conjugate wave.

#### REFERENCES

- [1] S. J. B. Yoo, "Wavelength conversion technologies for WDM network applications," *J. Lightwave Technol.*, vol. 14, pp. 955–966, 1996.
- [2] R. Schnabel, W. Pieper, M. Ehrhardt, M. Meiselt, and H. G. Weber, "Wavelength conversion and switching of high speed data signals using semiconductor laser amplifiers," *Electron. Lett.*, vol. 29, pp. 2047–2048, 1993.
- [3] P. Iannone and P. Prucnal, "Multinanometer wavelength conversion of 2.5 and 10 Gb/s optical channels in an injection-locked semiconductor laser," *IEEE Photon. Technol. Lett.*, vol. 30, pp. 988–991, 1994.
- [4] R. Ludwig and G. Raybon, "BER measurements of frequency converted signals using four-wave mixing in a semiconductor laser amplifier at 1, 2.5, 5, and 10 Gbit/s," *Electron. Lett.*, vol. 30, pp. 338–339, 1994.
- [5] J.-M. Liu and T. B. Simpson, "Four-wave mixing and optical modulation in a semiconductor laser," *IEEE J. Quantum Electron.*, vol. 30, pp. 957–965, 1994.
- [6] J. Zhou, N. Park, K. Vahala, M. Newkirk, and B. Miller, "Four-wave mixing wavelength conversion efficiency in semiconductor traveling-wave amplifiers measured to 65 nm of wavelength shift," *IEEE Photon. Technol. Lett.*, vol. 6, pp. 984–987, 1994.
- [7] A. Mecozzi, A. D'Ottani, and R. Hui, "Nearly degenerate four-wave mixing in distributed feedback semiconductor lasers operating above threshold," *IEEE J. Quantum Electron.*, vol. 29, pp. 1487–1493, 1993.
- [8] R. Hui, S. Benedetto, and I. Montrosset, "Optical frequency conversion using nearly degenerate four-wave mixing in a distributed-feedback semiconductor laser: Theory and experiment," *J. Lightwave Technol.*, vol. 11, pp. 2026–2031, 1993.
- [9] S. Murata, A. Tomita, J. Shimizu, H. Kitamura, and A. Suzuki, "Observation of highly nondegenerate four-wave mixing (>1 THz) in an InGaAsP multiple quantum well laser," *Appl. Phys. Lett.*, vol. 58, pp. 1458–1460, 1991.
- [10] H. Kuwatsuka, H. Shoji, M. Matsuda, and H. Ishikawa, "THz frequency conversion using nondegenerate four-wave mixing process in a lasing long-cavity  $\lambda/4$ -shifted DFB laser," *Electron. Lett.*, vol. 31, pp. 2108–2110, 1995.
- [11] J. Minch, C. S. Chang, and S. L. Chuang, "Four-wave mixing in a distributed feedback laser," *Appl. Phys. Lett.*, vol. 70, pp. 1360–1362, 1997.
- [12] H. Kogelnik and C. Shank, "Coupled-wave theory of distributed feedback lasers," *J. Appl. Phys.*, vol. 43, pp. 2327–2335, 1972.
- [13] T. Mukai and T. Saitoh, "Detuning characteristics and conversion efficiency of nearly degenerate four-wave mixing in a 1.5- $\mu$ m traveling-wave semiconductor laser amplifier," *IEEE J. Quantum Electron.*, vol. 26, pp. 865–875, 1990.
- [14] A. Mecozzi, S. Scotti, A. D'Ottani, E. Iannone, and P. Spano, "Four-wave mixing in traveling-wave semiconductor amplifiers," *IEEE J. Quantum Electron.*, vol. 31, pp. 689–699, 1995.
- [15] A. Uskov, J. Mork, and J. Mark, "Wave mixing in semiconductor laser amplifiers due to carrier heating and spectral-hole burning," *IEEE J. Quantum Electron.*, vol. 30, pp. 1769–1781, 1994.
- [16] J. Zhou, N. Park, J. Dawson, K. Vahala, M. Newkirk, and B. Miller, "Terahertz four-wave mixing spectroscopy for study of ultrafast dynamics in a semiconductor optical amplifier," *Appl. Phys. Lett.*, vol. 63, pp. 1179–1181, 1993.

- [17] J. Minch, C. S. Chang, W. Fang, S. L. Chuang, Y. K. Chen, and T. Tanbun-Ek, "Theory and experiment on the amplified spontaneous emission from a DFB laser," *IEEE J. Quantum Electron.*, vol. 33, pp. 815-823, May 1997.
- [18] B. W. Hakki and T. L. Paoli, "CW degradation at 300K of GaAs double-heterostructure junction lasers," *J. Appl. Phys.*, vol. 44, pp. 4113-4119, 1973.
- [19] ———, "Gain spectra in GaAs double-heterostructure injection lasers," *J. Appl. Phys.*, vol. 46, pp. 1299-1306, 1975.



**Jeffrey R. Minch** (S'96) was born in Schnectady, NY, in 1971. He received the B.S. degree in electrical engineering from Cornell University, Ithaca, NY, in 1993, the M.S. degree in electrical engineering from the University of Illinois at Urbana, in 1995, and is now working toward the Ph.D. degree there as well.

His research interests include quantum and optical electronic devices and nonlinear optics, particularly with an interest toward semiconductor lasers and wavelength conversion applications.



**Chih-Sheng Chang** (S'93-M'96) was born in Hualien, Taiwan, R.O.C., on November 3, 1964. He received the B.S. and M.S. degrees in electrical engineering from National Taiwan University, Taipei, Taiwan, R.O.C., in 1986 and 1990, respectively, and the Ph.D. degree from the Department of Electrical and Computer Engineering, University of Illinois at Urbana-Champaign in 1996.

He is currently a Post-Doctoral Research Associate in the Department of Electrical and Computer Engineering, University of Illinois at Urbana-Champaign. His research interests include strained quantum-well optoelectronic devices especially lasers and modulators, fiber sensors, and optical waveguides.



**Shun-Lien Chuang** (S'78-M'82-SM'88-F'97) received the B.S. degree in electrical engineering from National Taiwan University in 1976, and the M.S., E.E., and Ph.D. degrees in electrical engineering from the Massachusetts Institute of Technology in 1980, 1981, and 1983, respectively.

In 1983, he joined the Department of Electrical and Computer Engineering at the University of Illinois at Urbana-Champaign, where he is currently a Professor. He was a Resident Visitor at AT&T Bell Laboratories, Holmdel, NJ, in 1989. He was a consultant at Bellcore and Polaroid in 1991, and a Senior Visiting Professor (Sabbatical Chair) at SONY Research Center in 1995. He is conducting research on strained quantum-well semiconductor lasers, electroabsorption modulators, and femtosecond nonlinear optics. He was a Feature Editor for a special issue in *Journal of Optical Society of America B on Terahertz Generation, Physics and Applications* in 1994. He developed a graduate course on integrated optics and optoelectronics. He is the author of *Physics of Optoelectronic Devices*, (Wiley, Pure and Applied Optics Series, 1995). He has published more than 180 journal and conference papers.

He is a Fellow of the Optical Society of America and a member of the American Physical Society. He has been cited several times for Excellence in Teaching at the University of Illinois. He received the Andersen Consulting Award for excellence in advising in 1994 and was selected as an Associate at the Center for Advanced Study at the University of Illinois in 1995. He was also awarded a Fellowship from the Japan Society for the Promotion of Science to visit the University of Tokyo in 1996.

# Piezoelectric effects on electrical and optical properties of wurtzite GaN/AlGaIn quantum well lasers

Seoung-Hwan Park<sup>a)</sup> and Shun-Lien Chuang<sup>b)</sup>

Department of Electrical and Computer Engineering, University of Illinois at Urbana-Champaign,  
1406 West Green Street, Illinois 61801

(Received 23 January 1998; accepted for publication 11 April 1998)

The piezoelectric effects on the optical gain of wurtzite GaN/AlGaIn QW lasers taking into account the many-body effects are presented. The self-consistent model with piezoelectric field effect shows that band structures and optical gain are significantly affected by the piezoelectric field at relatively low carrier densities. The peak gain is redshifted and smaller when compared to the flat-band model without piezoelectric field effect. Only gain peaks corresponding to C1-HH1 and C1-LH1 transitions are observed in the investigated range and transitions for C1-HH2 and C1-LH2 are negligible due to the large subband energy spacing at low carrier densities and small matrix elements at high carrier densities. At high carrier densities, the self-consistent model shows band structures and optical properties similar to the flat-band model due to the screening effects. © 1998 American Institute of Physics. [S0003-6951(98)00924-3]

The wide-band-gap semiconductors including GaN, AlN, InN, and their ternary compounds have great potential for applications in high power and optoelectronic devices. Blue-green light-emitting diodes based on wurtzite GaN have already been demonstrated, and room-temperature continuous-wave operation of strained InGaIn/AlGaIn multi-quantum well (MQW) laser diodes with a lifetime of many hours has recently been reported.<sup>1</sup> With the current progress in these blue-green lasers, considerable efforts have been devoted to the calculation of the optical properties with many-body effects, because Coulomb interaction effects among carriers are expected to be important due to the large exciton binding energies in the wide-band-gap semiconductors.<sup>2-4</sup> Also, recent experimental studies show that III-V nitride heterostructures with the wurtzite crystal structure pseudomorphically grown in the (0001)-orientation have large strain-induced piezoelectric fields.<sup>5</sup> This internal field can greatly influence the optical properties,<sup>6</sup> and therefore the piezoelectric effect in addition to many-body effects should be taken into account for the design of high performance devices based on nitrides. However, most calculations of the electronic and optical properties for these wurtzite QW structures have been calculated mainly under the flat-band (FB) model.

In this letter, we report new results on the piezoelectric effect in wurtzite GaN/AlGaIn QW lasers taking into account many-body effects. Recently, Chow *et al.*<sup>3</sup> treated carrier-carrier (C-C) scattering effects on the optical gain at the level of quantum kinetic theory in the Markovian limit and showed that both diagonal and nondiagonal Coulomb correlations give rise to important modifications of the optical gain. Here, the line shape with only the diagonal C-C scattering contribution given by Asada<sup>7</sup> is used in calculating the optical gain as an approximation. However, the line shape function differs from a Lorentzian in that the broadening

factor  $\Gamma$  is given as a function of photon energy  $\hbar\omega$ . The band structure is determined based on a self-consistent (SC) solution.

We consider a GaN QW of a width  $L_z$  grown along the (0001) ( $z$ -axis) sandwiched between two  $\text{Al}_{0.3}\text{Ga}_{0.7}\text{N}$  barriers. The piezoelectric field of the barrier region is assumed to be zero. The valence band structure is calculated by using the block-diagonalized  $3 \times 3$  Hamiltonian<sup>8</sup> based on the  $\mathbf{k} \cdot \mathbf{p}$  method. The material parameters for GaN and AlN are taken from Ref. 8, except for those listed in Table I. The SC band structures and wave functions are obtained by iteratively solving the Schrödinger equation for electrons, the block-diagonalized  $3 \times 3$  Hamiltonian for holes, and Poisson's equation.<sup>9</sup> The total potential profiles for the electrons and holes are

$$\begin{aligned} V_c(z) &= V_{cw}(z) + |e|Fz - |e|\phi(z), \\ V_v(z) &= V_{vw}(z) + |e|Fz - |e|\phi(z), \end{aligned} \quad (1)$$

where  $V_{cw}(z)$  and  $V_{vw}(z)$  are the square-well potentials for the conduction band and valence band, respectively,  $F$  is the piezoelectric field, and  $\phi(z)$  is the screening potential in-

TABLE I. Parameters used for the calculations.

Parameter	GaN
Deformation potentials (eV)	
$D_1$	-1.70 <sup>a</sup>
$D_2$	6.30 <sup>a</sup>
$D_3$	8.00 <sup>a</sup>
$D_4$	-4.00 <sup>a</sup>
Dielectric constant(static) $\epsilon$	10.0 <sup>b</sup>
Elastic stiffness constants ( $\times 10^{11}$ dyn/cm <sup>2</sup> )	
$C_{11}$	39.0 <sup>c</sup>
$C_{12}$	14.5 <sup>c</sup>
Piezoelectric constant (cm/V) $d_{31}$	$-1.7 \times 10^{-10d}$

<sup>a</sup>Reference 14.

<sup>b</sup>Reference 15.

<sup>c</sup>Reference 16.

<sup>d</sup>Reference 5.

<sup>a)</sup>On leave from Department of Physics, Catholic University of Taegu-Hyosung, Hayang, Kyeongbuk, Korea.

<sup>b)</sup>Electronic mail: s-chuang@uiuc.edu

duced by the charged carriers, which satisfies Poisson's equation. The strain-induced piezoelectric field is given by<sup>10</sup>

$$F = \frac{2d_{31}}{\epsilon} \left( c_{11} + c_{12} - \frac{2c_{13}^2}{c_{33}} \right) \epsilon_{xx}, \quad (2)$$

where  $d_{31}$  is the piezoelectric constant,  $\epsilon$  is the static dielec-

tric constant,  $c_{ij}$  are the elastic stiffness constants, and  $\epsilon_{xx}$  is the in-plane component of the strain tensor. The wurtzite GaN is well known to have a large piezoelectric field along the (0001)-direction because it is polar along the  $c$ -axis.<sup>11</sup>

Using a spontaneous-emission transformation method<sup>12</sup> and a Padé approximation,<sup>2</sup> the optical gain  $g(\omega)$ , taking into account the many-body effects, is given by

$$g(\omega) = \left[ 1 - \exp\left(\frac{\hbar\omega - \Delta F}{kT}\right) \right] \sqrt{\frac{\mu_0}{\epsilon}} \left( \frac{e^2}{m_0^2 \omega} \right) \int_0^\infty dk_{\parallel} \frac{k_{\parallel}}{\pi L_z} |M_{lm}|^2 f_l^c(k_{\parallel}) [1 - f_m^v(k_{\parallel})] \\ \times \frac{\Gamma_{cv}(k_{\parallel}, \hbar\omega)}{[\Gamma_{cv}(k_{\parallel}, \hbar\omega)]^2 + (E_{lm}(k_{\parallel}) - \hbar\omega)^2} \frac{(1 - \text{Re } q_{k_{\parallel}}) + \text{Im } q_{k_{\parallel}} (E_{lm}(k_{\parallel}) - \hbar\omega) / (\Gamma_{cv}(k_{\parallel}, \hbar\omega))}{(1 - \text{Re } q_{k_{\parallel}})^2 + (\text{Im } q_{k_{\parallel}})^2}, \quad (3)$$

where  $\omega$  is the angular frequency,  $\mu_0$  is the vacuum permeability,  $\epsilon$  is the dielectric constant,  $k_{\parallel}$  is the in-plane wave vector,  $L_z$  is the well thickness,  $|M_{lm}|^2$  is the momentum matrix element<sup>13</sup> in the strained QW,  $f_l^c$  and  $f_m^v$  are the Fermi function for the conduction band states and the valence band states, and  $\hbar$  is Planck's constant. The indices  $l$  and  $m$  denote the electron states in the conduction band and the heavy hole (light hole) subband states in the valence band. Also,  $E_{lm}(k_{\parallel}) = E_l^c(k_{\parallel}) - E_m^v(k_{\parallel}) + E_g + \Delta E_{SX} + \Delta E_{CH}$  is the renormalized transition energy<sup>2</sup> between electrons and holes, where  $E_g$  is the band-gap of the material, and  $\Delta E_{SX}$  and  $\Delta E_{CH}$  are the screened exchange and Coulomb-hole contributions to the band-gap renormalization.  $q(k_{\parallel}, \hbar\omega)$  is the excitonic or Coulomb enhancement of the interband transition probability.<sup>2</sup> In the above,  $\Gamma_{cv}(k_{\parallel}, \hbar\omega) = \Gamma_{cl}(k_{\parallel}, \hbar\omega) + \Gamma_{vm}(k_{\parallel}, \hbar\omega)$ , where  $\Gamma_{cl}$  and  $\Gamma_{vm}$  are broadening factors related to the decay rate of the electron and hole wave functions. Here, only the hole-hole scattering is considered because it is dominant among the various processes such as the carrier-carrier and carrier-phonon scattering.<sup>7</sup>

Figure 1 shows the potential profiles and the wave functions (C1, HH1, and HH2) at zone center for the self-consistent model with the piezoelectric field of a 5 nm GaN/Al<sub>0.3</sub>Ga<sub>0.7</sub>N QW laser at (a)  $N = 2 \times 10^{19} \text{ cm}^{-3}$  and (b)  $N = 10 \times 10^{19} \text{ cm}^{-3}$ , respectively. The dotted line corresponds to potential profiles for the flat-band model without a piezoelectric field. The GaN QW is under 0.724% compressive strain and the strain-induced piezoelectric field is estimated to be about 1.33 MV/cm. This large field induces a spatial separation of the electron and hole wave functions and creates a screening electric field in the well to compensate the piezoelectric field. However, the SC model for relatively low carrier densities shows asymmetric electron and hole wave functions relative to the center of the well and is spatially separated as shown in Fig. 1(a), although there exists a large screening electric field in the well. Also, it is observed that the ground state transition energy C1-HH1 is redshifted compared to the FB model due to the quantum-confined Stark effect. For example, transition energies for the FB and SC models are 3.55 and 3.50 eV at  $N = 2 \times 10^{19} \text{ cm}^{-3}$ , respectively. On the other hand, as the

carrier density increases, the spatial separation of the electron and hole wave functions is gradually reduced. The SC model at  $N = 10 \times 10^{19} \text{ cm}^{-3}$  shows potential profiles and ground state transition energy C1-HH1 similar to the FB model. Thus, the piezoelectric effect on the electronic and optical properties is dominant in a range of relatively low carrier densities.

Figure 2 shows the valence band structures for the self-consistent model with the piezoelectric field of a 5 nm GaN/Al<sub>0.3</sub>Ga<sub>0.7</sub>N QW laser at (a)  $N = 2 \times 10^{19} \text{ cm}^{-3}$  and (b)  $N = 10 \times 10^{19} \text{ cm}^{-3}$ , respectively. The dotted line corresponds to the band structure for the flat-band model without piezoelectric field. The SC model at  $N = 2 \times 10^{19} \text{ cm}^{-3}$  shows a larger energy spacing between the first two subbands (HH1 and LH1) and higher subbands (HH2 and LH2) than those of the FB case. The increase of the subband energy spacing reduces the carrier population in the higher subbands. However, this effect is compensated by the decrease of the optical matrix element due to the spatial separation of the wave functions. The energy spacing decreases with increasing carrier density and the SC model shows band structures similar to those of the FB model at a carrier density of

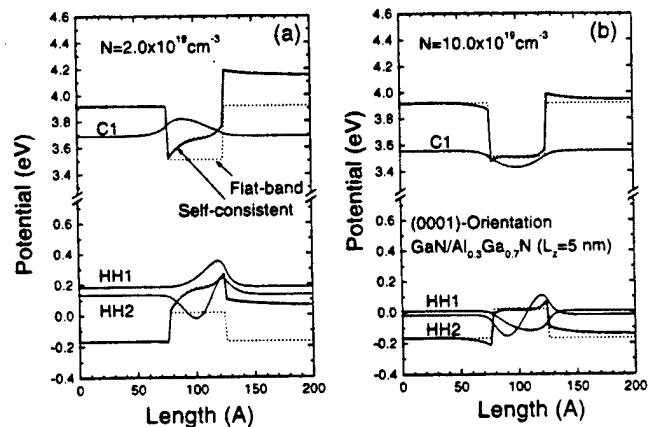


FIG. 1. The potential profiles and the wave functions (C1, HH1, and HH2) at zone center for the self-consistent model (solid line) with the piezoelectric field of a 5 nm GaN/Al<sub>0.3</sub>Ga<sub>0.7</sub>N QW laser at (a)  $N = 2 \times 10^{19} \text{ cm}^{-3}$  and (b)  $N = 10 \times 10^{19} \text{ cm}^{-3}$ , respectively. The dotted line corresponds to potential profiles for the flat-band model without a piezoelectric field.

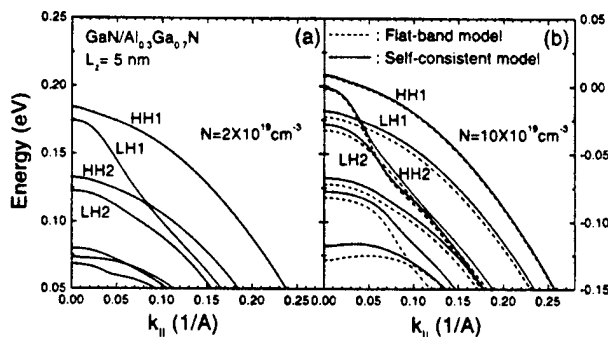


FIG. 2. The valence band structures for the self-consistent model with the piezoelectric field of a 5 nm GaN/Al<sub>0.3</sub>Ga<sub>0.7</sub>N QW laser at (a)  $N = 2 \times 10^{19} \text{ cm}^{-3}$  and (b)  $N = 10 \times 10^{19} \text{ cm}^{-3}$ , respectively. The dotted line corresponds to the band structure for the flat-band model without piezoelectric field.

$10 \times 10^{19} \text{ cm}^{-3}$ . This is due to the increase of the screening electric field to compensate the piezoelectric effect. In Fig. 3, we plot the normalized optical matrix element at zone center using the self-consistent model as a function of carrier density in a 5 nm GaN/Al<sub>0.3</sub>Ga<sub>0.7</sub>N QW laser. For comparison, using the flat-band model, we find that the normalized optical matrix elements at the zone center are 0.249 and 0.248 for C1-HH1 and C1-LH1, respectively, and zero for C1-HH2 and C1-LH2. In contrast, the SC model for C1-HH2 and C1-LH2 has matrix elements of a finite magnitude compared to zero for the FB model. Also, the matrix elements for C1-HH2 and C1-LH2 are larger than those of C1-HH1 and C1-LH1 at low carrier densities. However, transitions for C1-HH2 and C1-LH2 are reduced largely due to the increase of the subband energy spacing as shown in Fig. 2(a).

Figures 4(a) and 4(b) show the optical gain spectra and peak gain for FB and SC models as a function of carrier density in a 5 nm GaN/Al<sub>0.3</sub>Ga<sub>0.7</sub>N QW laser. The optical gain spectra in Fig. 4(a) for both cases have only one peak which corresponds to C1-HH1 and C1-LH1 transitions. The optical gain for C1-HH2 and C1-LH2 transitions is always smaller than that of the C1-HH1 and C1-LH1 transitions because of the large subband energy spacing at low carrier densities and small matrix elements at high carrier densities.

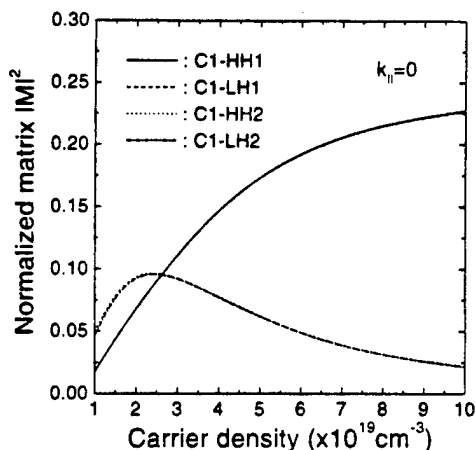


FIG. 3. The normalized optical matrix element at zone center using the self-consistent model as a function of the carrier density in a 5 nm GaN/Al<sub>0.3</sub>Ga<sub>0.7</sub>N QW laser. C1-HH1 and C1-LH1 are on top of each other, so are C1-HH2 and C1-LH2.

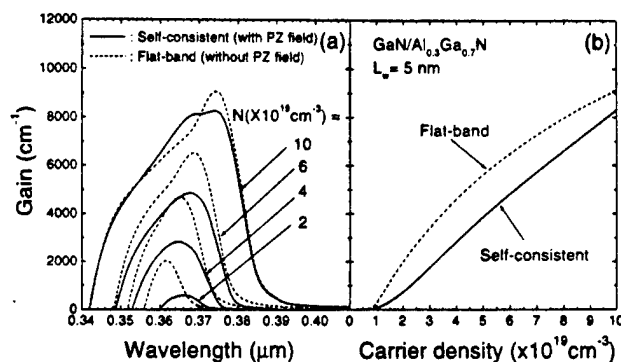


FIG. 4. The optical gain spectra (a) and peak gains (b) for FB and SC models as a function of carrier density in a 5 nm GaN/Al<sub>0.3</sub>Ga<sub>0.7</sub>N QW laser.

The peak gain for the SC model at low carrier densities is redshifted compared with the FB model.

On the other hand, the peak wavelength for the SC calculation approaches that of the FB model with increasing carrier density. This is due to the increase of the screening electric field with carrier density. As the carrier density increases, the peak gain in Fig. 4(b) for the SC case increases linearly while that of the FB case (dashed line) saturates gradually. Thus, it is expected that peak gains for both models coincide with each other at a high carrier density. The SC model predicts a larger threshold carrier density than that estimated by the FB model in the investigated range.

In summary, the piezoelectric effect on the optical gain of wurtzite GaN/AlGaIn QW lasers taking into account the many-body effects is presented. Our calculations show that the piezoelectric effect on the electronic and optical properties plays an important role up to a carrier density of  $10 \times 10^{19} \text{ cm}^{-3}$ .

This work was supported by ONR Grant No. N00014-96-1-0303. One of the authors (S.H.P.) was supported by Catholic University of Taegu-Hyosung.

- <sup>1</sup> S. Nakamura, IEEE J. Sel. Top. Quantum Electron. **3**, 712 (1997).
- <sup>2</sup> W. W. Chow, S. W. Koch, and M. Sargent III, *Semiconductor-Laser Physics* (Springer, Berlin, 1994).
- <sup>3</sup> W. W. Chow, P. M. Smowton, P. Blood, A. Girmdt, F. Jahnke, and S. W. Koch, Appl. Phys. Lett. **71**, 157 (1997).
- <sup>4</sup> S. H. Park and S. L. Chuang, Appl. Phys. Lett. **72**, 287 (1998).
- <sup>5</sup> G. Martin, A. Botchkarev, A. Rockett, and H. Morkoç, Appl. Phys. Lett. **68**, 2541 (1996).
- <sup>6</sup> J. Wang, J. B. Jeon, Yu. M. Sirenko, and K. W. Kim, IEEE Photonics Technol. Lett. **9**, 728 (1997).
- <sup>7</sup> M. Asada, in *Quantum Well Lasers*, edited by P. S. Zory (Academic, New York, 1993), Chap. 2.
- <sup>8</sup> S. L. Chuang and C. S. Chang, Semicond. Sci. Technol. **12**, 252 (1997).
- <sup>9</sup> S. L. Chuang, *Physics of Optoelectronic Devices* (Wiley, New York, 1995), Chap. 4.
- <sup>10</sup> A. Bykhovski, B. Gelmont, and S. Shur, J. Appl. Phys. **74**, 6734 (1993).
- <sup>11</sup> B. R. Nag, *Electron Transport in Compound Semiconductors*, Springer Series Vol. 11 (Springer, New York, 1980), Chap. 1.
- <sup>12</sup> S. L. Chuang, J. O'Gorman, and A. F. Levi, IEEE J. Quantum Electron. **29**, 1631 (1993).
- <sup>13</sup> S. L. Chuang, IEEE J. Quantum Electron. **32**, 1791 (1996).
- <sup>14</sup> M. Kumagai, S. L. Chuang and H. Ando, Phys. Rev. B (to be published).
- <sup>15</sup> V. W. L. Chin, T. L. Tansley, and T. Osotchan, J. Appl. Phys. **75**, 7365 (1994).
- <sup>16</sup> A. Polian, M. Grimsditch, and I. Grzegory, J. Appl. Phys. **79**, 3343 (1996).

# Optical Gain of Strained Wurtzite GaN Quantum-Well Lasers

Shun Lien Chuang, Senior Member, IEEE

**Abstract**—A theory for the electronic band structure and the free-carrier optical gain of wurtzite-strained quantum-well lasers is presented. We take into account the strain-induced band-edge shifts and the realistic band structures of the GaN wurtzite crystals. The effective-mass Hamiltonian, the basis functions, the valence band structures, the interband momentum matrix elements, and the optical gain are presented with analytical expressions and numerical results for GaN–AlGa<sub>x</sub>N strained quantum-well lasers. This theoretical model provides a foundation for investigating the electronic and optical properties of wurtzite-strained quantum-well lasers.

## I. INTRODUCTION

RECENTLY, wurtzite-strained quantum wells have been studied intensively in an effort to realize GaN blue-green lasers. With the current progress in II–VI and III–V blue-green lasers [1], [2], theoretical models for the electronic and optical properties of these quantum-well (QW) structures become very important. Although optically pumped stimulated emission from GaN was first observed more than 25 years ago [3] and many researchers have been intensively working on the electrical injection laser diodes, stimulated emission [4] and laser action [2] by current injection have only recently been achieved.

There have been more reports on the experimental data and theoretical models of zinc-blende compounds than those for the wurtzite semiconductors. Therefore, wurtzite semiconductor band structures and optical properties are less understood, and many band-structure parameters are not available. Furthermore, a GaN layer is usually grown on AlGa<sub>x</sub>N barrier and cladding layers, which are grown on a sapphire substrate. A significant amount of lattice mismatch between the substrate and the AlGa<sub>x</sub>N layer results in a large dislocation or defect density. The defect density may broaden the gain spectrum and can be simply accounted for in the linewidth broadening parameter. Strain also exists in the GaN–AlGa<sub>x</sub>N layers. As shown in Fig. 1 and Table I, the lattice constant of GaN is 3.1892 Å and that of AlN is 3.112 Å [5], [6]. The corresponding bandgap energies for Al<sub>x</sub>Ga<sub>1-x</sub>N and In<sub>1-x</sub>Ga<sub>x</sub>N ternary compounds with bowing effects as a function of the lattice constant are shown as solid curves. The band gap of Al<sub>x</sub>In<sub>1-x</sub>N and its bowing parameter are less understood. From the only available data [7], there seems to be a significant

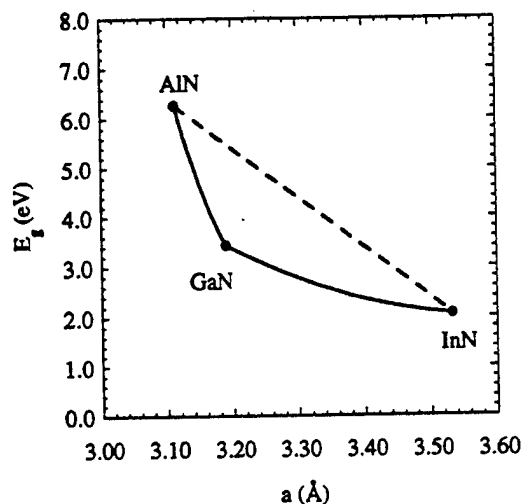


Fig. 1. Bandgap energy of GaN, AlN, InN, and their ternary compounds or possible quaternary compounds as a function of the lattice constants. The bowing effects for the AlGa<sub>x</sub>N and InGa<sub>x</sub>N are included in the plot of the bandgap energies (solid curves). Because not enough experimental data for the ternary AlIn<sub>x</sub>N compounds are available, a dashed line is shown for illustration.

amount of bowing effects. We use a dashed line to show the possible range of band gap and lattice constant. We would expect that a quaternary compound using AlInGa<sub>x</sub>N will have its band gap and lattice constant within the triangular area in Fig. 1. This means that, in general, various amounts of tensile and compressive strains are possible using different combinations of ternary and quaternary compounds in the wells and barriers. However, many band-structure parameters such as the conduction-band and valence-band deformation potentials and the valence-band effective-mass parameters are either absent or cannot be measured because of a lack of high-quality pseudomorphically strained QW samples.

Previously, the effective-mass Hamiltonian for wurtzite crystals was derived using an invariant method [8]–[10]. The necessary band-structure parameters to describe the heavy-hole (HH), light-hole (LH), and crystal-field split-hole (CH) bands have only been recently obtained by fitting the band structure of the effective-mass Hamiltonian to that of a first-principles calculation [11] and then applied to the calculations of QW band structure and optical gain [12], [13]. We have recently derived the effective-mass Hamiltonian based on the  $k \cdot p$  method [14] and defined important band-structure parameters in a similar way as those defined using the Luttinger–Kohn method [15] for the zinc-blende crystals. Our model is attractive since the Hamiltonian of a wurtzite-strained

Manuscript received March 22, 1996; revised June 18, 1996. This work was supported by the U.S. Office of Naval Research under Grant N00014-96-1-0303 and the Center for Advanced Study at the University of Illinois.

The author is with the Department of Electrical and Computer Engineering, University of Illinois at Urbana-Champaign, Urbana, IL 61801 USA.

Publisher Item Identifier S 0018-9197(96)07286-7.

TABLE I  
THE MATERIAL PARAMETERS

Parameter	GaN	AlN
Lattice constants <sup>a-b</sup> (Å)		
a	3.1892	3.112
c	5.1850	4.982
Energy parameters <sup>a-f</sup>		
$E_g$ (eV) at 300K	3.44	6.28
$\Delta_1 = \Delta_{\sigma}$ (meV)	16 <sup>f</sup> (22°)	-58.5°
$\Delta_{so}$ (meV)	12 <sup>f</sup> (11°)	
$\Delta_2 = \Delta_3 = \Delta_{so}/3$ (meV)	4	6.80°
Conduction-band effective masses <sup>e</sup>		
$m_e^*/m_0$	0.20	0.33
$m_c^*/m_0$	0.18	0.25
Valence-band effective-mass parameters <sup>e</sup>		
$A_1$	-6.56	-3.95
$A_2$	-0.91	-0.27
$A_3$	5.65	3.68
$A_4$	-2.83	-1.84
$A_5$	-3.13	-1.95
$A_6$	-4.86	-2.91
Deformation potentials (eV)		
a (Interband)	-8.16 <sup>d</sup>	
$a_c = 0.5a$	-4.08 <sup>f</sup>	
$D_1$	0.7 <sup>f</sup>	
$D_2$	2.1 <sup>f</sup>	
$D_3$	1.4 <sup>f</sup>	
$D_4$	-0.7 <sup>f</sup>	
Elastic stiffness constants <sup>a-b</sup> (10 <sup>11</sup> dyn/cm <sup>2</sup> )		
$C_{13}$	15.8	12.0
$C_{33}$	26.7	39.5

\*The linear interpolation formula  $P(\text{Al}_x\text{Ga}_{1-x}\text{N}) = xP(\text{AlN}) + (1-x)P(\text{GaN})$  is used for most of the parameters for  $\text{Al}_x\text{Ga}_{1-x}\text{N}$  barriers except for the bandgap energy, which has a bowing parameter [5] of 0.98 eV.  $E_g(\text{Al}_x\text{Ga}_{1-x}\text{N})(\text{eV}) = x(\text{AlN}) + (1-x)e_g(\text{GaN}) - 0.98x(1-x)$ .  
<sup>a</sup> [5], <sup>b</sup> [6], <sup>c</sup> [33], <sup>d</sup> [27], <sup>e</sup> [11], <sup>f</sup> [14].

semiconductor resembles that of a zinc-blende semiconductor [16]–[18], except that different energy-splitting parameters and basis functions are necessary. The six-by-six Hamiltonian can also be diagonalized [19] in a similar fashion as that for a zinc-blende structure.

The optical gain spectrum for a strained zinc-blende QW laser was first calculated using a four-by-four Hamiltonian [17], [20] ignoring spin-orbit coupling and then using a six-by-six Hamiltonian including the spin-orbit coupling [18]. It has been shown [21] recently that our theoretical results for the optical gain, the refractive index, and the linewidth-enhancement factor spectra of long-wavelength (1.55  $\mu\text{m}$ ) semiconductor lasers agree very well with our experimental data.

In this paper, we present new results including analytical expressions for the interband momentum matrix elements and

numerical results for the optical gain of strained wurtzite QW lasers. The Hamiltonian is taken from a block-diagonalized Hamiltonian consisting of two three-by-three matrices, which we have recently derived [19]. A  $\text{GaN-Al}_x\text{Ga}_{1-x}\text{N}$  strained QW structure is considered in our model calculations. We present the formulation of the free-carrier theory for the optical gain of a strained QW structure in Section II. The theory for electronic properties, such as the conduction-band and valence-band structures, the strain-induced band-edge shifts, and the model for a wurtzite QW heterostructure, is then presented in Section III. We then show in Section IV analytical expressions for the interband momentum-matrix elements and the final expressions for the optical spontaneous emission spectrum, which is used to calculate the optical gain coefficient. Numerical results for  $\text{GaN-Al}_x\text{Ga}_{1-x}\text{N}$  strained QW lasers are then presented in Section V. The conclusions are given in Section VI.

## II. GENERAL FORMULATION OF THE OPTICAL GAIN SPECTRUM

In this section, we present the general formula for the optical gain of a strained QW laser in terms of the electronic properties such as the conduction band and the valence band energies and the interband transition matrix elements. The optical material gain coefficient of a quantum well can be calculated either from Fermi's golden rule [17], including a Lorentzian line-shape function or calculated from the spontaneous emission spectrum [17], [21], [22] using a fundamental relation between the spontaneous emission and gain spectra. Both methods are essentially the same. However, we adopt the latter because it gives more physical results below the band gap than the former model and the optical gain has a transparent energy at the quasi-Fermi level separation. The spontaneous emission rate per unit volume per energy interval at an optical energy  $\hbar\omega$  is given by [21], [22]

$$r_{sp}^e(\hbar\omega) = \frac{n_r^2 \omega^2}{\pi^2 \hbar c^2} g_{sp}^e(\hbar\omega) \quad (1)$$

$$g_{sp}^e(\hbar\omega) = \frac{q^2 \pi}{n_r c \epsilon_0 m_0^2 \omega L_z} \sum_{\eta=\uparrow, \downarrow} \sum_{\sigma=U, L} \sum_{n, m} \times \int \frac{k_t dk_t}{2\pi} \int \frac{d\phi}{2\pi} |\hat{e} \cdot \mathbf{M}_{nm}^{\eta\sigma}(k_t)|^2 \times \frac{f_n^c(k_t)(1 - f_{\sigma m}^v(k_t))(\hbar\gamma/\pi)}{(E_{\sigma, nm}^{cv}(k_t) - \hbar\omega)^2 + (\hbar\gamma)^2} \quad (2)$$

where  $q$  is the magnitude of the electron charge,  $m_0$  is the electron rest mass in free space,  $c$  and  $\epsilon_0$  are the velocity of light and permittivity in free space, respectively,  $\eta$  is the electron spin, which can be either  $\uparrow$  or  $\downarrow$ ,  $\hat{e}$  is the polarization vector of the optical electric field,  $n_r$  and  $L_z$  are the refractive index and well width of the quantum well, and  $\hbar\gamma$  is the half linewidth of the Lorentzian function ( $\gamma = (0.1 \text{ ps})^{-1}$  is used in this paper for simplicity).  $\mathbf{M}_{nm}^{\eta\sigma}(k_t) = \langle \Psi_{m, k_t}^{v\sigma} | \mathbf{p} | \Psi_{n, k_t}^{c\eta} \rangle$  is the momentum matrix element for transitions between the conduction-band state  $\Psi_{n, k_t}^{c\eta}(z)$  and the valence-band state  $\Psi_{m, k_t}^{v\sigma}(z)$ , and  $\mathbf{p}$  is the momentum operator. For convenience,  $g_{sp}^e(\hbar\omega)$  is defined to have the same dimension (1/cm) as the

material gain coefficient. The expression

$$E_{\sigma,nm}^{cv}(k_t) = E_n^c(k_t) - E_{\sigma,m}^v(k_t) \quad (3)$$

is the interband energy of the conduction band and the valence band. The Fermi-Dirac distributions for the electrons in the conduction and valence bands are

$$f_n^c(k_t) = \frac{1}{1 + \exp\left(\frac{E_n^c(k_t) - F_c}{k_B T}\right)} \quad (4)$$

$$f_{\sigma m}^v(k_t) = \frac{1}{1 + \exp\left(\frac{E_{\sigma,m}^v(k_t) - F_v}{k_B T}\right)} \quad (5)$$

where  $F_c$  and  $F_v$  are the quasi-Fermi levels for electrons and holes.

The material gain can be determined from the spontaneous emission rate [21], [22] using

$$g(\hbar\omega) = g_{sp}^e(\hbar\omega) \left[ 1 - \exp\left(\frac{\hbar\omega - \Delta F}{k_B T}\right) \right] \quad (6)$$

for  $e = \text{TE}$  ( $=x$  or  $y$ , which is perpendicular to the  $c$  axis) or  $e = \text{TM}$  ( $=z$ , which is parallel to the  $c$  axis) polarization. The modal gain  $g_M = \Gamma g$  is obtained by multiplying the material gain by the optical confinement factor  $\Gamma$ . The separation of the quasi-Fermi levels,  $\Delta F$ , depends on the injected carrier densities

$$\Delta F = F_c - F_v. \quad (7)$$

The quasi-Fermi levels will be discussed in Section IV.

### III. THE ELECTRONIC BAND STRUCTURES AND WAVE FUNCTIONS

Consider a strained GaN-layer wurtzite crystal pseudomorphically grown along the  $c$  axis ( $z$  axis) on a thick  $\text{Al}_x\text{Ga}_{1-x}\text{N}$  layer. The strain tensor  $\bar{\epsilon}$  in the well region has the following elements:

$$\begin{aligned} \epsilon_{xx} &= \epsilon_{yy} = \frac{a_0 - a}{a} \\ \epsilon_{zz} &= -\frac{2C_{13}}{C_{33}} \epsilon_{xx} \\ \epsilon_{xy} &= \epsilon_{yz} = \epsilon_{zx} = 0 \end{aligned} \quad (8)$$

where  $a_0$  and  $a$  are the lattice constants of the  $\text{Al}_x\text{Ga}_{1-x}\text{N}$  barrier and the GaN well layers, respectively.  $C_{13}$  and  $C_{33}$  are the stiffness constants of the GaN well layer. The general strain-stress relation for the hexagonal crystal can be found in [23].

The conduction bands can be characterized by a parabolic-band model, and the effective-mass Hamiltonian can be written as

$$H^c(\mathbf{k}_t, k_z) = \left( \frac{\hbar^2}{2} \right) \left( \frac{k_t^2}{m_t^*} + \frac{k_z^2}{m_z^*} \right) + E_c^0(z) + P_{ce}(z) \quad (9)$$

where the wave vector  $\mathbf{k}_t = -i\nabla_t$ ,  $k_z = -i\partial/\partial z$ , and  $m_t^*$  and  $m_z^*$  are the electron effective masses perpendicular ( $t$ ) and parallel ( $z$ ) to the growth direction, respectively. The hydrostatic energy shift in the conduction band,  $P_{ce}(z)$ , is zero

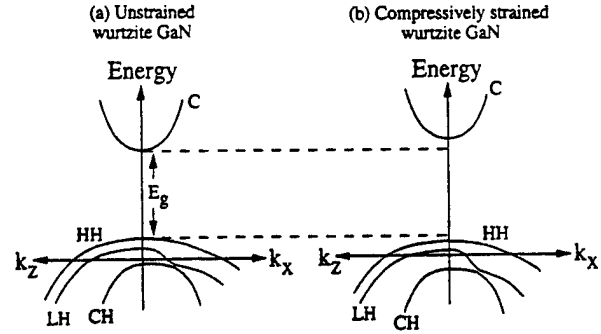


Fig. 2. Schematic diagram showing the bulk band structures of (a) an unstrained GaN wurtzite semiconductor and (b) a compressively strained GaN layer.

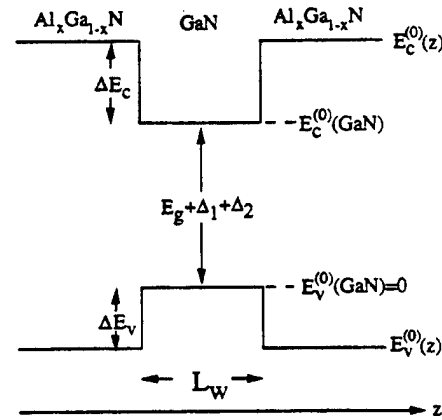


Fig. 3. The conduction- and valence-band energy profiles of a  $\text{GaN-Al}_{0.3}\text{Ga}_{0.7}\text{N}$  quantum well with a well width  $L_w$  before adding the strain-induced band-edge shifts. The reference energy is chosen to be  $E_v^0$  of an unstrained GaN material.

in the barrier regions and is due to a compressive strain in the well region

$$P_{ce} = a_{cz}\epsilon_{zz} + a_{ct}(\epsilon_{xx} + \epsilon_{yy}) \quad (10)$$

where  $a_{cz}$  and  $a_{ct}$  are the conduction-band deformation potentials along the  $c$  axis and perpendicular to the  $c$  axis, respectively. We take  $a_{cz} = a_{ct}(=a_c)$  for simplicity and assume a value of  $-4.08$  eV from a recent fit [14] to the available experimental data. Since the interband deformation potential is negative, the band gap increases with an increasing compressive strain, as shown in Fig. 2. The conduction-band edge is shifted upward for compressive strain, as in a thin GaN layer sandwiched between two thick AlGaN layers.  $E_c^0(z)$  in (9) is the QW potential profile of the *unstrained* conduction-band edge and is given by  $E_c^0(z) = E_c^0(\text{GaN})$  for  $z$  in the well, and  $= E_c^0(\text{Al}_x\text{Ga}_{1-x}\text{N})$  for  $z$  in the barrier, as shown in Fig. 3. We choose the reference energy at  $E_v^0(\text{GaN}) = 0$ , which is the band edge of the CH band of an unstrained wurtzite GaN before including the spin-orbit interaction [14],  $E_v^0 = \langle z|H_0|z \rangle$ . Note that the heavy-hole, light-hole, and conduction-band edges are referenced to the same energy value,  $E_v^0(\text{GaN})$ , following the convention for the wurtzite structure. In this convention,  $E_c^0(\text{GaN}) - E_v^0(\text{GaN}) = E_g + \Delta_1 + \Delta_2$ .

The wave function of the  $n$ th conduction subband can be written as

$$\Psi_{n,k_t}^{c\eta}(z) = \frac{e^{i\mathbf{k}_t \cdot \mathbf{r}_t}}{\sqrt{A}} \phi_n(z) |S, \eta\rangle \quad (11)$$

where  $\mathbf{k}_t$  is the transverse wave vector,  $\mathbf{r}_t$  is the two-dimensional position vector and  $A$  is the area of the quantum well in the  $x$ - $y$  plane,  $\phi_n(z)$  is the envelope function for the  $z$ -dependent part of the  $n$ th conduction subband, and  $\eta$  is the electron spin ( $\uparrow$  or  $\downarrow$ ).

The conduction-band-edge energy  $E_n^c = E_n^c(k_t = 0)$  is determined by solving the effective-mass equation for electrons

$$H^c(k_t = 0, k_z = -i\partial/\partial z)\phi_n(z) = E_n^c\phi_n(z) \quad (12)$$

with the envelope function normalized as

$$\int dz |\phi_n(z)|^2 = 1. \quad (13)$$

We use

$$E_n^c(k_t) \approx E_n^c(k_t = 0) + \frac{\hbar^2 k_t^2}{2m_{e,w}^*} \quad (14)$$

to obtain the conduction-band structure, where  $m_{e,w}^*$  is the electron effective mass in the well region parallel to the quantum well.

The bulk valence-band structure can be determined by finding the eigenvalues of

$$\det[H_{ij}^v(\mathbf{k}) - \delta_{ij}E^v(\mathbf{k})] = 0 \quad (15)$$

where  $\mathbf{k}$  is a real wave vector and the envelope functions are plane waves with the same wave vector  $\mathbf{k}$ . The Hamiltonian for the valence-band structure has been derived recently by the  $\mathbf{k} \cdot \mathbf{p}$  method [14], and the matrix elements are defined consistently using our chosen basis functions. We found that the six-by-six Hamiltonian can be block-diagonalized using a unitary transformation [19]

$$H_{6 \times 6}^v(\mathbf{k}) = \begin{bmatrix} H_{3 \times 3}^U(\mathbf{k}) & 0 \\ 0 & H_{3 \times 3}^L(\mathbf{k}) \end{bmatrix} \quad (16)$$

where  $H_{3 \times 3}^U$  and  $H_{3 \times 3}^L$  are three-by-three matrices defined as

$$H^U = \begin{bmatrix} F & K_t & -iH_t \\ K_t & G & \Delta - iH_t \\ iH_t & \Delta + iH_t & \lambda \end{bmatrix} \\ H^L = \begin{bmatrix} F & K_t & iH_t \\ K_t & G & \Delta + iH_t \\ -iH_t & \Delta - iH_t & \lambda \end{bmatrix}. \quad (17)$$

Note that the relations hold:  $H^U = (H^L)^* = (H^L)^t$  and the reference energy,  $E_v^0$ , which should appear in all the diagonal terms of the matrices, has been set to zero for a bulk semiconductor. The matrix elements contain the general expressions for a strained wurtzite semiconductor

$$F = \Delta_1 + \Delta_2 + \lambda + \theta$$

$$G = \Delta_1 - \Delta_2 + \lambda + \theta$$

$$\lambda = \lambda_k + \lambda_e$$

$$\lambda_k = \frac{\hbar^2}{2m_0} (A_1 k_z^2 + A_2 k_t^2)$$

$$\lambda_e = D_1 \epsilon_{zz} + D_2 (\epsilon_{xx} + \epsilon_{yy})$$

$$\theta = \theta_k + \theta_e$$

$$\theta_k = \frac{\hbar^2}{2m_0} (A_3 k_z^2 + A_4 k_t^2)$$

$$\theta_e = D_3 \epsilon_{zz} + D_4 (\epsilon_{xx} + \epsilon_{yy})$$

$$K_t = \frac{\hbar^2}{2m_0} A_5 k_t^2$$

$$H_t = \frac{\hbar^2}{2m_0} A_6 k_t k_z$$

$$\Delta = \sqrt{2}\Delta_3 \quad (18)$$

where  $k_t = \sqrt{k_x^2 + k_y^2}$  is the magnitude of the wave vector in the  $k_x$ - $k_y$  plane. Note that the bases for the Hamiltonian  $H_{6 \times 6}^v$  in (16) are defined as

$$|1\rangle = \alpha^* |Y_{11} \uparrow\rangle + \alpha |Y_{1-1} \downarrow\rangle$$

$$|2\rangle = \beta |Y_{1-1} \uparrow\rangle + \beta^* |Y_{11} \downarrow\rangle$$

$$|3\rangle = \beta^* |Y_{10} \uparrow\rangle + \beta |Y_{10} \downarrow\rangle$$

$$|4\rangle = \alpha^* |Y_{11} \uparrow\rangle - \alpha |Y_{1-1} \downarrow\rangle$$

$$|5\rangle = \beta |Y_{1-1} \uparrow\rangle - \beta^* |Y_{11} \downarrow\rangle$$

$$|6\rangle = -\beta^* |Y_{10} \uparrow\rangle + \beta |Y_{10} \downarrow\rangle$$

$$Y_{11} = \frac{-1}{\sqrt{2}} |X + iY\rangle$$

$$Y_{10} = |Z\rangle$$

$$Y_{1-1} = \frac{1}{\sqrt{2}} |X - iY\rangle. \quad (19)$$

where

$$\alpha = \frac{1}{\sqrt{2}} e^{i(\frac{3\pi}{4} + \frac{3\phi}{2})}, \quad \beta = \frac{1}{\sqrt{2}} e^{i(\frac{\pi}{4} + \frac{\phi}{2})} \quad (20)$$

and  $\phi = \tan^{-1}(k_x/k_y)$  is the azimuthal angle in the  $k_x$ - $k_y$  plane and covers a range between 0 and  $2\pi$ . The wave functions  $Y_{lm}(l = 1, m = -1, 0, 1)$  in (19) are the spherical harmonics of the  $p$  state of hydrogen atom [17] in cartesian coordinates following the phase convention of [24]. The  $A_i$ s are the band-structure parameters, which play the same role as the Luttinger parameters,  $\gamma_1, \gamma_2$ , and  $\gamma_3$ , of zinc-blende crystals.  $\Delta_1$  is the crystal-field split energy and is caused by the anisotropy of the wurtzite symmetry. It is the difference between the eigenvalues of the unperturbed Hamiltonian,  $H_0$ , of the  $X$ -like (or  $Y$ -like) states and the  $Z$ -like states before the spin-orbit coupling effect is included,  $\langle X|H_0|X\rangle = \langle Y|H_0|Y\rangle = E_v + \Delta_1$ , and  $\langle Z|H_0|Z\rangle = E_v$ .  $E_v$  is the reference energy.  $\Delta_2$  and  $\Delta_3$  account for spin-orbit interactions. It should be pointed out that under the cubic approximation [8], [11], the following relations hold among the parameters  $A_i$ s and  $\Delta_i$ s:

$$A_1 - A_2 = -A_3 = 2A_4, \quad A_3 + 4A_5 = \sqrt{2}A_6 \\ D_1 - D_2 = -D_3 = 2D_4, \quad \Delta_2 = \Delta_3. \quad (21)$$

Therefore, five band-structure parameters such as  $A_1, A_2, A_5, \Delta_1$ , and  $\Delta_2$ , plus two deformation potentials  $D_1$

and  $D_2$ , are necessary for the calculation of the valence-band structures. Sometimes, the spin-orbit split energy  $\Delta_{so} = 3\Delta_2 = 3\Delta_3$  is used.

For a QW structure, the corresponding material parameters in the barrier and the well regions have to be used in the Hamiltonian. The band-edge discontinuities have to be added properly in the effective-mass equation. The hole wave function in a quantum well can be written as

$$\Psi_m^U(z; k_t) = \frac{e^{i\mathbf{k}_t \cdot \mathbf{r}_t}}{\sqrt{A}} (g_m^{(1)}(z; k_t)|1\rangle + g_m^{(2)}(z; k_t)|2\rangle + g_m^{(3)}(z; k_t)|3\rangle) \quad (22)$$

$$\Psi_m^L(z; k_t) = \frac{e^{i\mathbf{k}_t \cdot \mathbf{r}_t}}{\sqrt{A}} (g_m^{(4)}(z; k_t)|4\rangle + g_m^{(5)}(z; k_t)|5\rangle + g_m^{(6)}(z; k_t)|6\rangle) \quad (23)$$

where  $g_m^{(i)}$ ,  $i = 1, 2, \dots, 6$  are the envelope functions of the  $m$ th valence subbands, which follow the normalization rules

$$\sum_{i=1}^3 \int dz |g_m^{(i)}(z; k_t)|^2 = 1, \quad \sum_{i=4}^6 \int dz |g_m^{(i)}(z; k_t)|^2 = 1. \quad (24)$$

The valence subband structure for the upper Hamiltonian  $E_m^U(k_t)$  can be determined by solving

$$\sum_{j=1}^3 \left( H_{ij}^U \left( k_z = -i \frac{\partial}{\partial z} \right) + \delta_{ij} E_v^0(z) \right) g_m^{(j)}(z; k_t) = E_m^U(k_t) g_m^{(i)}(z; k_t) \quad (25)$$

for  $i = 1, 2, 3$ . Similarly, the band structure for the lower Hamiltonian,  $E_m^L(k_t)$ , can be obtained using  $H_{ij}^L + \delta_{ij} E_v^0(z)$ .  $E_v^0(z)$  is the QW potential profile of the *unstrained* valence-band reference energy, and is given by  $E_v^0(z) = E_v^0(\text{GaN})$  for  $z$  in the well, and  $= E_v^0(\text{Al}_x\text{Ga}_{1-x}\text{N})$  for  $z$  in the barrier. We choose the reference energy at  $E_v^0(\text{GaN}) = 0$ . The band-edge discontinuity for the valence band is  $\Delta E_v^0 = Q_v \Delta E_g$  where  $\Delta E_g$  is the bandgap difference between the unstrained  $\text{Al}_x\text{Ga}_{1-x}\text{N}$  and GaN. The partition ratio is assumed to be  $Q_v = 0.33$  for the valence band, which follows the experimental results for the GaN-AlN heterojunction [25]. Thus, we have the QW potential  $E_v^0(z) = 0$  in the well, and  $E_v^0(z) = -Q_v \Delta E_g$  in the barriers. The bandgap energy of  $\text{Al}_x\text{Ga}_{1-x}\text{N}$  has a bowing parameter  $b = 0.98$  eV and is given in Table I together with other material parameters, which are linearly interpolated from the corresponding GaN and AlN binary wurtzite semiconductors. Note that the strain-induced band edge shifts are taken into account in the diagonal terms of the Hamiltonian matrices.

Since  $H^U$  and  $H^L$  differ only by a change of signs in front of all the terms with a single derivative with respect to  $z$  (i.e.,  $\partial/\partial z$  in  $H_t$ ), it is easy to see that for a quantum well with a reflection symmetry  $E_v^0(z) = E_v^0(-z)$ , the upper and lower Hamiltonians have the same valence-band structures,  $E_m^U(k_t) = E_m^L(k_t)$ , and the wave functions are related by  $g_m^{(1)}(z; k_t) = g_m^{(4)}(-z; k_t)$ ,  $g_m^{(2)}(z; k_t) = g_m^{(5)}(-z; k_t)$ , and  $g_m^{(3)}(z; k_t) = g_m^{(6)}(-z; k_t)$ . At the zone center ( $k_t = 0$ ), the HH subbands are decoupled from the LH and CH subbands,

while there is always a coupling between the LH and CH bands.

#### IV. INTERBAND MOMENTUM-MATRIX ELEMENTS FOR GAIN AND SPONTANEOUS EMISSION SPECTRA

Using the expressions for the basis  $|u_i^e\rangle$  in (19), we obtain

$$|\hat{x} \cdot \mathbf{M}_{nm}^U(k_t)|^2 = \frac{|\langle S|p_x|X\rangle|^2}{4} \left\{ \langle \phi_n | g_m^{(1)} \rangle^2 + \langle \phi_n | g_m^{(2)} \rangle^2 + 2 \cos(2\phi) \langle \phi_n | g_m^{(1)} \rangle \langle \phi_n | g_m^{(2)} \rangle \right\} \quad (26)$$

for  $\eta = \text{both } \uparrow \text{ and } \downarrow$ , where we have used the following momentum matrix elements from the basis functions:

TE( $\hat{e} = \hat{x}$ ) polarization

$$\begin{aligned} \langle S \uparrow | p_x | 1 \rangle &= -\frac{\alpha^*}{\sqrt{2}} \langle S | p_x | X \rangle \\ \langle S \uparrow | p_x | 2 \rangle &= \frac{\beta}{\sqrt{2}} \langle S | p_x | X \rangle \\ \langle S \uparrow | p_x | 3 \rangle &= 0 \\ \langle S \uparrow | p_x | 4 \rangle &= -\frac{\alpha^*}{\sqrt{2}} \langle S | p_x | X \rangle \\ \langle S \uparrow | p_x | 5 \rangle &= \frac{\beta}{\sqrt{2}} \langle S | p_x | X \rangle \\ \langle S \uparrow | p_x | 6 \rangle &= 0 \end{aligned} \quad (27)$$

TM( $\hat{e} = \hat{z}$ ) polarization

$$\begin{aligned} \langle S \uparrow | p_z | 1 \rangle &= 0 \\ \langle S \uparrow | p_z | 2 \rangle &= 0 \\ \langle S \uparrow | p_z | 3 \rangle &= \beta^* \langle S | p_z | Z \rangle \\ \langle S \uparrow | p_z | 4 \rangle &= 0 \\ \langle S \uparrow | p_z | 5 \rangle &= 0 \\ \langle S \uparrow | p_z | 6 \rangle &= -\beta^* \langle S | p_z | Z \rangle \end{aligned} \quad (28)$$

for  $\eta = \uparrow$ . Similar expressions can be derived for the electron spin  $\eta = \downarrow$  in the conduction band.

Since the only  $\phi$ -dependent term in the integrand of (2) appears in the matrix elements, the integration of the  $\cos(2\phi)$  term over  $\phi$  vanishes. We then obtain two scalar polarization-dependent matrix elements, which result from the  $\phi$  integration of the momentum matrix elements:

TE-polarization ( $\hat{e} = \hat{x}$  or  $\hat{y} \perp c$  axis):

$$\begin{aligned} |(M_x)_{nm}^\sigma(k_t)|^2 &= \frac{|\langle S | p_x | X \rangle|^2}{4} \left\{ \langle \phi_n | g_m^{(1)} \rangle^2 + \langle \phi_n | g_m^{(2)} \rangle^2 \right\} \\ &\quad \text{for } \sigma = U \\ &= \frac{|\langle S | p_x | X \rangle|^2}{4} \left\{ \langle \phi_n | g_m^{(4)} \rangle^2 + \langle \phi_n | g_m^{(5)} \rangle^2 \right\} \\ &\quad \text{for } \sigma = L. \end{aligned} \quad (29)$$

TM-polarization ( $\hat{e} = \hat{z} \parallel c$  axis):

$$\begin{aligned} |(M_z)_{nm}^\sigma(k_t)|^2 &= \frac{|\langle S | p_z | Z \rangle|^2}{2} \langle \phi_n | g_m^{(3)} \rangle^2 \quad \text{for } \sigma = U \\ &= \frac{|\langle S | p_z | Z \rangle|^2}{2} \langle \phi_n | g_m^{(6)} \rangle^2 \quad \text{for } \sigma = L. \end{aligned} \quad (30)$$

We define two equivalent energy parameters,  $E_{pz}$  and  $E_{px}$ , in terms of the band-edge momentum matrix elements

$$\begin{aligned}\frac{m_0 E_{pz}}{2} &= |\langle S | p_z | Z \rangle|^2 \\ \frac{m_0 E_{px}}{2} &= |\langle S | p_x | X \rangle|^2\end{aligned}\quad (31)$$

for the interband transition in a similar way to that of the zinc-blende crystals [26], for which only one parameter is required. These energy parameters can be expressed in terms of the band-structure parameters by generalizing Kane's model [17], [26] to those for the wurtzite crystals, taking into account the hexagonal symmetry [14]. We obtain

$$\begin{aligned}E_{pz} &= \left( \frac{m_0}{m_z^*} - 1 \right) \frac{(E_g + \Delta_1 + \Delta_2)(E_g + 2\Delta_2) - 2\Delta_3^2}{(E_g + 2\Delta_2)} \\ E_{px} &= \left( \frac{m_0}{m_x^*} - 1 \right) \frac{E_g [(E_g + \Delta_1 + \Delta_2)(E_g + 2\Delta_2) - 2\Delta_3^2]}{(E_g + \Delta_1 + \Delta_2)(E_g + \Delta_2) - \Delta_3^2}\end{aligned}\quad (32)$$

Therefore, the numerical values for the interband matrix elements can be calculated using the parameters listed in Table I. It should be pointed out that no experimental data for the magnitudes of the interband optical matrix elements are available due to the lack of a good calibration scheme and probably high-quality GaN samples; the above analytical model does provide a reasonable estimation for the interband matrix elements. For GaAs materials, a similar formula [17] for the energy parameter  $E_{pz} = E_{px}$  of the zinc-blende crystals following Kane's model gives a value of about 21.4 eV, which is about 17% smaller than the reported experimental value of 25.7 eV. We would expect a similar percentage of errors in the numerical values when using the above expressions for wurtzite crystals.

The final expression for  $g_{sp}^e(\hbar\omega)$  in the spontaneous emission rate is

$$\begin{aligned}g_{sp}^e(\hbar\omega) &= \frac{2q^2\pi}{n_r c \epsilon_0 m_0^2 \omega L_w} \sum_{\sigma=U,L} \sum_{n,m} \int \frac{k_t dk_t}{2\pi} |(M_e)_{nm}^{\sigma}(k_t)|^2 \\ &\times \frac{f_n^c(k_t)(1 - f_{\sigma m}^v(k_t))(\gamma/\pi)}{(E_{cv,nm}^e(k_t) - \hbar\omega)^2 + \gamma^2}\end{aligned}\quad (33)$$

The total spontaneous emission rate per energy interval per unit volume,  $r_{sp}(\hbar\omega)$ , is given by

$$r_{sp}(\hbar\omega) = \frac{n_e^2 \omega^2}{\pi^2 \hbar c^2} \frac{(2g_{sp}^x + g_{sp}^z)}{3}\quad (34)$$

which uses the fact that the momentum-matrix element of the total spontaneous emission is the angular average of two TE-polarization components and one TM-polarization component

$$|M_{sp}|^2 = \frac{1}{3}(2|M_x|^2 + |M_z|^2).\quad (35)$$

For a given injection level, the electron and hole concentrations are related by the charge neutrality condition

$$n + N_A = p + N_D\quad (36)$$

where  $N_A$  and  $N_D$  are the ionized acceptor and donor concentrations, respectively, in the active region and are assumed to

be zero for an undoped active layer. The electron concentration  $n$  and the hole concentration  $p$  are related to the quasi-Fermi levels,  $F_c$  and  $F_v$ , in (4) and (5), by

$$\begin{aligned}n &= \frac{2}{L_w} \sum_n \int \frac{k_t dk_t}{2\pi} f_n^c(k_t) \\ &= \frac{k_B T m_e^*}{\pi \hbar^2 L_w} \sum_n \ln [1 + e^{(F_c - E_n^c(0))/k_B T}]\end{aligned}\quad (37)$$

$$p = \frac{1}{L_w} \sum_{\sigma=U,L} \sum_m \int \frac{k_t dk_t}{2\pi} (1 - f_{\sigma m}^v(k_t)).\quad (38)$$

## V. NUMERICAL RESULTS AND DISCUSSIONS

We consider first a layer of GaN under either a compressive or tensile strain, depending on the barrier materials, with the convention that the in-plane strain  $\epsilon_{xx}$  is negative for compression and positive for tension. The conduction band-edge energy in the GaN bulk layer is

$$E_c = E_v^0 + \Delta_1 + \Delta_2 + E_g + P_{ce}.\quad (39)$$

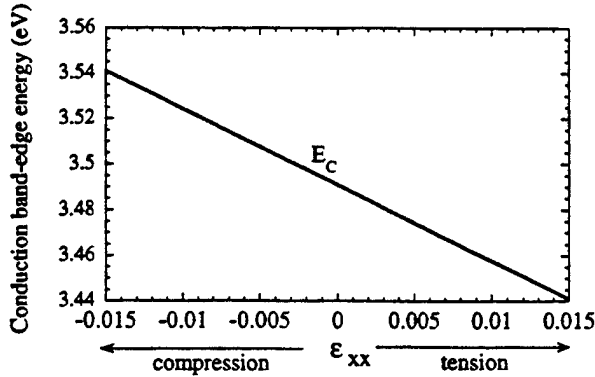
The valence band-edge energies can be obtained by finding the eigenvalues of the three-by-three Hamiltonians, (17), evaluated at the zone center ( $k = 0$ )

$$\begin{aligned}E_{HH} &= E_v^0 + \Delta_1 + \Delta_2 + \theta_e + \lambda_e, \\ E_{LH} &= E_v^0 + \frac{\Delta_1 - \Delta_2 + \theta_e}{2} + \lambda_e \\ &\quad + \sqrt{\left( \frac{\Delta_1 - \Delta_2 + \theta_e}{2} \right)^2 + 2\Delta_3^2} \\ E_{CH} &= E_v^0 + \frac{\Delta_1 - \Delta_2 + \theta_e}{2} + \lambda_e \\ &\quad - \sqrt{\left( \frac{\Delta_1 - \Delta_2 + \theta_e}{2} \right)^2 + 2\Delta_3^2}\end{aligned}\quad (40)$$

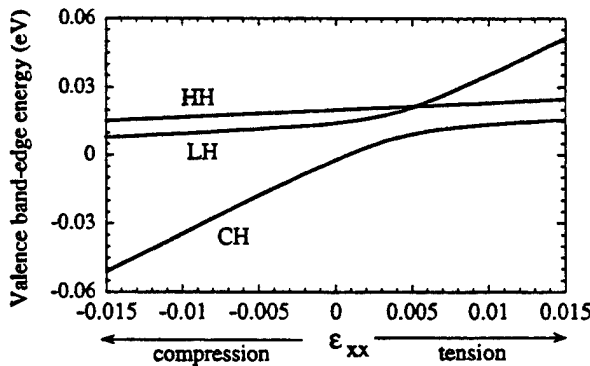
The band edge energies of the conduction band,  $E_c$ , the HH, the LH, and the CH bands are shown in Fig. 4(a) and (b). With increasing compressive strain, the bandgap energy  $E_c - E_{HH}$  increases, where

$$\begin{aligned}E_c - E_{HH} &= E_g + P_{ce} - (\lambda_e + \theta_e) \\ &= E_g + (a_{cz} - D_1 - D_3)\epsilon_{zz} \\ &\quad + (a_{ct} - D_2 - D_4)(\epsilon_{xx} + \epsilon_{yy}).\end{aligned}\quad (41)$$

It should be pointed out that most measurements of the bandgap energy as a function of an externally applied hydrostatic pressure can only provide the total interband deformation potential,  $(a_{cz} - D_1 - D_3)$  or  $(a_{ct} - D_2 - D_4)$ , and it is not possible to distinguish these two numbers, or individual parameters. The hydrostatic pressure also leads to the same sign for  $\epsilon_{xx}$ ,  $\epsilon_{yy}$ , and  $\epsilon_{zz}$ , while a biaxial strain in the GaN-AlGaIn QW structure has a sign difference between the in-plane strain ( $\epsilon_{xx} = \epsilon_{yy}$ ) and the strain along the growth direction ( $\epsilon_{zz}$ ). At zero strain,  $E_{HH} = \Delta_1 + \Delta_2 = 0.020$  eV using the parameters listed in Table I. These parameters were obtained by fitting to the experimental data collected in [27]. With increasing tensile strain, which would require an AlInN or AlInGaIn barrier material (see Fig. 1), the band gap of the tensile-strained GaN



(a)

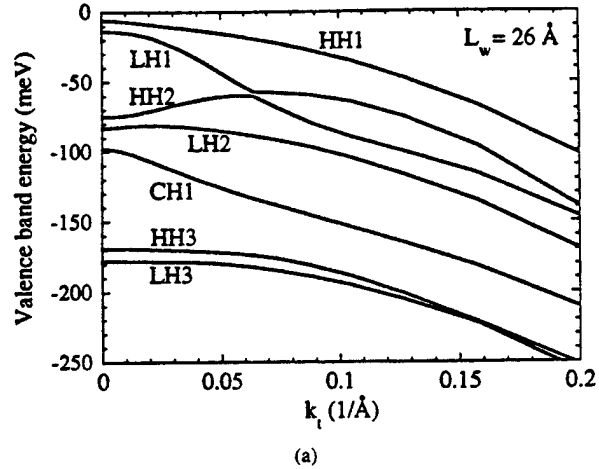


(b)

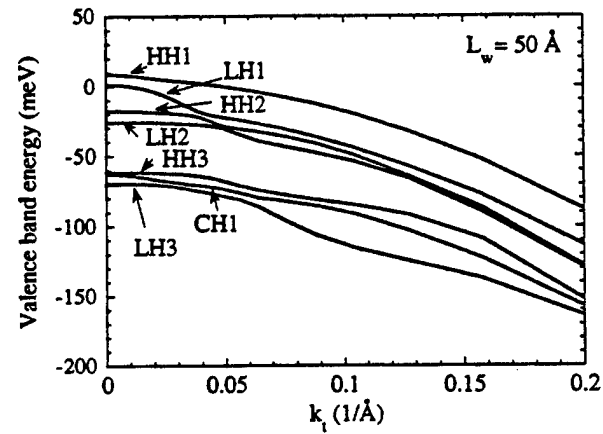
Fig. 4. The band edges of (a) the conduction band and (b) the HH, the LH, and the CH bands as a function of the compressive and tensile strains for a GaN crystal. The reference energy is set at  $E_v^0$  of an unstrained GaN material.

will have a smaller band gap than the unstrained GaN. The strong coupling of the LH and CH bands also splits the energy at a value of strain near 0.004 (or 0.4%). Since the band-structure parameters such as the deformation potentials and effective-mass parameters for the valence band are available only for  $\text{Al}_x\text{Ga}_{1-x}\text{N}$  compounds, we present numerical results for the GaN-AlGaIn QW structures in the following numerical examples. This system has only compressive strain instead of tensile strain in the GaN well layers.

The valence subband dispersion curves are shown in Fig. 5(a) and (b) for two QW structures with well widths  $L_w = 26 \text{ \AA}$  and  $50 \text{ \AA}$ , respectively. We choose  $62 \text{ \AA}-26 \text{ \AA}-62 \text{ \AA}$  and  $50 \text{ \AA}-50 \text{ \AA}-50 \text{ \AA}$  as the barrier-well-barrier widths and use an interval of  $2 \text{ \AA}$  in a finite-difference method [28] to find the electron and hole wave functions when we solve the coupled differential equations. The label of the HH, the LH, and the CH subbands is determined by the wave functions and their components at the band edges,  $k_t = 0$ . For HH subbands, the wave function component,  $g^{(1)}$  or  $g^{(4)}$ , is dominant. For LH subbands,  $g^{(2)}$  or  $g^{(5)}$ , and for CH subbands,  $g^{(3)}$  or  $g^{(6)}$ , are dominant. Fig. 5(a) and (b) also shows that a thick well has closer spacings between the subband energies than those of the thin well. For the quasi-two-dimensional nature of the density of states to play a significant role on the optical gain of a QW laser, a thin well is desirable, especially because the electron and hole effective masses of GaN are very heavy. However, a



(a)



(b)

Fig. 5. The valence subband structures of a strained GaN-Al<sub>0.3</sub>Ga<sub>0.7</sub>N quantum well with well widths: (a)  $L_w = 26 \text{ \AA}$  and (b)  $L_w = 50 \text{ \AA}$ . The reference energy is set at  $E_v^0$  of an unstrained GaN material.

thin well reduces the modal gain; therefore, multiple quantum wells are required.

We show in Fig. 6(a) and (b) the dispersion of the momentum-matrix elements as a function of the in-plane wavenumber  $k_t$  on the  $k_x-k_y$  plane for the first conduction subband (C1) to the first heavy-hole (HH1), the light-hole (LH1), and the crystal-field split-hole (CH1) transitions and their polarization dependences for  $L_w = 26 \text{ \AA}$ . Both the C1-HH1 and C1-LH1 transitions have strong TE components near the zone center, while the C1-CH1 transition has a dominant TM component, which can be larger than the other transitions for the TE polarizations. However, since the compressive strain in the quantum well makes the top few valence subbands HH- or LH-like, the dominant transitions for the compressive GaN-AlGaIn transitions will be TE polarization. This result is different from that of a zinc-blende structure, for which the conduction to LH subband transition has a dominant TM component, and the LH subband can be shifted downward away from the top HH subband with a compressive strain. For a wurtzite structure, the HH and LH subbands tend to shift in the same direction by almost the same amount of energy, resulting in competition for the hole population in

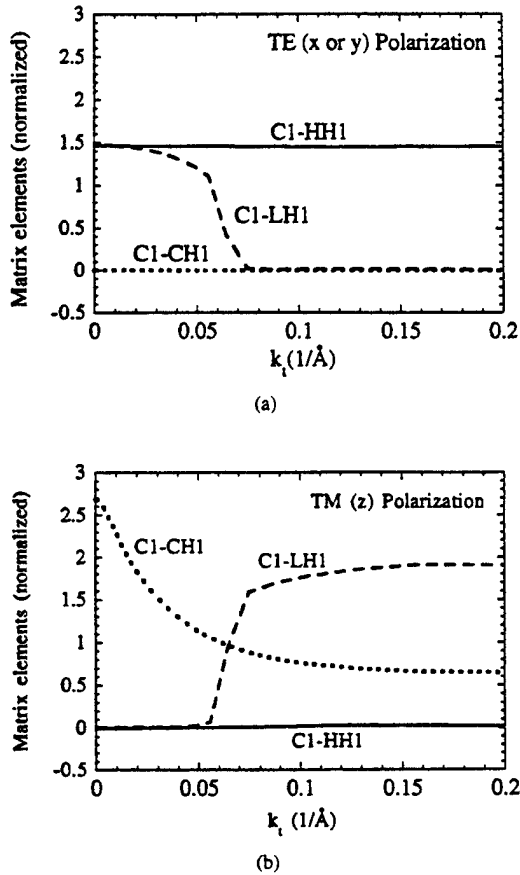


Fig. 6. The normalized momentum-matrix elements for the first conduction (C1) subband to the HH1, the LH1, and the CH1 subband transitions for (a) TE polarization [on the  $x$ - $y$  plane, which is perpendicular to the  $c$  axis ( $=z$  axis)] and (b) TM polarization (along the  $c$  axis) for a well width  $L_w = 26 \text{ \AA}$ .

each subband. Both the HH and LH bands contribute to the same (TE) polarization, yet at different energies result in a broader gain spectrum than those of the zinc-blende structures. The momentum-matrix elements in Fig. 6(a) and (b) also show that the coupling between the LH1 and CH1 subbands is weak, while the coupling between the LH1 and HH2 becomes strong at  $k_t$  near  $0.07 \text{ \AA}^{-1}$ , as can be checked from the valence band structure in Fig. 5(a) and (27)–(28).

Fig. 7(a) and (b) show the material gain spectrum,  $g(\hbar\omega)$ , and the spontaneous emission spectrum, which is proportional to  $\hbar\omega r_{sp}^e(\hbar\omega)$ , of a single QW structure for well widths of  $26 \text{ \AA}$  and  $50 \text{ \AA}$ , respectively. The solid curves are for the TE polarization and the dashed curves for the TM polarization. A narrow well has a larger separation of subbands, resulting in sharper gain and spontaneous emission spectra than those of a wider well. We plot in Fig. 8(a) and (b) the gain spectrum for three carrier concentrations ranging from  $1 \times 10^{19} \text{ cm}^{-3}$  to  $3 \times 10^{19} \text{ cm}^{-3}$  for TE (solid curves) and TM (dashed curves) polarizations. It is clearly seen that the TM polarized gain is very small, as expected from the valence subband structures, since the HH and LH subbands contribute mostly to TE polarization.

The spontaneous emission spectrum is useful since a lot of the experimental data have been obtained using a surface emission configuration via optical pumping of GaN films

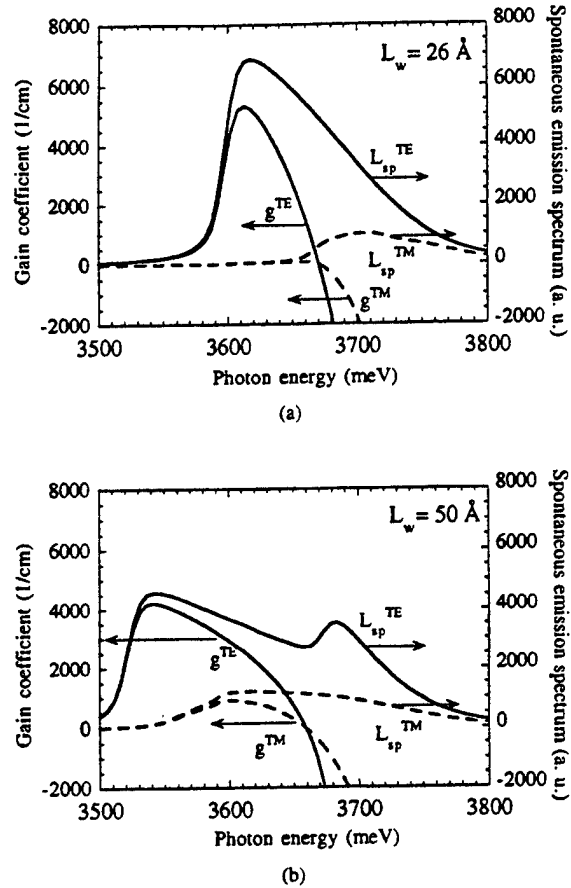


Fig. 7. Spontaneous emission spectrum (right axis in arbitrary units), which is proportional to  $\hbar\omega r_{sp}^e(\hbar\omega)$ , and optical gain spectrum (left axis),  $g(\hbar\omega)$ , for a strained GaN- $\text{Al}_{0.3}\text{Ga}_{0.7}\text{N}$  quantum well with a well width of (a)  $L_w = 26 \text{ \AA}$  and (b)  $L_w = 50 \text{ \AA}$  at the same carrier concentration  $n = 3 \times 10^{19} \text{ cm}^{-3}$ . Solid curves are for the TE polarization, which is on the  $x$ - $y$  plane. Dashed curves are for the TM polarization.

instead of an edge-emission configuration due to the difficulty of cleaving GaN layers to form mirrors. The spontaneous emission spectrum is also used to calculate the gain spectrum in our model based on (2) and (6). Previously, optical gain of GaN zinc-blende crystal was calculated using a simple parabolic band model [29] and using a many-body formulation [30] with valence-band mixing. Our results for wurtzite structures have the same order of magnitude compared with the previous calculations [13], [29], [30] for both crystal structures since the effective masses are about the same.

The peak gain coefficient is plotted as a function of the carrier concentration per quantum well in Fig. 9(a). The transparent carrier densities are larger than  $1$  or  $1.5 \times 10^{19} \text{ cm}^{-3}$  and the gain increases very fast once the carrier densities are above the transparent values. It is interesting to note that the earliest experimental report [3] of stimulated emission from GaN crystals using optical pumping has a gain coefficient ranging from  $1.3 \times 10^3$  to  $1 \times 10^5 \text{ cm}^{-1}$ , depending on the pump intensity. Although the transparent carrier density is very large, the gain increases quickly with increasing carrier density above the transparent-density value. The gain coefficient of a thinner well has a larger transparent carrier density, yet a larger differential gain, than those of a wider

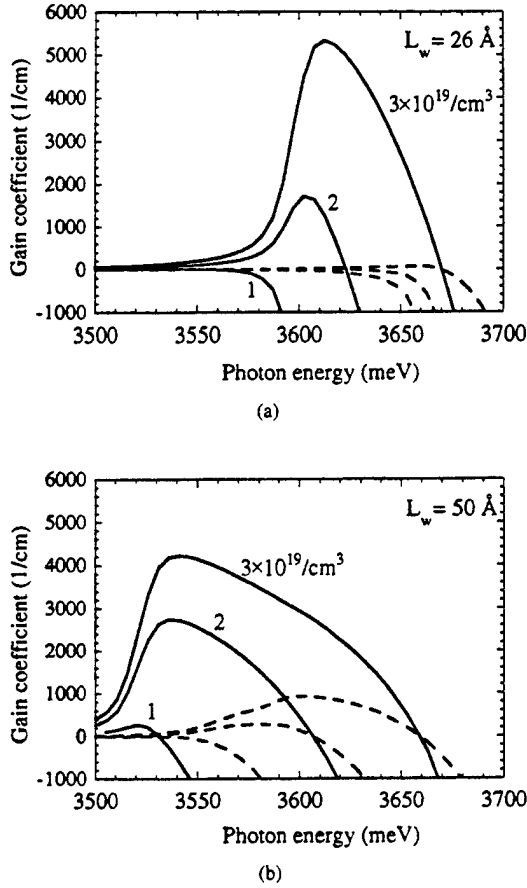


Fig. 8. Optical gain spectra for a strained GaN-Al<sub>0.3</sub>Ga<sub>0.7</sub>N quantum well with a well width of (a)  $L_w = 26$  Å and (b)  $L_w = 50$  Å at carrier concentrations  $n = 1 \times 10^{19}$ ,  $2 \times 10^{19}$ , and  $3 \times 10^{19}$  cm<sup>-3</sup>. Solid curves are for the TE polarization. Dashed curves are for the TM polarization.

well. Both the carrier density,  $n$ , and the material gain per well,  $g$ , are proportional to  $1/L_w$ , or the density of states. The modal gain, which determines the threshold condition of a laser diode, is proportional to the material gain multiplied by the optical confinement factor, which is proportional to the well width. Since the injection current density is in amperes per unit area, we replot the gain-wellwidth product, ( $gL_w$ ), versus the surface carrier concentration in Fig. 9(b) for another comparison. The surface carrier concentration,  $n_s = nL_w$ , will be the number of carriers injected into each well per unit area. The plot in Fig. 9(b) shows an interesting improvement in the transparent surface carrier density and differential gain by using a thin well rather than a wide well in the active region of a QW structure.

Using the electron and hole effective masses [5], [6],  $m_e = 0.20m_0$  and  $m_h = 0.80m_0$ , the dielectric constant [31],  $\epsilon = 9.38\epsilon_0$ , where  $\epsilon_0$  is the permittivity of free space, we obtain an exciton binding energy

$$E_{ex} = \frac{m_r e^4}{2(4\pi\epsilon\hbar)^2} \quad (42)$$

equal to 25 meV, and the exciton Bohr radius

$$a_B = \frac{4\pi\epsilon\hbar^2}{m_r e^2} \quad (43)$$

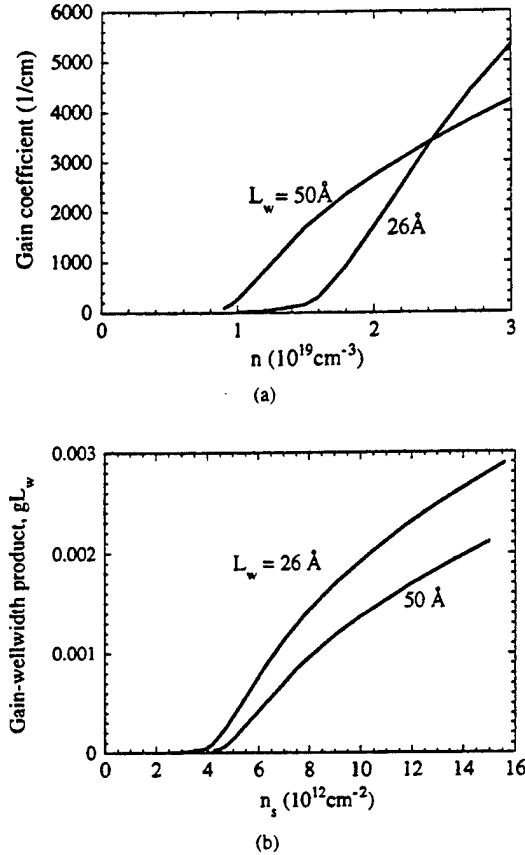


Fig. 9. (a) Peak optical gain coefficient as a function of the injected carrier density,  $n$ , for a strained GaN-Al<sub>0.3</sub>Ga<sub>0.7</sub>N quantum well with a well width  $L_w = 26$  Å, and  $L_w = 50$  Å and (b) Gain-wellwidth product,  $gL_w$ , which is the material gain  $g$  in (a) multiplied by the well width  $L_w$  and is proportional to the modal gain coefficient of a double heterojunction laser, is plotted as a function of the injected surface carrier density,  $n_s = nL_w$ . The polarization is on the  $x$ - $y$  plane (TE).

about 31 Å. Here,  $m_r = m_e m_h / (m_e + m_h)$  is the reduced effective mass. We then estimate the carrier density above which the exciton phase becomes unstable with respect to an electron-hole plasma for a two-dimensional structure,  $n_c = 1/(\pi a_B^2) = 3.3 \times 10^{12}$  cm<sup>-2</sup>. This value is smaller than that of ZnSe [32],  $5.7 \times 10^{12}$  cm<sup>-2</sup>. From Fig. 9(b), we find a significant amount of gain occurs when the surface carrier concentration  $n_s$  is larger than  $4 \times 10^{12}$  cm<sup>-2</sup>. Therefore, the electron-hole plasma model should be appropriate in the estimation of the optical gain. It should be noted that bandgap shrinkage for a strained wurtzite QW laser and an enhancement of the matrix elements due to the screened Coulomb interaction in an electron-hole plasma will increase the gain value by about 30% [30] and shift the peak gain energy by an amount of the order of 20–50 meV, which is determined by the carrier density. On the other hand, strain may be relaxed in the GaN layer because of dislocation, and the amount of the increase in bandgap energy in the above theory due to compressive strain may be ignored in strain-relaxed samples.

## VI. CONCLUSION

We have presented a comprehensive theoretical model for calculating the electronic band structures and optical gain for

a wurtzite-strained QW structure. Our model is based on the effective-mass Hamiltonian derived recently using the  $\mathbf{k} \cdot \mathbf{p}$  method for wurtzite crystals. We also presented new analytical expressions and numerical results for the QW band structure, the basis transformation, the interband optical-matrix elements, and their applications to the calculations of the optical gain coefficient. Our model provides a foundation for calculating the optical gain and spontaneous emission properties of a strained wurtzite GaN QW laser. For a GaN layer with much heavier electron and hole effective masses than those of a zinc-blende structure, the necessity of using thin multiple quantum wells is pointed out and demonstrated in our model calculations.

#### ACKNOWLEDGMENT

The author would like to thank C. S. Chang for stimulating discussions on the band-structure calculations in the early part of this work.

#### REFERENCES

- [1] A. Ishibashi, "II-VI blue-green laser diodes," *IEEE J. Select. Topics Quantum Electron.*, vol. 1, pp. 741-748, 1995.
- [2] S. Nakamura, M. M. Senoh, S. Nagahama, N. Iwasa, T. Yamada, T. Matsushita, H. Kiyoku, and Y. Sugimoto, "InGaIn-based multi-quantum-well-structure laser diodes," *Jpn. J. Appl. Phys.*, vol. 35, pp. L74-L76, 1996.
- [3] R. Dingle, K. L. Shaklee, R. F. Leheny, and R. B. Zetterstrom, "Stimulated emission and laser action in gallium nitride," *Appl. Phys. Lett.*, vol. 19, pp. 5-7, 1971.
- [4] I. Akasaki, H. Amano, S. Sota, H. Sakai, T. Tanaka, and M. Koike, "Stimulated emission by current injection from an AlGaIn/GaN quantum well device," *Jpn. J. Appl. Phys.*, vol. 34, pt. 2, pp. L1517-L1519, 1995.
- [5] K.-H. Hellwege, Ed., *Numerical Data and Functional Relationships in Science and Technology*, Landolt-Börnstein, New Series, Groups III-V. Berlin: Springer, 1986, vol. 22a.
- [6] J. H. Edgar, Ed., *Properties of Group III Nitrides*. London: INSPEC, IEE, 1994.
- [7] K. Kubota, Y. Kobayashi, and K. Fujimoto, "Preparation and properties of III-V nitride thin films," *J. Appl. Phys.*, vol. 66, pp. 2984-2988, 1989.
- [8] G. L. Bir and G. E. Pikus, *Symmetry and Strain-Induced Effects in Semiconductors*. New York: Wiley, 1974.
- [9] G. E. Pikus, "A new method of calculating the energy spectrum of carriers in semiconductors. I. Neglecting spin-orbit interaction," *Sov. Phys. JEPT*, vol. 14, pp. 898-907, 1962.
- [10] ———, "A new method of calculating the energy spectrum of carriers in semiconductors. II. Account of spin-orbit interaction," *Sov. Phys. JEPT*, vol. 14, pp. 1075-1085, 1962.
- [11] M. Suzuki, T. Uenoyama, and A. Yanase, "First-principles calculations of effective-mass parameters of AlN and GaN," *Phys. Rev. B*, vol. 52, pp. 8132-8139, 1995.
- [12] T. Uenoyama and M. Suzuki, "Valence subband structures of wurtzite GaN/AlGaIn quantum wells," *Appl. Phys. Lett.*, vol. 67, pp. 2527-2529, 1995.
- [13] S. Kamiyama, K. Ohnaka, M. Suzuki, and T. Uenoyama, "Optical gain calculation of wurtzite GaN/AlGaIn quantum well laser," *Jpn. J. Appl. Phys.*, vol. 34, p. L821, 1995.
- [14] S. L. Chuang and C. S. Chang, " $\mathbf{k} \cdot \mathbf{p}$  method for strained wurtzite semiconductors," *Phys. Rev. B*, vol. 54, pp. 2491-2504, July, 1996.
- [15] J. M. Luttinger and W. Kohn, "Motion of electrons and holes in perturbed periodic field," *Phys. Rev.*, vol. 97, pp. 869-883, 1955.
- [16] C. Y.-P. Chao and S. L. Chuang, "Spin-orbit-coupling effects on the valence-band structure of strained semiconductor quantum wells," *Phys. Rev. B*, vol. 46, pp. 4110-4122, 1992.
- [17] S. L. Chuang, *Physics of Optoelectronic Devices*. New York: Wiley, 1995.
- [18] C. S. Chang and S. L. Chuang, "Modeling of strained quantum well lasers with spin-orbit coupling," *IEEE J. Select. Topics Quantum Electron.*, vol. 1, pp. 218-229, 1995.
- [19] S. L. Chuang and C. S. Chang, "Effective-mass Hamiltonian for strained wurtzite GaN and analytical solutions," *Appl. Phys. Lett.*, vol. 68, pp. 1-3, 1996.
- [20] D. Ahn and S. L. Chuang, "Optical gain in a strained-layer quantum-well laser," *IEEE J. Quantum Electron.*, vol. 24, pp. 2400-2406, 1988.
- [21] C. S. Chang and S. L. Chuang, "Amplified spontaneous emission spectroscopy in strained quantum-well lasers," *IEEE J. Select. Topics Quantum Electron.*, vol. 1, pp. 1100-1107, 1995.
- [22] S. L. Chuang, J. O'Gorman, and A. F. J. Levi, "Amplified spontaneous emission and carrier pinning in laser diodes," *IEEE J. Quantum Electron.*, vol. 29, pp. 1631-1639, 1993.
- [23] A. E. H. Love, *A Treatise on the Mathematical Theory of Elasticity*. New York: Dover, 1994, pp. 151-160.
- [24] F. Bassani and G. P. Parravicini, *Electronic States and Optical Transitions in Solids*. Oxford, U.K.: Pergamon, 1975, p. 24.
- [25] G. Martin, S. Strite, A. Botchkarev, A. Agarwal, A. Rockett, H. Morkoc, W. R. L. Lambrecht, and B. Segall, "Valence-band discontinuity between GaN and AlN measured by X-ray photoemission spectroscopy," *Appl. Phys. Lett.*, vol. 65, p. 610, 1994.
- [26] E. O. Kane, "Band structure of Indium Antimonide," *J. Phys. Chem. Solids*, vol. 1, pp. 249-261, 1957.
- [27] B. Gil, O. Briot, and R.-L. Aulombard, "Valence-band physics and the optical properties of GaN epilayers grown onto sapphire with wurtzite symmetry," *Phys. Rev. B*, vol. 52, pp. R17028-R17031, 1995.
- [28] S. L. Chuang and C. S. Chang, "Band structure model of strained quantum-well wurtzite semiconductors," unpublished.
- [29] W. Fang and S. L. Chuang, "Theoretical prediction of GaN lasing and temperature sensitivity," *Appl. Phys. Lett.*, vol. 67, pp. 751-753, 1995.
- [30] W. W. Chow, A. F. Wright, and J. S. Nelson, "Theoretical study of room temperature optical gain in GaN strained quantum wells," *Appl. Phys. Lett.*, vol. 68, pp. 296-298, 1996.
- [31] S. Chichibu, T. Azuhata, T. Sota, and S. Nakamura, "Excitonic emissions from hexagonal GaN epitaxial layers," *J. Appl. Phys.*, vol. 79, p. 2784, 1996.
- [32] J. Ding, H. Jeon, T. Ishihara, M. Hagerott, and A. V. Nurmikko, "Excitonic gain and laser emission in ZnSe-based quantum wells," *Phys. Rev. Lett.*, vol. 69, pp. 1707-1710, 1992.
- [33] R. Dingle, D. D. Sell, S. E. Stokowski, and M. Ilegems, "Absorption, reflectance, and luminescence of GaN epitaxial layers," *Phys. Rev. B*, vol. 4, pp. 1211-1218, 1971.



**Shun Lien Chuang** (S'78-M'82-SM'88) received the B.S. degree in electrical engineering from National Taiwan University in 1976, and the M.S., E.E., and Ph.D. degrees in electrical engineering from the Massachusetts Institute of Technology, Cambridge, MA, in 1980, 1981, and 1983, respectively.

While in graduate school, he held research and teaching assistantships and also served as a Recitation Instructor. In 1983, he joined the Department of Electrical and Computer Engineering at the University of Illinois at Urbana-Champaign, where he is currently a Professor. He was a Resident Visitor at AT&T Bell Laboratories, Holmdel, NJ, in 1989. He was a Consultant at Bellcore and Polaroid in 1991, and a Senior Visiting Professor at SONY Research Center in 1995. He was also an Associate at the Center for Advanced Study at the University of Illinois in 1995. He is conducting research on strained quantum-well semiconductor lasers and femtosecond nonlinear optics. He developed a graduate course on integrated optics and optoelectronics. He is the author of *Physics of Optoelectronic Devices* (New York: Wiley, 1995). He was a Feature Editor for a special issue of the JOURNAL OF THE OPTICAL SOCIETY OF AMERICA B on *Terahertz Generation, Physics and Applications* in 1994. He has published more than 150 conference and journal papers and was invited to give talks at conferences including the American Physical Society March Meeting, Optical Society of America Annual Meeting, and Integrated Photonics Research.

Dr. Chuang is a member of the Optical Society of America and the American Physical Society. He has been cited several times for Excellence in Teaching. He received the Andersen Consulting Award from the University of Illinois for excellence in advising in 1994. He was also awarded a Fellowship from the Japan Society for the Promotion of Science to visit the University of Tokyo in 1996.

# REPORT DOCUMENTATION PAGE

Form Approved

OMB No. 0704-0188

Public reporting burden for this collection of information is estimated to average 1 hour per response, including the time for reviewing instructions, searching existing data sources, gathering and maintaining the data needed, and completing and reviewing the collection of information. Send comments regarding this burden estimate or any other aspect of this collection of information, including suggestions for reducing this burden to Washington Headquarters Services, Directorate for Information Operations and Reports, 1215 Jefferson Davis Highway, Suite 1204, Arlington, VA 22202-4302, and to the Office of Management and Budget, Paperwork Reduction Project (0704-0188), Washington, DC 20503.

1. AGENCY USE ONLY (Leave blank)		2. REPORT DATE April 5, 1999		3. REPORT TYPE AND DATES COVERED Final Technical 10/95 - 12/99	
4. TITLE AND SUBTITLE High-Speed Strained Quantum-Well Lasers and Optoelectronic Devices				5. FUNDING NUMBERS N00014-96-1-0303	
6. AUTHOR(S) S. L. Chuang					
7. PERFORMING ORGANIZATION NAMES(S) AND ADDRESS(ES) University of Illinois Dept. of Electrical & Computer Engineering 1406 W. Green Street Urbana, IL 61801				8. PERFORMING ORGANIZATION REPORT NUMBER	
9. SPONSORING / MONITORING AGENCY NAMES(S) AND ADDRESS(ES) Office of Naval Research CODE 251 Ballston Centre Tower One 800 N. Quincy Street Arlington, VA 22217-5660				10. SPONSORING / MONITORING AGENCY REPORT NUMBER	
11. SUPPLEMENTARY NOTES					
a. DISTRIBUTION / AVAILABILITY STATEMENT Approved for public release				12. DISTRIBUTION CODE	
13. ABSTRACT (Maximum 200 words)  We investigate research issues on strained quantum-well optoelectronic devices and their applications for navy needs. This work studies the fundamental physics in strained quantum-well devices such as Fabry-Perot (FP) lasers, distributed-feedback (DFB) lasers, and vertical cavity surface-emitting lasers (VCSELs) through the development of theory and experiment. Integrated optoelectronic devices are also investigated for applications in wavelength-division-multiplexed (WDM) fiber-optic communications systems such as wavelength tunability and wavelength conversion. In this work, we investigate the following areas: <ul style="list-style-type: none"> <li>a. Comprehensive characterization of fundamental parameters of strained quantum-well lasers</li> <li>b. Modeling and experiment of integrated laser/modulator devices</li> <li>c. Modeling and experiment of VCSELs</li> <li>d. Wavelength conversion using four-wave mixing and cross-phase/gain/absorption modulation</li> <li>e. Optical gain theory for GaN-based blue-green quantum-well lasers</li> </ul>					
14. SUBJECT TERMS strained quantum-well lasers, semiconductor lasers, optoelectronics, integrated laser-modulators				15. NUMBER OF PAGES	
				16. PRICE CODE	
17. SECURITY CLASSIFICATION OF REPORT unclassified	18. SECURITY CLASSIFICATION OF THIS PAGE unclassified	19. SECURITY CLASSIFICATION OF ABSTRACT unclassified	20. LIMITATION OF ABSTRACT UL		